Ab-initio insights into the tunability of the electronic structure in transition metal dichalcogenide alloys grown by atomic layer deposition

Schulpen, Jeff J.P.M.

Award date:
2018

Ab-initio insights into the tunability of the electronic structure in Transition Metal Dichalcogenide alloys grown by Atomic Layer Deposition

Jeff Schulpen
Dr. Vincent Vandalon
Dr. Ageeth Bol

October 2018

Contents

Chapter 1

Introduction

While the exotic properties of graphene, a single atomic layer of graphite, were predicted theoretically decades before, it was not until the discovery of the exfoliation technique in 2004 [1] that these predictions could be confirmed experimentally [1, 2, 3]. These discoveries have motivated great progress in the synthesis and investigation of graphene and other two-dimensional materials. Nowadays, a wide variety of these extraordinary 2D materials have been synthesized, most notably the family of transition metal dichalcogenide (TMD) compounds [4, 5, 6] and the graphene-like boron nitride [7, 8] and X-enes like phosphorene [9, 10], silicene [11, 12] and germanene [13, 12]. These materials are receiving ever-increasing research interest [6] due to their potential usability in such diverse applications as nano-electronics [14], catalysis [15], energy storage [16] and sensing [17]. In this work, we focus on the transition metal dichalcogenides.

Transition metal dichalcogenides

Within the spectrum of 2D materials, transition metal dichalcogenides in particular have emerged in recent years as promising materials for use in next-generation nano-electronic devices. Like all 2D materials, they consist of atomically thin layers which are coupled together through Van der Waals interactions and which may be exfoliated down to monolayer thickness. Each monolayer consists of a layer of transition metal atoms (e.g. Mo, W, Ti, Ta or Nb) which is sandwiched between two layers of chalcogen atoms (S, Se or Te), as shown in figure 1.1. An important benefit of this layered structure is that these materials maintain their useful material properties when exfoliated down to atomic thicknesses. In contrast, bulk crystals like silicon suffer from finite-size effects which are detrimental to their electronic performance at these scales. In addition to the desirable properties which are exhibited by 2D crystals in general, TMDs exhibit some unique properties that distinguish them from other 2D materials. To understand these, we will mainly focus on two specific properties of these materials: their bandgap and the effective mass of their charge carriers. These quantities are essential considerations in many of the proposed applications of transition metal dichalcogenides. Here we will

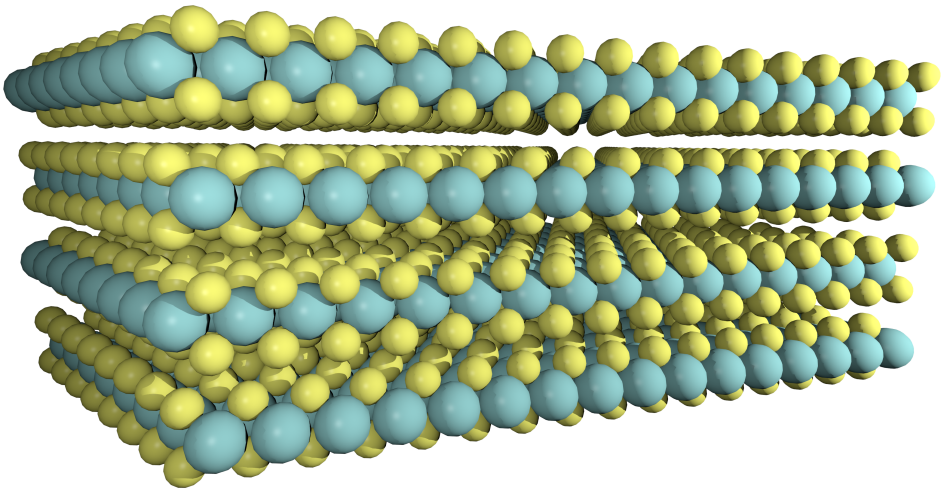

Figure 1.1: Transition metal dichalcogenides (TMDs) form a crystal of atomically thin chalcogen-metal-chalcogen layers, which are bound together through Van der Waals forces.

highlight two examples: next-generation transistors and novel high-accuracy sensors. In many TMDs, the confinement of the electrons to a 2D electron gas leads to the formation of an electronic bandgap in the 1-2 eV range. These semiconducting TMDs neatly complement the semi-metallic graphene and insulating boron nitride, and they may be used in conjunction to produce fully two-dimensional transistors [18, 19]. Additionally, Sylvia et al. [20] have shown that in next-generation low-voltage transistors, there will be an optimum effective carrier mass such that both back-scattering in the channel and tunneling-induced leakage currents are minimized. Control over the effective mass in TMDs could contribute to performing such optimizations. The development of novel sensors on the other hand may benefit from the fact that the bandgap in semiconducting TMDs transitions from indirect to direct and changes its magnitude when the material is scaled down from bulk to monolayer thickness [21], making it possible to tailor the bandgap to specific sensing applications.

These examples illustrate that a precise control over the electronic properties like the bandgap and effective mass in TMDs would give these materials a great advantage for implementation in next-generation electronics and sensors. Of course, other challenges like developing a cost-effective method to synthesize TMDs on wafer scale will also have to be overcome. Ongoing research on this topic is mostly focussed on the chemical vapor deposition (CVD), physical vapor deposition (PVD) and atomic layer deposition (ALD) techniques. However, the present work will focus on the challenge of achieving control over the electronic properties of TMDs and gaining insight into the mechanisms through which this control can be achieved.

Research questions

Various methods of achieving control over the electronic properties of TMDs are already being explored in literature. In addition to the aforementioned controllable bandgap transition in TMDs, tunability may also be achieved through strain engineering, introducing crystal defects [22, 23], doping [24, 25], or combining multiple TMDs into alloys [26, 27]. In this work, we employ ab-initio electronic structure calculations in order to provide insight into how two of these techniques achieve control over electronic properties: point defects in TMDs and binary alloys of TMDs. To guide the investigation, we have formulated three research questions which we aim to answer in this thesis:

1. Can density functional theory (DFT) be used to calculate structural and electronic properties like lattice parameters, bandgap, carrier mobility and phonon frequencies of transition metal dichalcogenides with enough accuracy to compare them to experimental results?

2. What role do crystal defects play in determining the electronic properties of transition metal dichalcogenides?

3. How can the atomic ordering of binary TMD alloys be exploited to achieve control over their electronic properties?

Below we describe in which parts of the thesis these individual questions are addressed. An graphical outline of the thesis by topic is provided in figure 1.2

In order to answer the first question, we first summarize the essential theoretical fundamentals of the electronic structure of crystals and calculation methods in chapter 2. We identify the important parameters that need to be carefully optimized to obtain accurate results from density functional theory calculations. Subsequently, we perform these optimizations and apply DFT calculations to the TMDs MoS_2 and WS_2 in chapter 3, demonstrating the accuracy of the DFT method in calculating both structural and electronic properties of these materials.

The second research question is addressed in the latter half of chapter 3, where we employ DFT calculations using a supercell method in order to model realistic concentrations of typical point defects found in synthetically grown TMD crystals. We discuss the effects these defects have on thestructural and electronic properties of the material and compare these to the effects of other types of defects typically found in synthesized TMDs, such as grain boundaries.

Chapter 5 addresses the third and final research question. We report results of electrical and optical characterization of $Mo_xW_{1-x}S_2$ alloys synthesized by atomic layer deposition, demonstrating how the material properties change as a function of both the alloy ratio and the atomic mixing of the alloy. Special attention is given both experimentally and theoretically to Raman spectroscopy, a technique which is known to be very sensitive to structural changes in TMDs. Comparison of experimental data with results from DFT calculations gives insight into how the alloy ratio and the atomic

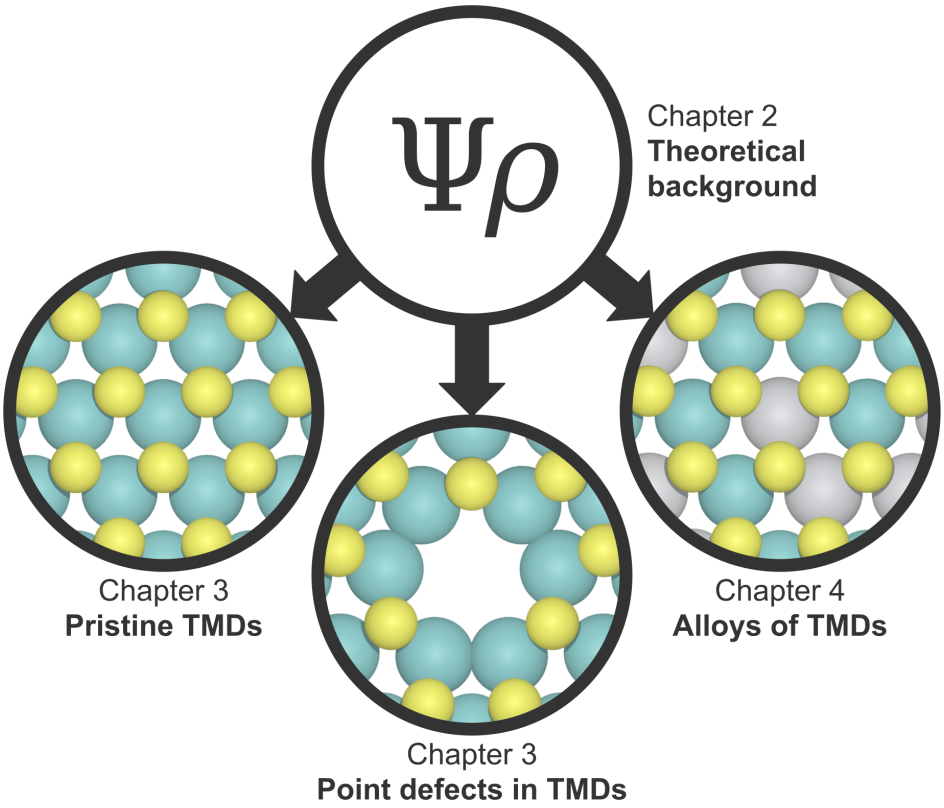

Figure 1.2: Outline of this thesis. Chapter 2 summarizes the theory behind the electronic structure of crystals and calculation methods thereof, with a focus on density functional theory (DFT). In chapter 3, DFT is applied to pristine TMDs as well as TMDs with point defects. In chapter 4, binary alloys of TMDs are investigated through both DFT and experimental deposition and characterization of these materials.

mixing both uniquely impact the electronic and structural properties of the binary TMD alloys.

Chapter 2

Theory: Electronic Structure & Calculation Methods

We are interested in calculating the electronic properties of transition metal dichalcogenides and investigating how they can be controlled. The central object of such an investigation is the so-called electronic band structure. In this chapter, we explain the origin and meaning of the electronic band structure and its derived quantities like the bandgap, effective carrier mass and density of states. Subsequently, we disscuss methods of calculating the electronic band structure. Special attention will be given to Density Functional Theory (DFT), as this is the method that we will employ in later chapters to calculate the electronic band structures of transition metal dichalcogenides. We explain the key concepts necessary to understand these calculations, as well as finally summarizing our computational approach.

2.1 Electronic structure

After the discovery of the electron by Thomson in 1897 [28] and the subsequent discovery of the atomic nucleus [29], it became clear that the interplay between these contituent parts are responsible for almost all of the properties of matter. Indeed, whether it is the electrical (conductivity, permittivity), optical (absorption, emission), structural (compressibility, rigidity) or thermodynamic (heat capacity, heat conductivity) properties that we are interested in, at the most fundamental level they are all determined by the complex joint behaviour of the electrons and atomic nuclei. Naturally then, the main focus of the field of solid state physics is to describe the behavior of the electrons and nuclei in a given material as accurately as possible. This is a formidable task: any macroscopically-sized material consists of a number of nuclei and electrons on the order of at least 10^{23}, whose mutual interactions are governed by the laws of quantum mechanics. As a first line of attack, this quantum many-body problem is usually simplified by decoupling the electron dynamics from the motion of the nuclei, which is known as the Born-Oppenheimer approximation. This approach is justified on

the grounds that the electrons - having a mass four orders of magnitude lower than atomic nuclei - move on timescales much shorter than the nuclei do, such that from the viewpoint of the electrons, the nuclei can be considered static. This method splits the quantum many-body problem into two parts which may be solved consecutively: the configuration of the electrons, known as the electronic structure, and the positions of the atomic nuclei. In crystals, the problem can be simplified even further, as is explained in the next section.

2.2 Crystals

Crystals have historically always been the biggest focus of the research on solid-state physics due to the uniquely simple properties of their electronic structure. Crystals are solids where the constituent atoms form a motif that is repeated periodically. The motif, also called the unit cell, may be as simple as a single atom, as complex as a globular protein molecule thousands of atoms in size, or anything in between. As a simple example, table salt NaCl consists of a motif of one sodium atom and one chloride atom, which is repeated in a cubic structure.

Since in a periodic crystal every unit cell is indistinguishable from any other, the distribution of electrons should also be the same in every unit cell. Since the electron density is equal to the squared amplitude of the electron wavefunction $|\psi|^2$, the magnitude of the wavefunction is constrained to having the same periodicity as the crystal lattice. There is no such restriction on the phase of the wavefunction, and its value may change upon translation along a lattice vector. Consequently, we can express the wavefunction as

$$\psi\left(\boldsymbol{r}+\boldsymbol{R}\right)=e^{(i\boldsymbol{k}\cdot\boldsymbol{R})}\psi\left(\boldsymbol{r}\right), \tag{2.1}$$

where $\boldsymbol{R}$ is any reciprocal lattice vector. The phase shift is written as the dot product of the displacement vector with an arbitrary vector $\boldsymbol{k}$, without loss of generality. While this expression is valid for infinite crystals, a derivation for finite crystals using periodic boundary conditions shows that in that case, the magnitude of $\boldsymbol{k}$ is restricted to a discrete set of values [30]. For a crystal of infinite extent, the vector $\boldsymbol{k}$ may assume any magnitude and thus there is no restriction on the phase shift. An equivalent statement of Bloch's theorem is the following [30]:

$$\psi_{n,k}(\boldsymbol{r})=u_n(\boldsymbol{r})e^{i\boldsymbol{k}\cdot\boldsymbol{r}}, \tag{2.2}$$

where the function $u_n(\boldsymbol{r})$ has the same periodicity as the crystal lattice. This formulation highlights the fact that for each $\boldsymbol{k}$, there exists an infinite discrete range of choices for the function $u_n(\boldsymbol{r})$.

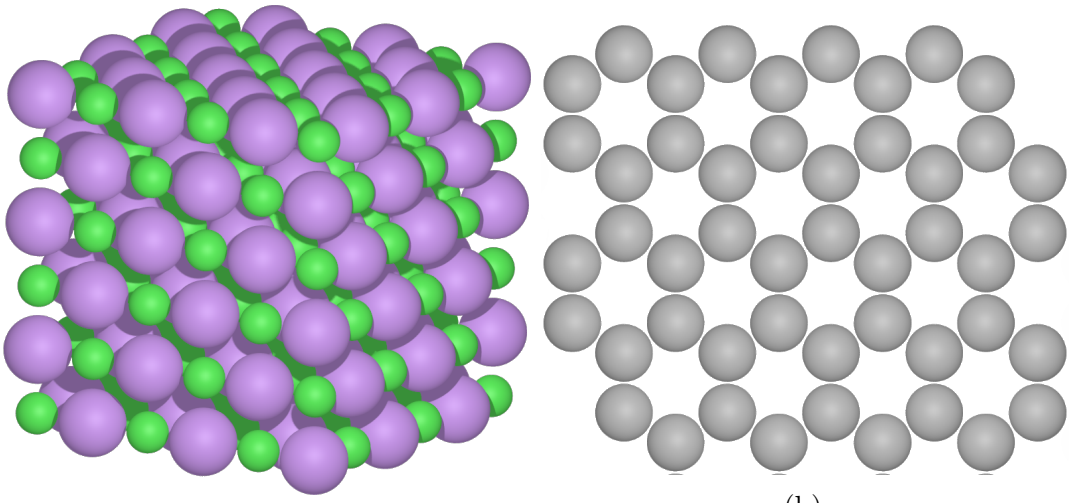

(a) (b)

Figure 2.1: The crystal structures of (a) table salt (NaCl) and (b) two-dimensional graphene, examples of crystals consisting of a simple atomic motif.

2.2.1 Electronic band diagrams

It is instructive to plot the energy of the wavefunctions in a crystal both as a function of the $\boldsymbol{k}$ and n of equation 2.2. Since the wavevector $\boldsymbol{k}$ is allowed to vary continuously while the variable n is a discrete index, so the energy varies smoothly as a function of $\boldsymbol{k}$ but discretely as a function of n. Thus, these plots take the form of a series of continuous bands, each band belonging to a single index n and containing contributions from all values of $\boldsymbol{k}$. A glance at equation 2.1 shows that wavefunctions with wavevectors $\boldsymbol{k}$ and $\boldsymbol{k} + \frac{2\pi}{\boldsymbol{R}}$ are mathematically equivalent. Thus, band structure plots will be periodic in $\boldsymbol{k}$-space and all the information will be contained in the region $\frac{2\pi}{\boldsymbol{R}} < \boldsymbol{k} \leq \frac{2\pi}{\boldsymbol{R}}$, which is known as the Brillouin zone. The Brillouin zone forms a unit cell of the crystal is k-space, and just like the real-space unit cell it can be described with three unit vectors in three dimensions. There is a one-to-one relation between the real-space and reciprocal space unit cells: the unit vectors in both spaces are related through

$$\boldsymbol{a}_i \cdot \boldsymbol{b}_j = \delta_{ij} \tag{2.3}$$

where $\boldsymbol{a}_i$ are the real-space unit vectors, $\boldsymbol{b}_i$ are the k-space unit vectors, and the Kronecker delta δ_{ij} equals 1 for $i = j$, and 0 otherwise. From this relation, it is seen that the unit vectors in both spaces are in fact inverses of each other.

To gain an intuitive understanding for the existence of Brillouin zones and periodicity in $\boldsymbol{k}$-space (or reciprocal space), it is instructive to consider lattice vibrations in crystals, where a similar effect occurs. These lattice vibrations are periodic oscillations of the atoms in a crystal lattice, which can be described as a displacement wave. However, it is only the atoms themselves that are displaced, and it makes no sense to define a displacement for the space between the atoms. Consequently, it is only the value of

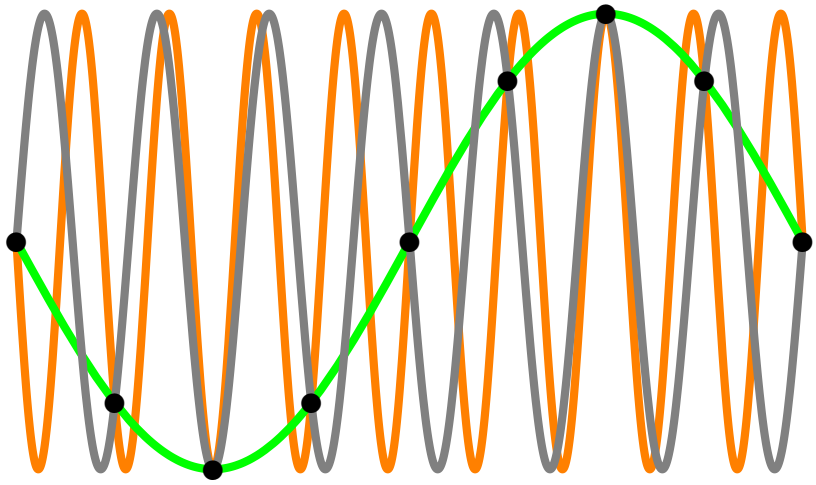

Figure 2.2: A waveform sampled at discrete positions (black dots) can be described by infinitely many different wavelengths, but by only one wavelength larger than twice the sampling spacing (green).

the displacement wave at the atomic positions which is relevant. Due to this discrete sampling of the displacement wave, there exists an ambiguity in the wavelength of the wave: the same pattern of atomic displacements can be described by different wavelengths. In signal processing, this effect is known as aliasing: high-frequency components that are sampled at a low frequency are "aliased" to lower frequencies. In the specific case of audio processing, this effects leads to components of the sound being heard at different frequencies than intended, and in image processing it leads to the emergence of Moiré patterns. In all of these cases, including lattice vibrations, a discretely sampled signal can be represented by an infinite number of wavelengths, but by only one unique wavelength larger than twice the sampling spacing (see figure 2.2. It is exactly these wavelengths that form the Brillouin zone for phonons, as they (or superpositions of them) are able to describe all sets of atomic displacements, including those described by shorter wavelengths outside the Brillouin zone.

While the case for electronic wavefunctions is not exactly analogous - it is not only their value at specific points that matters but rather their value at all points in space - the illustration above still provides a way of intuitively coming to terms with the periodicity of band structures in reciprocal space.

As a typical example of an electronic band structure plot, figure 2.3b shows the band structure of silicon. As silicon is a three-dimensional material, the Brillouin zone is also three-dimensional, which means that it is impossible to depict the energies of the complete set of wavevectors of the Brillouin zone in one figure. To overcome this problem, a specific path through the Brillouin zone is chosen, and only wavevectors along this path are represented in the band diagram. This path is chosen along lines connecting high-symmetry points in the Brillouin zone. These points are labeled by

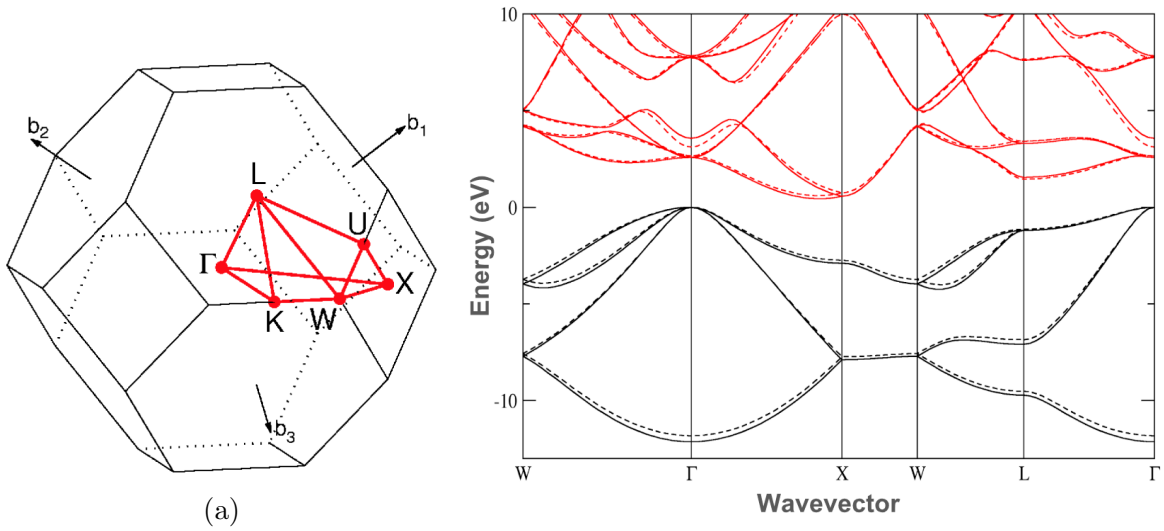

(a) (b)

Figure 2.3: The Brillouin zone [31] (a) and the electronic band diagram [32] (b) of silicon. For a three-dimensional crystal, the Brillouin zone is also three-dimensional, and a path through this zone is chosen for which to plot the electronic energy bands. This path is chosen along lines connecting high-symmetry points in the symmetry-irreducible (unique) part of the Brillouin zone which is marked in red in (a). Conventionally internal high-symmetry points are marked with Greek letters and those on the edge of the Brillouin zone are marked with Latin letters.

unique letters, where Greek letters are used for points in the interior of the Brillouin zone and Latin letters are used for points on the edge.

Quantities derived from band diagrams

Various useful quantities can be derived from the electronic band structure. The ones which are important for this work are discussed below.

Band gap: Band structures generally have "gaps" in them: intervals on the energy scale where there are no electronic states. Rather confusingly, the regions in between the gaps are also referred to as bands, due to their appearance in density of states plots (see below). To distinguish them from the $E(\vec{k})$ bands of band structure diagrams, we will refer to them as "allowed energy bands". In metals, the Fermi level (the level up to which the band structure is filled with electrons) is such that one of these allowed energy bands is partially filled. This gives metals their excellent conductivity: the highest-energy electrons have plenty of free and accessible states to transition to, allowing them to respond to electric fields by changing their pseudomomentum k. In semiconductors and insulators on the other hand, the Fermi level coincides with the top of an allowed energy band. This means that their charge carriers are "stuck": in

order to transition to other states, the carriers need to bridge the band gap from their current allowed energy band (the valence band) to the next allowed energy band (the conduction band). The classification of a material as either a semiconductor or an insulator is based on the magnitude of their band gap. Materials with band gaps small enough to enable promotion of electrons to the conduction band through means of heat, electric fields or light are classified as semiconductors, which are the workhorse of solid state electronics due to their controllable conductivity. Insulators on the other hand have such large band gaps that their conductivity is negligible under normal circumstances. For semiconductors, there is an important distinction between two kinds of band gaps. When the electronic states at the conduction band minimum (CBM) and the valence band maximum (VBM) belong to the same k-vector, the bandgap is classified as direct. If instead the VBM and CBM have different k-vectors, the material is classified as having an indirect bandgap. This distinction is important for example in optical considerations: in direct bandgap materials, electron-hole pairs (excitons) may recombine by emitting a photon of light with an energy equal to the bandgap magnitude. For materials with an indirect bandgap, this radiative recombination is limited since the emitted photon does carry enough momentum to satisfy the conservation of k-vector. Radiative recombination can still occur when other actors like phonons or crystal defects can absorb the excess momentum.

Effective carrier mass: Under the influence of the lattice potential, electrons and holes in crystals respond to external forces as if they are free particles with an altered mass. This is known as the effective mass m^* of the carriers and is typically reported in units of the rest mass of the electron $m_e = 9.109 \cdot 10^{-31}$ kg. The effective mass is an intrinsically important quantity for next-generation field-effect transistors, where an optimal effective mass is needed to balance channel backscattering and tunneling leakage effects [20]. More generally, the effective mass is an important factor determining the transport properties of charge carriers in crystals and is closely related to the carrier mobility, which is one of the main figures of merit in the performance of field-effect transistors. In this section, we summarize the theoretical foundations of the concept of effective mass and its relation to other measurable electronic properties.

In order to derive the concept of effective mass of charge carriers in crystals, we make an analogy between free particles and those in a crystal.[30]. For free particles, their (non-relativistic, intertial) mass is defined by Newton's second law

$$\frac{d\boldsymbol{p}}{dt} = m\boldsymbol{a} = \boldsymbol{F}, \tag{2.4}$$

where $\vec{p}$ is the momentum of the particle, $\vec{a}$ its acceleration and $\vec{F}$ the sum of all forces acting on the particle.

Since the charge carriers in crystals have Bloch wavefunctions which are not momentum eigenstates, we will look for a modified version of Newton's second law of the form

$$\frac{d\boldsymbol{p}_{crystal}}{dt} = \hbar\frac{d\boldsymbol{k}}{dt} = m\boldsymbol{a} = \boldsymbol{F}_{ext}, \tag{2.5}$$

where $\boldsymbol{p}_{crystal} = \hbar\boldsymbol{k}$ is the pseudomomentum of the carrier and $\boldsymbol{F}_{ext}$ is the total external force applied on the carrier, excluding forcing originating from the crystal lattice. The acceleration can be found by taking the time derivative of the velocity, which for a charge carrier in a crystal is defined by the group velocity of its Bloch wavepacket:

$$\boldsymbol{a} = \frac{d\boldsymbol{v}_g}{dt} = \frac{1}{\hbar}\frac{d}{dt}\frac{dE(\boldsymbol{k})}{d\boldsymbol{k}}. \tag{2.6}$$

Combining this with equation (2.5) yields a form of Newton's second law applicable to electrons and holes in crystals:

$$\boldsymbol{F}_{ext} = \hbar^2\left(\frac{d^2E(\boldsymbol{k})}{dk_i dk_j}\right)^{-1}\boldsymbol{a}, \tag{2.7}$$

From this result it can be seen that the effective mass of the charge carriers depends both on their k-vector and the direction in which they are accelerated. The effective mass at any point in k-space can be found by calculating the second derivative of the electronic energy bands $E(\boldsymbol{k})$ at that k-point in the desired direction. The two most-used methods for this are parabolic fitting, where the quadratic coefficient equals the local second derivative of band, and using a finite difference scheme to calculate the second derivative.

Experimentally, direct measurements of the effective mass are not straight-forward, as they can only be measured by complicated techniques like cyclotron resonance or angular-resolved photo-emission spectroscopy. Instead, the effective mass is usually measured indirectly by measuring the carrier mobility. This quantity is defined as

$$\boldsymbol{v}_{drift} = \mu\boldsymbol{E}, \tag{2.8}$$

where v_{drift} is the drift velocity of the carriers effectuated by an externally applied electric field of strength $|E|$. From a derivation based on kinetic theory [30], the mobility μ can be shown to depend on the effective mass of the carriers and the average time between scattering events $\bar{\tau}$ as

$$\mu = \frac{e}{m^*}\bar{\tau}, \tag{2.9}$$

where e is the charge of the electron. The mobility can be calculated by exploiting its relation to the electrical conductivity σ and carrier concentration n:

$$\sigma = ne\mu. \tag{2.10}$$

In thin crystals, the conductivity can be measured by the four-point-probe method and the carrier concentration can be obtained through Hall voltage measurements, such

that the mobility can be calculated. Note that this still leaves the scattering time $\bar{\tau}$ unknown, such that quantitative results for the effective mass cannot be obtained in this way. Only under the assumption of a nearly constant scattering time can trends in the mobility be expected to correspond to trends in the effective mass.

Density of states (DoS): The density of states is a way of visualizing the electronic states in a crystal that is complementary to the band structure. In three-dimensional crystals, the Brillouin zone is three-dimensional, and only a small subset of the k-vectors within the Brillouin zone is represented. While this is sufficient for extracting information about the bandgap and effective carrier mass, it yields an incomplete picture about the total number of electronic states in the system. In a plot of the density of states, the number of states within a small energy interval is drawn as a function of their energy. At the expense of discarding any k-information about these states, DoS plots give a good impression of the distribution of states on the energy scale throughout the whole Brillouin zone.

2.3 Calculation methods

In order to calculate the electronic band structure, the quantum many-body problem needs to be solved for the many-electron wavefunction. Concretely, the quantum many-body problem of determining the state of N electrons in a static environment of atomic nuclei is encompassed by the Schrödinger equation

$$\hat{H}\Psi(r_1, r_2, ..., r_N) = E\Psi(r_1, r_2, ..., r_N), \tag{2.11}$$

where Ψ is the many-body wavefunction with a dependence on the positions of all N electrons, E is the total energy of the system and $\hat{H}$ is the Hamiltonian operator

$$\hat{H} = \hat{T}_e + \hat{V}_{ee} + \hat{V}_{en} \tag{2.12}$$

consisting of the electron kinetic energy $\hat{T}_e$, electron-electron potential energy $\hat{V}_{ee}$ and electron-nucleus potential energy $\hat{V}_{en}$ operators. Only for $N = 1$ can equation 2.11 be solved exactly: like its classical counterpart, the quantum many-body problem allows no analytic solutions. Numerical evaluations are possible for $N > 1$, but the complexity of these calculations quickly rises as N increases, making this approach viable only for the smallest atoms or molecules. To proceed further, approximations have to be made. The two most succesful branches of approximation methods are those based on expansion of the wavefunction into independent single-electron wavefunctions and those that evaluate the wavefunction using the electron density as an intermediary quantity. Though the density functional theory framework employed in this work belongs to the second branch, it is commonly used in conjunction with techniques of the other branch, making it worthwhile to discuss both.

Single-particle wavefunction approximations

One useful, though rather crude simplification of the quantum many-body problem is to neglect electron-electron interaction altogether and approximate the full N-electron wavefunction Ψ with a product of N single-electron wavefunctions ψ:

$$\Psi(r_1, r_2, ..., r_N) = \psi_1(r_1) \cdot \psi_2(r_2) \cdot ... \cdot \psi_N(r_N). \tag{2.13}$$

Of course, we cannot expect accurate results if we pretend that each electron is alone in the material. The least we can do is let each electron feel the average effect of the presence of all the other electrons: this can be achieved by letting the single-electron wavefunctions ψ be solutions to a single-particle Schrödinger equation with a modified potential representing both the nuclei and all the other electrons in the material. In this way, charge screening, an important effect which is responsible for the shielding of the nuclear charge by electrons, can be described by this model. This model for the electronic structure is known as the Hartree method.

One of the deficiencies of the Hartree model is that it does not handle so-called exchange interactions. These stem from the Pauli exclusion principle, which states that no two fermions (electrons) can occupy the same state. Mathematically, this is equivalent to the multi-electron wavefunction flipping its sign upon exchange of two electrons, hence the name "exchange interaction". The Hartree wavefunction (equation 2.13) does not obey this rule: it is invariant under exchange of electron coordinates. The Hartree method can be extended to incorporate Pauli exclusion effects by instead expressing the N-electron wavefunction as a matrix determinant of single-particle wavefunctions

$$\Psi(r_1, r_2, ..., r_N) = \frac{1}{\sqrt{N}} \begin{vmatrix} \psi_1(r_1) & \psi_1(r_2) & \dots & \psi_1(r_N) \\ \psi_2(r_1) & \psi_2(r_2) & \dots & \psi_2(r_N) \\ \vdots & \vdots & \ddots & \vdots \\ \psi_N(r_1) & \psi_N(r_2) & \dots & \psi_N(r_N) \end{vmatrix}. \tag{2.14}$$

Since the determinant of a matrix flips its sign under exchange of two columns, the resulting superposition of single-electron wavefunctions is indeed antisymmetric under exchange of electron coordinates. This kind of determinant is known as a Slater determinant, and the method of expressing the N-electron wavefunction as a single Slater determinant is referred to as the Hartree-Fock method.

Though a great improvement over the Hartree model, in the Hartree-Fock model the electrons still only experience an average effect of all other electrons, which means that individual electron-electron interactions are not represented. Various methods exist for accounting for this so-called correlation interaction. These methods, collectively known as post-Hartree-Fock methods, generally either include additional Slater determinants (configuration interaction [33]) or treat the interaction in a perturbative manner (e.g. coupled-cluster [33] and Møller-Plesset perturbation theory [34]).

A major benefit of the (post-)Hartree-Fock methods is that the exchange (Pauli exclusion) energy is treated in an exact way, something that is still impossible for the

electron density-based methods discussed next. It is for this reason that for many high-accuracy density functional calculations, a hybrid approach is used where some of the exact exchange energy is borrowed from a Hartree-Fock calculation.

Electron density-based approximations

While Hartree-Fock and post-Hartree-Fock calculations can yield very precise results, their scalability is poor, as the computational complexity rises dramatically with increasing system size. Thus, people have sought for alternative approximations for electronic structure calculations. A very successful class of approximations is those based on finding the electronic structure through the intermediary quantity of the electron density. Before discussing density functional theory (DFT), the modern workhorse of electronic structure and quantum chemistry calculations, it is instructive to discuss its closely related but conceptually simpler predecessor, the Thomas-Fermi model [35]. This was the first attempt at expressing the total energy of an electronic system in terms of the electronic density. In this model, the total energy is expressed as the sum of the kinetic energy of the electrons, the potential energy of the electron-electron interactions and the potential energy of the electron-nucleus interactions:

$$E_{TF}[n(\boldsymbol{r})] = T_e + V_{ee} + V_{en}. \tag{2.15}$$

The kinetic energy is approximated using the analytic expression derived for the case of a homogeneous electron gas [36]:

$$T_e = \frac{3h^2}{40m_e}\left(\frac{3}{\pi}\right)^{2/3}\int n(\boldsymbol{r})^{5/3}\boldsymbol{dr}, \tag{2.16}$$

while the potential energies are modeled through classical electrostatic Coulomb interaction

$$V_{en} = \int q_e n(\boldsymbol{r}) v(\boldsymbol{r})\boldsymbol{dr} \tag{2.17}$$

and

$$V_{ee} = \frac{1}{2}q_e^2\int\int\frac{n(\boldsymbol{r})n(\boldsymbol{r'})}{|\boldsymbol{r}-\boldsymbol{r}|}\boldsymbol{dr}\boldsymbol{dr'}. \tag{2.18}$$

As the total energy thus depends on the energy density which is itself a function of position, the energy is said to be a functional of the electron density. Though conceptually transparent, this model does have some shortcomings. For one, the analytic expression of the kinetic energy is valid only for a homogeneous electron gas. While this might be a reasonable approximation for metals, it can not be expected to be generally applicable to other materials. Additionally, the model accounts neither for correlation (individual electron-electron interaction) nor for exchange (Pauli exlusion) effects. The latter issue was alleviated somewhat by Dirac [37], who added to the energy

sum in equation 2.15 an exchange contribution, which he derived for the case of the homogeneous electron gas (HEG):

$$E_x^{HEG}[n(\boldsymbol{r})] = -\frac{3}{4}\left(\frac{\pi}{3}\right)^{1/3}\int n(\boldsymbol{r})^{4/3}d\boldsymbol{r} \tag{2.19}$$

However, mainly due to its crude approximation of the true kinetic energy in a non-homogenous electronic structure, the Thomas-Fermi model only has limited applicability. It was not until the 1960s that the full potential of density-based electronic structure calculations was discovered.

2.4 Density Functional Theory

The rise of modern density-functional theory started with the publication of a ground-breaking paper by Hohenberg and Kohn in 1964 [38]. In it, they proved that for any electronic system 1) there is a one-to-one correspondence between the wavefunction (and hence the energy) and the electronic density of the ground state $\psi_0(\boldsymbol{r_1}, \boldsymbol{r_2}, ..., \boldsymbol{r_N}) \leftrightarrow n_0(\boldsymbol{r})$ and that 2) the energy of the system $E = E[n(\boldsymbol{r})]$ has the variational property that its value is minimal (and equal to the exact ground-state energy) for the ground-state electron density. Taken together, these theorems show that the complete electronic structure of any system can be obtained by minimizing the energy functional $E = E[n(\boldsymbol{r})]$. This proof of the existence of a universal density functional is remarkable, but says nothing about the mathematical form of the functional: how exactly the energy depends on the electron density was not addressed. However, in the next year, Kohn and Sham [39] demonstrated a practical way of applying the Hohenberg-Kohn theorems for actual calculations. First, they isolated the unknown part of the energy functional by expanding the functional to

$$E[n(\boldsymbol{r})] = T^{ni}[n(\boldsymbol{r})] + V_{ee}^{C}[n(\boldsymbol{r})] + V_{en}^{C}[n(\boldsymbol{r})] + E_{XC}[n(\boldsymbol{r})], \tag{2.20}$$

where $T^{ni}[n(\boldsymbol{r})]$ is the kinetic energy of an equivalent system with non-interacting electrons, $V_{ee}^{C}[n(\boldsymbol{r})]$ and $V_{en}^{C}[n(\boldsymbol{r})]$ are the classical electrostatic electron-electron and electron-nucleus Coulomb interactions and $E_{XC}[n(\boldsymbol{r})]$ contains the unknown exchange (Pauli exclusion) and correlation (individual electron-electron interaction) contributions to the total energy.

Next, the nuclear potential is substituted for an effective single-particle Kohn-Sham potential which includes a term for the average interaction with all other electrons and a term representing the exchange and correlation interactions

$$v_{KS}(\boldsymbol{r}) = v_{nucl}(\boldsymbol{r}) + v_{ee}(\boldsymbol{r}) + v_{XC}(\boldsymbol{r}) \tag{2.21}$$

where the average electron-electron interaction is again modeled by the Coulomb interaction

$$v_{ee}(\boldsymbol{r}) = \frac{\partial V_{ee}[n(\boldsymbol{r})]}{\partial n(\boldsymbol{r})} = \int \frac{n(\boldsymbol{r}')}{|\boldsymbol{r} - \boldsymbol{r}'|} d\boldsymbol{r}' \tag{2.22}$$

and the exchange-correlation potential can be implicitly written as depending on some exchange-correlation energy functional

$$v_{XC}(\boldsymbol{r}) = \frac{\partial E_{XC}[n(\boldsymbol{r})]}{\partial n(\boldsymbol{r})}. \tag{2.23}$$

Finally, for a system of N electrons, solving a system of N one-electron Schrödinger equations of the form

$$\left(-\frac{1}{2m_e}\nabla^2 + v_{KS}(\boldsymbol{r})\right)\psi_i(\boldsymbol{r}) = \epsilon_i \psi_i(\boldsymbol{r}) \tag{2.24}$$

yields an electron density $\sum_i |\psi_i(\boldsymbol{r})|^2$ which is equal to the ground-state electron density of the original system of interacting electrons. Solving the system of equations requires an iterative approach since the effective potential itself depends on the electron density. This involves first solving the equations using a trial wavefunction or charge density as input, after which the output wavefunction or charge distribution is used as input and the equations are solved again. This last step is repeated until the input and output differ by less than a predetermined tolerance. At this point, the input and output wavefunctions are said to be self-consistent and hence this approach to solving the equations 2.24 is also known as the self-consistent field method.

The Kohn-Sham formalism to density functional theory described above has higher accuracy than the Thomas-Fermi model mainly due to the different way in which the kinetic energy is approximated. In the Thomas-Fermi model, the kinetic energy is calculated under the assumption that the system is a homogeneous electron gas. In Kohn-Sham DFT, this approximation is not necessary as the kinetic energy is instead evaluated by applying the quantum-mechanical kinetic energy operator to the non-interacting Kohn-Sham orbital wavefunctions.

However, one particular deficiency of the Thomas-Fermi model is still a persisting problem in Kohn-Sham DFT: the lack of an exact description of exchange and correlation interactions. Although the Hohenberg-Kohn paper proves that a universal functional linking the total energy to the electron density exists, its exact formulation is still an unsolved problem. Instead, density functional calculations rely on approximate functionals describing the exchange and correlation contributions to the total energy. Some of the most-used types of these approximate functionals are described in the next section.

Exchange-correlation functionals

In the absence of an exact description of the exchange (Pauli exlusion) and correlation (individual electron-electron interaction) contributions to the total energy of an electronic

system, DFT calculations have to rely on approximations to these contributions. In their 1964 paper [38], Hohenberg and Kohn proposed the first of these approximations, building on the already available knowledge of the homogeneous electron gas (HEG). The exchange energy for this system was already derived analytically by Dirac [37] (equation 2.19), while for the correlation contribution Hohenberg and Kohn derived analytic expressions in the limits of high and low electron density. Since in these functionals the exchange-correlation energy density only depends on the local value of the electron density, these HEG-derived functionals are referred to as the local density approximation (LDA). This approximation works surprisingly well considering its simplicity, and has been used extensively in solid state calculations for many years. Its success can be attributed mostly to two factors. Firstly, although the shape and position of the exchange-correlation-induced distortions in the electron density are described poorly by the LDA approximation, the spherical averages of these distortions are remarkably accurate [40], and it is this average that is the primary factor contributing to the electron-electron interaction energy. Secondly, it has been shown that although the individual exchange and correlation contributions to the energy calculated by the LDA method are not very accurate, the errors in these two terms tend to cancel out in important cases [41]. However, the LDA approach still has its shortcomings. Binding energies are typically overestimated [40], leading to underestimated bond lengths and lattice constants. Additionally, band gap energies of insulators and semiconductors are often underestimated.

A more sophisticated exchange-correlation functional can be devised when not only the local density, but also the local gradient in the density are considered. This approach is known as the generalized gradient approximation (GGA). It is also classified a semi-local functional, as the gradient at a point carries some information about the immediate environment around that point. The functional of this kind that is most widely used both due to its accuracy and mathematical simplicity is that of Perdew, Burke and Ernzerhof (PBE) [42]. This functional is used for all DFT calculations in the present work.

It is worth noting that there are other exchange-correlation functionals that further improve on the GGA, at the price of a higher computational cost. Meta-generalized gradient approximation (MGGA) functionals [43] include higher order density gradients or a kinetic energy density depedence to improve their accuracy. Additionally, hybrid functionals are a class of functionals that combine part of the exact Hartree-Fock exchange energy with the conventional GGA functionals. For example, the PBE0 functional mixes three quarters of the PBE exchange energy with one quarter of the Hartree-Fock energy [44]. At the far end of the spectrum are methods that model the exchange-correlation energy in a fully non-local way, such as the weighted density approximation (WDA) [45]. While these methods are the most physically accurate, they evaluate the exchange-correlation energy through a nested integral of the electron density, greatly increasing the computational cost.

Van der Waals forces

As a special case of correlation effects, dispersion forces like the Van der Waals interaction are generally poorly described by the approximate correlation functionals used in DFT calculations. Since the inter-layer interactions in the 2D transition metal dichalcogenides studied in this work are of a Van der Waals nature, a correction for dispersion effects is needed in order to obtain an accurate description of these materials. To this end we employ the DFT-D3 dispersion correction by Grimme [46] [47] [48].

Basis sets

In order to simplify the numerical evaluation of the hamiltonian, which typically has to be performed tens of thousands of times during a DFT calculation, the electronic wavefunctions are built up from elements which have a mathematically simple inner product with the hamiltonian. The total hamiltonian is then evaluated by summing the inner products with all of those partial elements of the wavefunction. The group of these elements is called the basis set, and a good basis set should be able to closely approximate the true wavefunction with only as few elements as possible. Two types of basis sets are most commonly used. Firstly, basis sets of localized orbitals consist of atomic-like orbitals which are centered on specific points in space. Hence, its use is also referred to as the method of linear combination of atomic orbitals (LCAO). Though the LCAO method is mostly used in the field of quantum chemistry, the closely related method of tight-binding is often used outside the framework of DFT to calculate the electronic structure of systems whose large size makes DFT calculations unpractical [49].

Plane-waves

Since the factor $u_n(\boldsymbol{r})$ of the Bloch wavefunction has the same symmetries as the crystal lattice, its Fourier decomposition consists only of plane-waves with wavevectors equal to crystal lattice vectors

$$u_n(\boldsymbol{r}) = \sum_{\boldsymbol{G}} c_{n,G} e^{i\boldsymbol{G}\cdot\boldsymbol{r}}, \tag{2.25}$$

such that the complete wavefunction (equation 2.2) can be written as a superposition of plane-waves

$$\psi_{n,k}(\boldsymbol{r}) = \sum_{\boldsymbol{G}} c_{n,\boldsymbol{G}'} e^{i(\boldsymbol{k}+\boldsymbol{G})\cdot\boldsymbol{r}}. \tag{2.26}$$

Thus, plane-waves constitute a useful set of basis functions for use in DFT calculations. The exact solution requires the summation in equation 2.26 to run over the infinitely many reciprocal lattice vectors. In practice the summation is truncated in

in order to make it computationally feasible. In this way, only plane-waves below a certain cutoff energy E_{cut} are included:

$$\frac{1}{2}\left|\boldsymbol{k}+\boldsymbol{G}\right|^2 \leq E_{cut}. \tag{2.27}$$

This approach provides a clean systematic way of improving the accuracy of the calculation by increasing the cutoff energy, which is a benefit over localized basis sets.

Brillouin zone sampling

Many quantities of interest for an electronic system like the density or the total energy are given by integrals over the Brillouin zone. Computationally, these integrals have to be discretized, thus approximating them by a finite weighted sum over a set of points within the Brillouin zone (k-points). A number of schemes for finding "mean-value" or "representative" k-points have been proposed in literature [50] [51] [52] [53]. In the calculations performed in this work, we employ the method of Monkhorst and Pack [54], in which a regular lattice-commensurate grid of k-points is evaluated. The accuracy can be systematically improved by using a finer grid, facilitating convergence checks of the system energy with respect to the k-point sampling. Careful optimization of the amount of evaluated k-points is desirable since too coarse sampling will decrease the accuracy of the calculation while an overly fine sampling will unnecessarily increase the computational complexity.

Pseudopotentials and augmented plane-waves

Density functional calculations with plane-wave basis sets face a challenge in the core regions of atoms. In these regions the electron density is high and many one-electron wavefunctions overlap. As a result, the wavefunctions exhibit high-frequency spatial oscillations in these core regions in order to maintain their required orthogonality. This presents convergence issues for the plane-wave DFT as high-frequency plane-wave components are needed to accurately model these regions. Several workarounds have been developed to mitigate this issue and keep the required cutoff energy for plane-wave DFT calculations low without sacrificing accuracy.

In the pseudopotential method, the core electrons are kept fixed and are represented by an effective potential around the nuclei which is much smoother than the full Kohn-Sham potential, but coincides with it beyond a certain convergence radius. The Kohn-Sham equations are then solved only for the valence electrons, requiring less high-frequency plane-wave components and thus simplifying the calculation. An added benefit is that relativistic effects, which are only significant for core orbitals, do not need to be included in the calculation as long as the pseudopotentials have been constructed with regard for relativistic effects.

In the augmented plane-wave (APW) method [55], the plane-wave basis set is augmented with superpositions of atomic orbitals centered at the nuclei. In this

way, the electronic system is separated into two kinds of regions: around the nuclei, where potentials and wavefunctions vary rapidly, the wavefunctions are described as atomic orbitals, and in the interstitial regions between nuclei the wavefunctions are expanded into plane-waves. At the boundary regions, continuity of the wavefunction is enforced. In this method, the core electron wavefunctions are thus explicitly evaluated, leading potentially to higher accuracy but also higher computational cost compared to pseudopotential methods.

The projector-augmented wave method introduced by Blöchl [56] provides a theoretical framework which connects the full all-electron wavefunction to a more manageable smooth wavefunction through a transformation operator. This transformation makes the auxiliary wavefunction much smoother in the core regions, much like the pseudopotential method does. The difference is that in the PAW framework, these auxiliary wavefunctions can be transformed back into the full all-electron wavefunction. In this way, the computational efficiency of smoother wavefunctions (as in the pseudopotential method) is combined with the accuracy of an all-electron calculation (as in the APW method). The PAW method is used for all the DFT calculations in this work.

2.5 Summary

In the rest of this thesis, we will employ Kohn-Sham density functional calculations to investigate the electronic structure of 2D transition metal dichalcogenides and their alloys by means of their electronic band structure. The calculations are performed in the projector-augmented wave formalism as implemented in the VASP software package. Brillouin-zone integrals are evaluated by the k-space sampling method of Monkhorst and Pack. The exchange and correlation contributions to the Hamiltonian are approximated by the generalized gradient functional of Perdew, Burke and Ernzerhof (PBE) and the van der Waals interactions between the TMD layers are corrected for by the DFT-D3 method of Grimme.

Chapter 3

Pristine Transition Metal Dichalcogenides and Point Defects

This chapter is aimed at gaining insight into the structural, vibrational and electronic properties of the transition metal dichalcogenides MoS_2 and WS_2. TMDs can take on several different crystal phases, the most ubiquitous being the 2H (2 layers per unit cell, hexagonal) and 1T (one layer per unit cell, tetragonal) phases. For MoS_2 and WS_2, the 2H phase is the most energetically favorable structure, hence the discussion in this chapter will be based on this structural phase of TMDs. We will discuss the crystal structure of the 2H phase of TMDs and list the experimentally known lattice constants of MoS_2 and WS_2 which we will use as one of the benchmarks for our ab-initio calculations. The vibrational modes of the crystal structure are discussed in the context of Raman spectroscopy, a technique that is highly sensitive to structural changes in TMDs. We demonstrate the possibility of calculating lattice vibration frequencies in TMDs with DFT, which we will exploit in an extensive phonon analysis of TMD alloys in the next chapter. The electronic structure of 2H-phase TMDs is explicated by first discussing its general features which are dictated by the crystal structure. After this introduction, we discuss the methods and results of our ab-initio calculations of the structural and electronic properties of MoS_2 and WS_2, comparing them to our benchmarks. Additionally, we extend our ab-initio calculations to the study of realistic concentrations of point defects typically found in synthesized TMDs. This requires the adoption of a supercell calculation method and unfolding of the resulting eigenstates in order to obtain an effective band structure that can be interpreted and compared to those of the pristine materials.

3.1 Crystal structure

Figure 3.1 shows the crystal structure of the 2H phase of TMDs. Each 2D atomic layer consists of a layer of metal atoms sandwiched between chalcogen atoms, where the chalcogen atoms form a trigonal prismatic shape around the metal atoms (figure

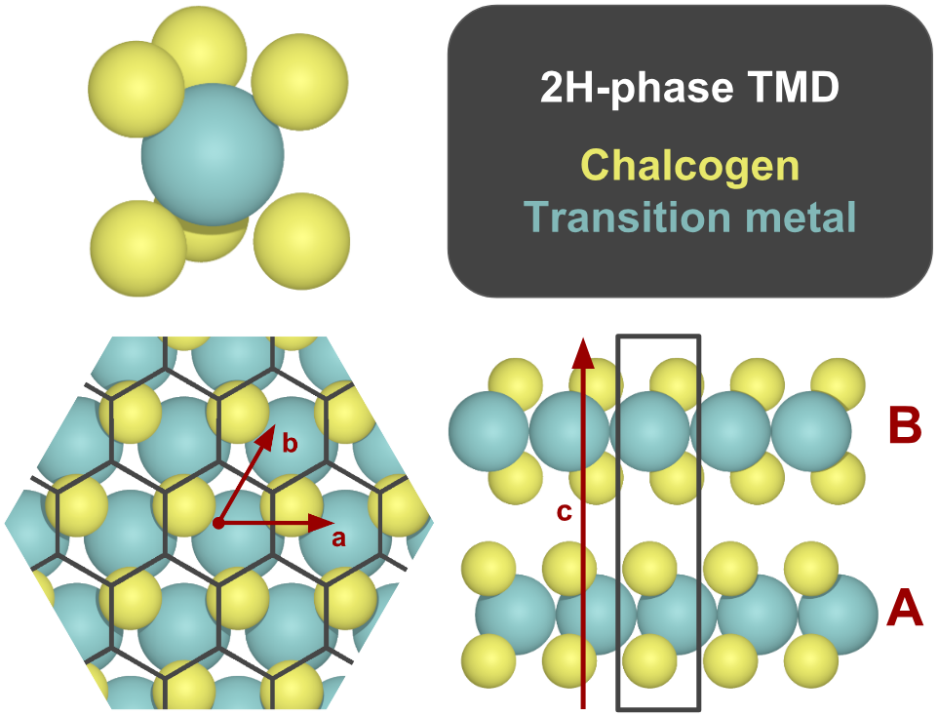

Figure 3.1: The crystal structure of 2H-phase transition metal dichalcogenides such as MoS_2 and WS_2. Top: conventional unit cell highlighting the trigonal prismatic symmetry of the atomic layers. Bottom-left: top view of a monolayer of MoS_2 with overlay of a possible choice of unit cell emphasizing the hexagonal symmetry of the crystal lattice. Bottom-right: side view of the same crystal, demonstrating the AB stacking order of the atomic layers characteristic to the 2H crystal phase. The length of the c axis is twice the interlayer distance since the unit cell contains two atomic layers.

3.1a). The monolayers have hexagonal symmetry (figure 3.1b) and they are stacked in an AB pattern in the bulk material. The in-plane and out-of-plane lattice constants of MoS_2 and WS_2 are summarized in table 3.1. These numbers clearly demonstrate the exceptional structural similarity between these two materials: their lattice parameters differ by less than half a percent. This structural similarity is what allows MoS_2 and WS_2 to be combined into alloys without distorting their crystal structure, which is explored in the next chapter. The crystal structure of MoS_2 and WS_2 is closely related to their vibrational modes, which are a valuable metrics in the experimental characterization of these materials, as explained in the next section.

Table 3.1: In-plane (a) and out-of-plane (c) lattice constants of the transition metal dichalcogenides MoS_2 and WS_2.

TMD	**a (nm)**	**c (nm)**
MoS_2	0.316	1.23
WS_2	0.316	1.24

3.2 Vibrational structure

Since the unit cell of 2H-phase TMDs contains $N = 6$ atoms, it has $3N = 18$ degrees of freedom. This means that these crystals have $3N - 3 = 15$ vibrational eigenmodes, not counting the 3 modes that correspond to a homogeneous translation of the whole crystal. These lattice oscillations are illustrated in figure 3.2. The oscillations may have different wavelengths, such that a phononic band structure can be constructed where the vibrational frequencies of the eigenmodes are graphed as a function of k-vector within the Brillouin zone, fully analogous to the electronic band structure. For experimental measurement of these vibrations, generally either infrared absorbance spectroscopy or Raman scattering spectroscopy are used. These two techniques have different selection rules for what vibrations they can measure: only vibrations where the electric dipole moment changes can absorb IR light, while only vibrations where the electric polarizability changes can scatter Raman light. In the next chapter we will use Raman spectroscopy to study lattice vibrations in TMD alloys, motivated by the technique's quick, substrate-independent nature and its suitable frequency window for studying the predominantly low-frequency lattice vibrations in TMDs. Raman scattering is only efficient when the atoms in the lattice vibrate in phase such that, in general, only phonons at the Γ point can be measured with this technique. Exceptions arise when crystal symmetry is broken by the presence of defects or if absorption is exceptionally strong, as is the case when the excitation laser frequency matches an electronic transition in the material. In particular, both these effects are known to cause the emergence of a longitudinal acoustic phonon originating from the M-point of the Brillouin zone in the Raman spectra of WS_2 [57, 58, 59]. The Raman-active vibration modes of 2H-phase TMDs are denoted by an R in figure 3.2. IR denotes active infrared-absorbing modes, while IN denotes inactive modes. Of the Raman-active modes, the very low-frequency E^2_{2g} mode cannot be resolved by regular Raman spectroscopy, leaving three modes to be measured: A_{1g}, E_{2g} and E_{1g}. Of these three, especially the A_{1g} and E_{2g} contain a lot of information about the structure of the TMD. Their frequencies can serve as a measure of the number of layers [57] as well as a for strain in the material [60]. Additionally, the peak ratio of these two vibrations from polarized Raman measurements gives insight into the orientation distribution in nanocrystalline TMDs. Evidently, the vibrational modes are important diagnostics in characterizing TMDs, and their theoretical evaluation would be highly valuable. In section 3.4.3 we discuss the calculation of the frequency of the A_{1g} mode in MoS_2 and WS_2 by density functional theory, which we extend to our study of TMD alloys in chapter 4.

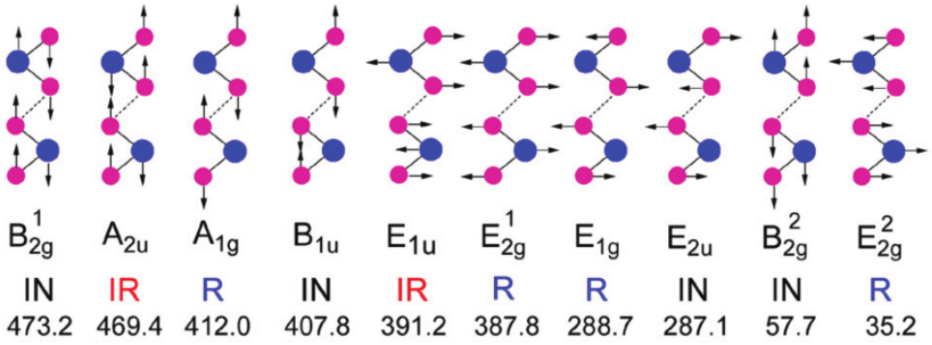

Figure 3.2: Vibrational eigenmodes of bulk 2H-phase transition metal dichalcogenides[61]. Each E mode is doubly degenerate in the in-plane directions, giving a total of $3N - 3 = 15$ eigenmodes where $N = 6$ is the number of atoms per unit cell. The modes are labeled as active in infrared absorption (IR), active in Raman scattering (R) or inactive (IN) and their vibrational frequencies in MoS_2 are indicated in cm^{-1}.

3.3 Electronic structure

Our goal is the calculation of electronic properties such as the bandgap and electron effective mass from band structure diagrams which we calculate through ab-initio techniques. In order to become familiar with the band structure of transition metal dichalcogenides, we first derive the shape of the Brillouin zone of TMDs from their crystal structure. Next, we demonstrate how the shape of the Brillouin zone determines the general shape of the band structure of these materials by constructing a simplified band structure through the empty lattice approximation. This exposition serves as a preparation for the next section, where we present the results of the ab-initio calculations of the electronic structure of MoS_2 and WS_2.

The Brillouin zone

As discussed in chapter 2, the wavefunctions describing electronic energy eigenstates in crystals are Bloch functions which are characterized by a discrete index n and a continuous wavevector $\vec{k}$. These wavefunctions, and thus all their derived properties, are periodic in k-space, such that we may define a unit cell in k-space which is called the Brillouin zone. The shape of the Brillouin zone of any material is uniquely determined by the crystal structure of the material, and is an important factor in determining what the electronic band structure of the material looks like. The geometry of the Brillouin zone of 2H-phase TMDs can be derived by using the definitions of the reciprocal unit vectors as given in section 2.2.1. When applying these relations, we find that the Brillouin zone of 2H-phase TMDs has a hexagonal prismatic shape like the real-space unit cell, though it differs from the real-space unit cell in its shape and orientation. More specifically, it is rotated by 30 degrees with respect to the real-space unit cell

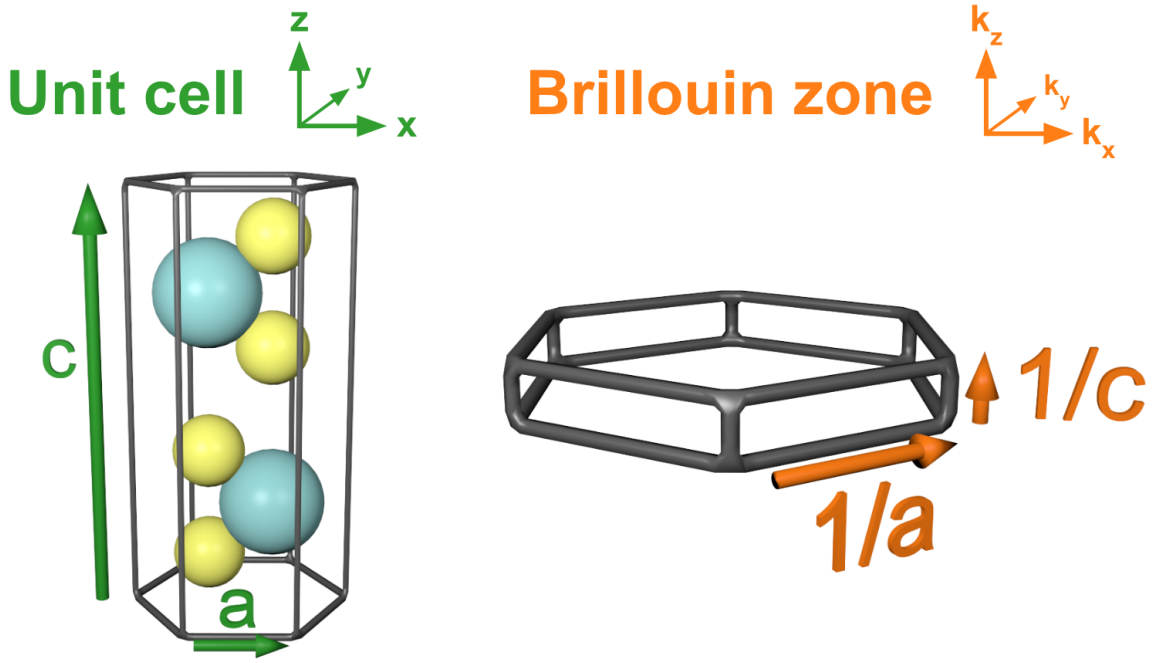

Figure 3.3: The three-dimensional unit cell of 2H phase TMDs and their Brillouin zone. The Brillouin zone is rotated along the vertical axis by 30 degrees with respect to the real-space unit cell, and its height over width ratio is the inverse of the real-space unit cell. Since the real-space unit cell contains two atomic layers, it is rather tall, leading to a relatively flat Brillouin zone.

and its height over width ratio is the inverse of that of real-space unit cell. Since the real-space unit cell is rather tall, the resulting Brillouin zone is relatively flat (figure 3.3). In order understand how these geometrical considerations influence the band structure of 2H-phase TMDs, we derive a simplified band structure based on only these geometrical properties in the next section.

Empty-lattice band structure

The empty-lattice approximation is a method to derive a simplified band structure of a material based only on the geometry of the crystal lattice and the energy-momentum relationship of free electrons. It does not provide a physically accurate description of the band structure as it completely ignores the influence of the atomic potential on the electrons in the crystal, but the empty lattice approximation is a useful tool in understanding the general features of the band structure which we will calculate more accurately using density functional theory in section 3.4.

An empty-lattice band structure is constructed by centering a parabolic free-electron energy-momentum curve at every lattice point in k-space. The pattern of overlapping parabolas within the first Brillouin zone then represents the band structure. In figure

3.4, this is demonstrated for a one-dimensional crystal, resulting in a simple band structure. For the real, three-dimensional crystals we are interested in, there are two main sources of additional complexity in their empty-lattice band structures. Firstly, for all Brillouin zone shapes except cubical ones, the spacing between Brillouin zones is different in different k-directions. For the case of 2H-phase TMDs, the Brillouin zone is a very flat hexagonal prism (figure 3.3), such that they are packed more closely together in the k_z direction than in the k_x and k_y directions. This leads to more complex overlap patterns in the empty-lattice band structure. Additionally, band structures of three-dimensional crystals have to be represented by choosing a path through the Brillouin zone and graphing the electronic energy for wavevectors on this path only. Both of these effects can be seen in the empty-latttice band structure of a 2H-phase TMD in figure 3.5, in which only bands originating from nearest-neighbouring Brillouin zones were included. As expected and as also seen in the one-dimensional case, we note a parabolically increasing electron energy as the magnitude of the k-vector increases from the Γ point to the K point, as well as from Γ to M. The path along the perimeter of the Brillouin zone from M to K is accompanied by only a slight variation in wavevector magnitude, which is reflected by the relatively flat energy bands in this part of the diagram. Additionally, many bands are degenerate, which is indicated by the opacity of the lines in the diagram. These duplicate bands originate from the symmetry of the Brillouin zone. For example, since the spacing to the next Brillouin zone in the $+k_z$ and $-k_z$ directions is the same, both these cells contribute an identical band to the diagram. In a full calculation of the band structure of TMDs, these degeneracies will be lifted by the influence of the potential that the electrons experience in the crystal, leading to the splitting of degenerate bands and the formation of bandgaps [30]. Another feature that will also be present in the full band diagram and has an intuitive explanation in the case of the empty-lattice band diagram is the observed "doubling" of bands: every band is accompanied by another band at a slightly higher energy. This is again a consequence of the geometry of the Brillouin zone: the small spacing between unit cells in the k_z direction results in a pattern of overlapping parabolas which are only very slightly displaced from each other in the k_z direction.

Now that the general shape of the electronic band structure of 2H-phase TMDs has been introduced through the simplistic but insightful empty-lattice approximation, we will calculate the physically accurate band structure by means of density functional theory in the next section.

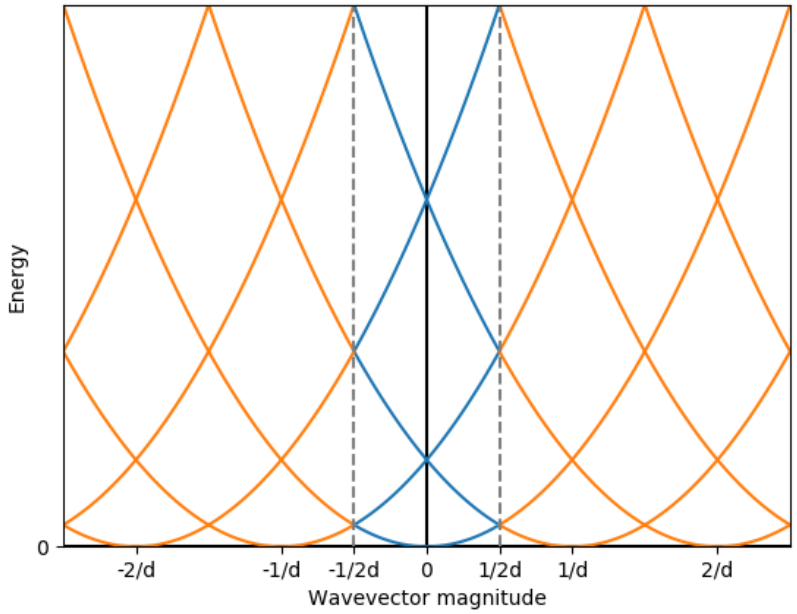

Figure 3.4: In one dimension, the empty lattice approximation leads to simple band structure inside the first Brillouin zone consisting of overlapping parabolas centered on neighbouring Brillouin zones.

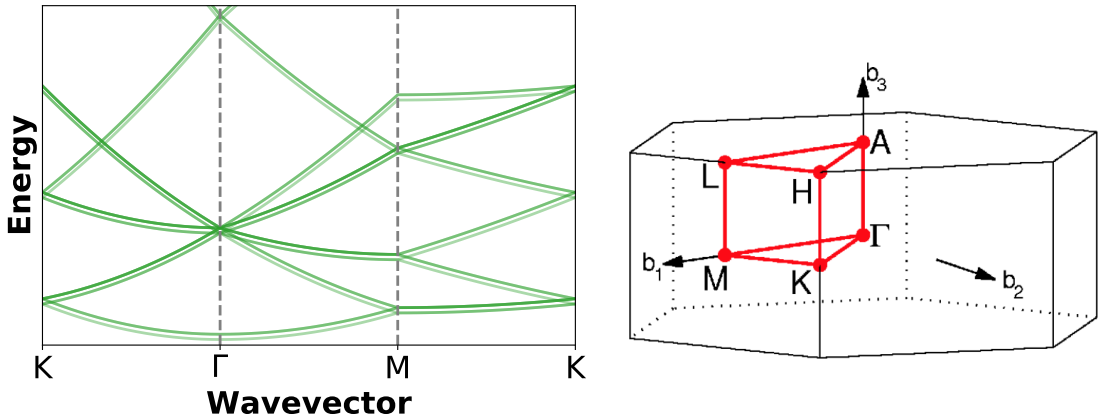

Figure 3.5: Brillouin zone with labeled high-symmetry points (right) and the empty-lattice band structure of a 2H-phase TMD (left). In three dimensions, the empty-lattice band structure gains significant complexity, exhibiting several of the same qualitative properties of the full electronic band structure.

3.4 Results: ab-initio calculations on pristine TMDs

In this section we report the results of our DFT electronic structure calculations of pristine MoS_2 and WS_2 and point defects therein. We first discuss the convergence of the calculated structural and electronic properties with respect to the Brillouin zone sampling and plane-wave energy cutoff, after which we compare the calculated properties of the pristine materials to literature. Next, we employ a supercell method to DFT in order to study the influence of point defects in these materials.

3.4.1 Convergence with respect to calculation parameters

In order to obtain accurate results from density functional theory calculations, the parameters of the calculation have to be chosen carefully. The most important parameters in determining the accuracy of a plane-wave DFT calculation are the energy cutoff value for the plane waves and the number of points used to sample the Brillouin zone [62]. In this section, we check the convergence of our DFT results with respect to these two parameters. As metrics, we track the changes in the calculated energy per atom and lattice parameters from a structural relaxation as the energy cutoff and number of k-points are increased. It is reasonable to track these metrics only during the relaxation step, as the relaxation is more sensitive to the calculation parameters than the subsequent static electronic structure calculation. Our criteria for convergence are that the changes in the energy per atom and the Mo-S bond length are smaller than 1 meV and 10^{-3} Å as the cutoff energy or k-mesh density are increased. These differences are smaller than chemically relevant energies, such that after reaching these criteria we may expect consistent results from our calculations, up to the accuracy of the PBE exchange-correlation functional we use.

Brillouin zone sampling Figure 3.6 shows the convergence of the energy per atom and the molybdenum-sulfur bond length as a function of the number of irreducible k-points used to sample the Brillouin zone. The amounts of irreducible k-points used were 6, 15, 32, 60, 96, 147, 216, 297, 400, 845 and 1536, corresponding to Gamma-centered Monkhorst-Pack grids commensurate to the Brillouin zone, consisting of NxNxN symmetry-reducible k-points with N = 3, 5, 7, 9, 11, 13, 15, 17, 19, 25 and 31. In order to visualize the convergence, we subtracted the values of the metrics from the calculations with grid size N from their values obtained in the calculation with grid size N-1. We note that our convergence criteria for both the energy per atom and the bond length is reached for a k-mesh of 7x7x7 k-points, corresponding to 32 points within the irreducible Brillouin zone. To be on the safe side, we will use a mesh of 11x11x11, or 96 irreducible k-points, for our electronic structure calculations.

Planewave cutoff energy In planewave DFT, the wavefunctions are built up from superpositions of planewaves. In order to keep the calculation manageable, this summation is limited to planewaves with an energy below a certain cutoff energy. Figure 3.7

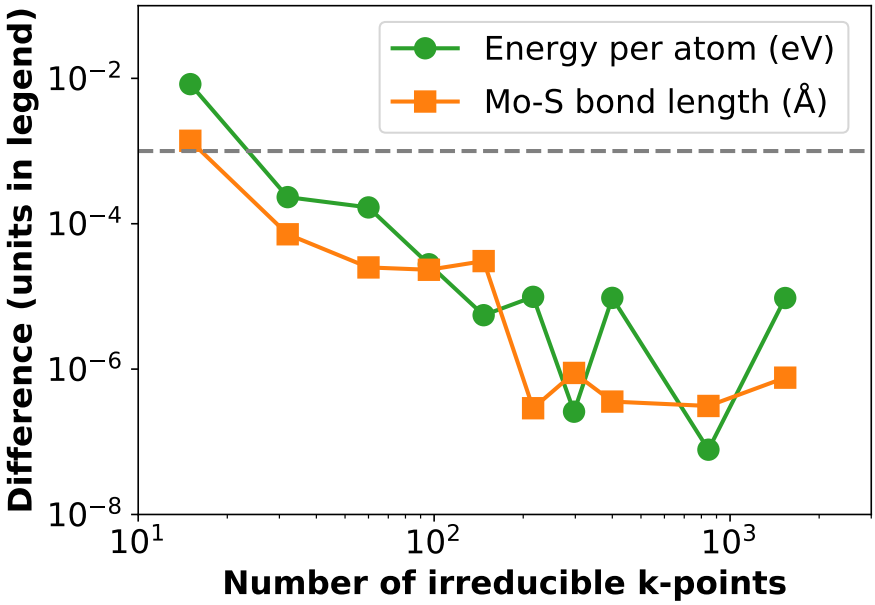

Figure 3.6: Convergence with respect to the Brillouin zone sampling of the energy per atom and Mo-S bond length in MoS_2 calculated with DFT.

shows the convergence of the energy per atom, Mo-S bond length and the electronic band gap as a function of the cutoff energy. The cutoff energy was increased from 200 eV to 400 eV in steps of 10 eV, and the values of the metrics calculated at cutoff energy E were subtracted from their values calculated at cutoff energy E - 10 eV to show their convergence. We note that our convergence criteria are satisfied at a cutoff energy of 320 eV. To be on the safe side, we will use a cutoff energy of 400 eV in our electronic structure calculations.

3.4.2 Structural properties from DFT

Using the optimized calculation parameters whose convergence was demonstrated in the last section, we performed DFT structural relaxations of bulk MoS_2 and WS_2. The resulting lattice parameters are compared to their experimentally measured values in table 3.2. It can be seen that all calculated lattice parameters agree with their experimental values to within half a percent. Evidently, both the strong in-plane interactions and the weak Van der Waals inter-layer interactions are modeled accurately in our calculations.

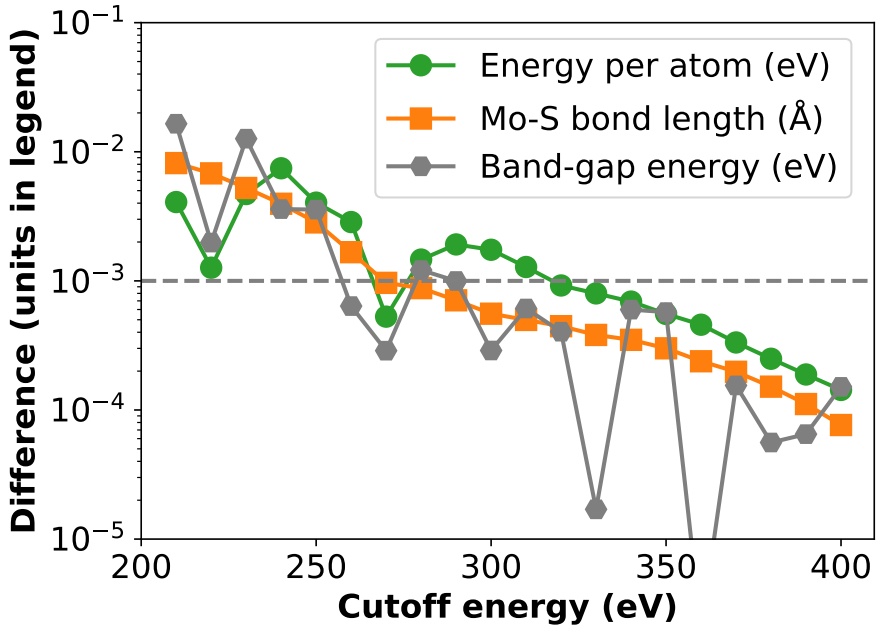

Figure 3.7: Convergence with respect to the planewave cutoff energy of the energy per atom, Mo-S bond length and bandgap energy in MoS_2 calculated with DFT.

Table 3.2: Comparison of the lattice parameters of MoS_2 and WS_2 obtained from our DFT structure relaxation to the experimentally measured values.

	Experimental [63]		Calculated	
TMD	**a (Å)**	**c (Å)**	**a (Å)**	**c (Å)**
MoS_2	3.16	12.29	3.161	12.32
WS_2	3.16	12.38	3.166	12.41

3.4.3 Vibrational properties from DFT

Now that we have obtained the relaxed structures of MoS_2 and WS_2, we will apply perturbations to them with the goal of deriving phonon frequencies from them. We note that there exists software to automate these types of calculations [64]. However, we have chosen for a manual approach which enables us apply the same technique to supercell calculations in our study of TMD alloys in chapter 4. We focus on the A_{1g} vibration as both its modeling and interpretation of results are relatively straight-forward: the vibration consists of the chalcogen atoms oscillating in the out-of-plane direction while the metal atoms are at rest (see figure 3.2), resulting in a purely out-of-plane oriented restoring force on the chalcogen atoms. Displacing the sulfur atoms of the relaxed MoS_2 and WS_2 cells in the out-of-plane direction and performing a static DFT calculation allows us to calculate this restoring force. In figure 3.8 we show the restoring force

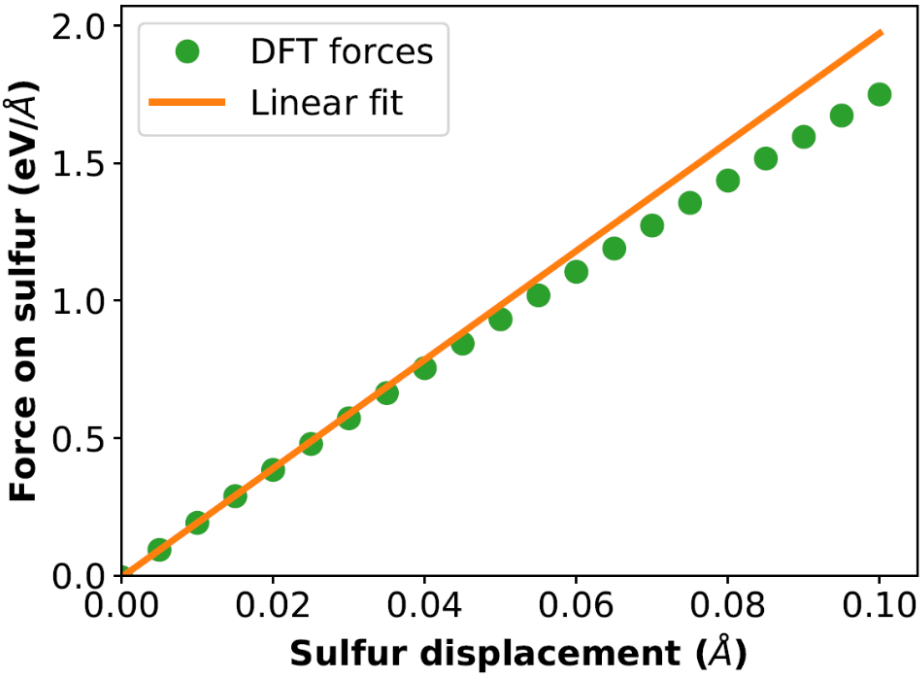

Figure 3.8: Restoring force on sulfur atoms in the A_{1g} vibration of MoS_2 as a function of their out-of-plane displacement. The slope of the linear fit is used to calculate the phonon frequency.

on the sulfur atom in the A_{1g} vibration of MoS_2 as a function of its displacement. The onset of anharmonicity can clearly be observed as the curve diverges away from a straight line for larger displacements. As a realistic vibrational amplitude, we enforce a sulfur displacement corresponding to a single vibrational quantum (phonon) occupying the A_{1g} mode. In the harmonic approximation and taking the phonon energy as $\hbar\omega$ where ω is the experimental radial frequency of the A_{1g} vibration, this amplitude is found to be 0.07 $\mathring{A}$. Using this displacement to calculate the A_{1g} frequency in MoS_2 gives a value of 394 cm$^-$1, which is within 4% of the experimental value of 410 cm$^-$1.

3.4.4 Electronic properties from DFT

Band structure Using the obtained relaxed structures of MoS_2 and WS_2, we proceed to calculate their electronic structure. In these calculations, the electronic energy bands are calculated along the path K - Γ - M - K in the Brillouin zone, sampling 20 points between each pair of high-symmetry points. Figure 3.9 shows the calculated band structure of MoS_2, with the upper valence band and the lower conduction band highlighted. Qualitatively, we note the indirect bandgap from the Γ-point in the valence band to the halfway point between Γ and K in the conduction band. Figure 3.10 shows the band structure around the bandgap for both MoS_2 and WS_2, such that their bandgaps can be seen more clearly. The calculated magnitudes of the bandgap

are compared to their experimental values in table 3.3. The band gap magnitudes for monolayers of MoS_2 and WS_2, where the bandgap transitions to a direct gap at the K point in the Brillouin zone, were also calculated and can be found in the same table. From the comparison in table 3.3 it can be seen that the bandgap is consistently underestimated by our DFT calculations, which is a known issue with DFT calculations using local exchange-correlation functionals [65]. More accurate values can be obtained from quasiparticle calculations based on, for example, Green's functions [66]. On the other hand, the comparison of the DFT bandgaps with the experimental data is also hindered by the significant exciton binding energies in these materials which shifts the measured photoluminescence energy away from the true electronic bandgap. Despite these complications, the difference between our calculated bandgaps of monolayers MoS_2 and WS_2 is in good agreement with the experimental values. In fact, the bandgap underestimation of DFT comprises a rigid shift of either the valence or the conduction band, such that the derived quantities like the effective mass are unaffected by the poor bandgap prediction [65].

Table 3.3: Comparison of the DFT-calculated bandgaps of MoS_2 and WS_2 to the experimentally measured values.

	Experimental bandgap		Calculated bandgap	
TMD	Bulk	Monolayer	Bulk	Monolayer
MoS_2	1.23 eV [67]	1.89 eV [68]	0.890 eV	1.74 eV
WS_2	1.35 eV [67]	2.01 eV [69]	1.025 eV	1.88 eV

In order to gain insight into the character of the valence band maxima and conduction band minima, the orbital decompositions of the wavefunctions at these points were calculated. This was done by means of the overlap integrals between the Bloch wavefunctions and the atomic orbital wavefunctions, the calculation of which is automated in the VASP software package. The orbital decompositions of the global extrema as well as the second local extrema of the valence and conduction bands are shown in figure 3.11. The valence band maximum at the Γ point is seen to consist mostly of contributions from the molybdenum d_z^2 and sulfur p_z orbitals. The character of the conduction band minimum is even more dominated by the molybdenum d_z^2 orbitals, showing negligible contributions from other orbitals. This analysis sheds light on the bandgap transition between bulk and monolayer TMDs, where the valence band states at th Γ point drop down in energy such that a direct bandgap emerges at the K point. Since both the VBM and the CBM consist largely of Mo d_z^2 character but only the energy of the VBM changes during the bandgap transition, this energy drop can be attributed to the S p_z contribution to the valence band maximum. From the viewpoint of crystal field theory such behavior would be expected since the stacking of monolayers would introduce an overlap between S p_z orbitals from different layers, increasing their energy. A similar conclusion was reached by Splendiani et al. [21].

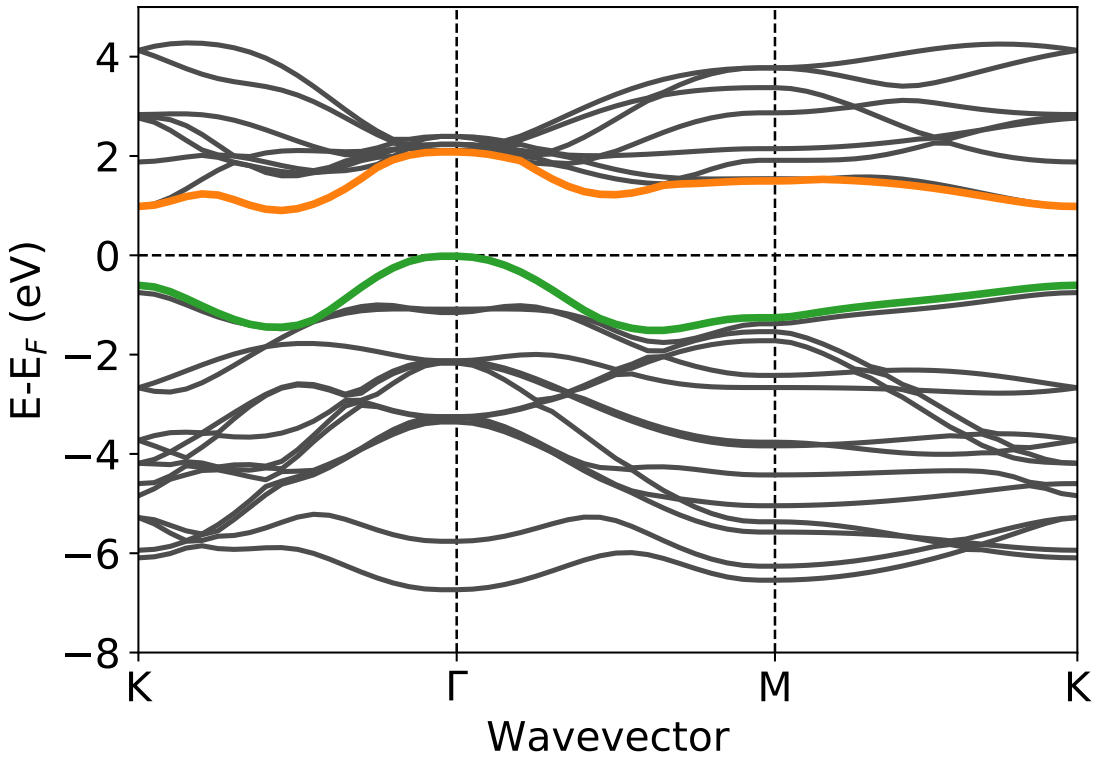

Figure 3.9: Electronic band structure of bulk MoS_2 calculated with DFT. The uppermost valence band and lowermost conduction bands are highlighted.

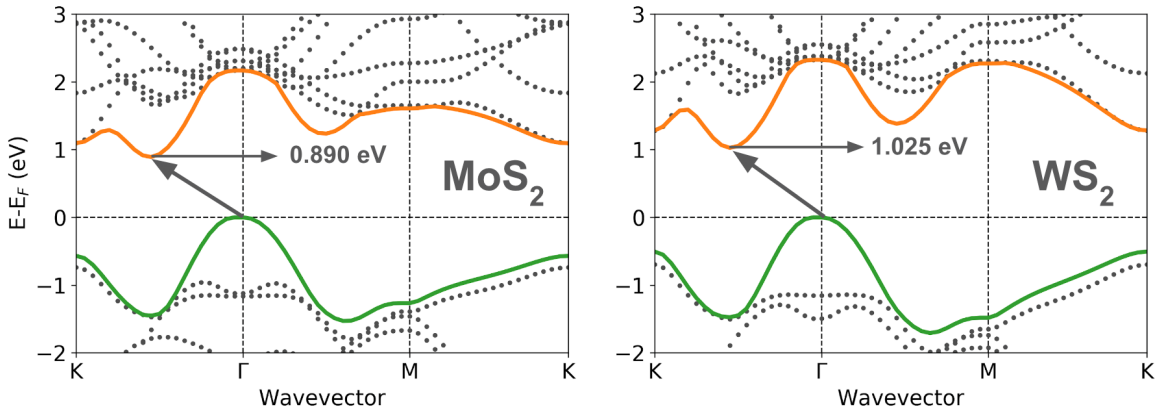

Figure 3.10: Band structure around the bandgap of both MoS_2 and WS_2 as calculated with DFT. The indirect bandgap transitions between the Γ point and the Γ-K middle point are indicated along with their energies.

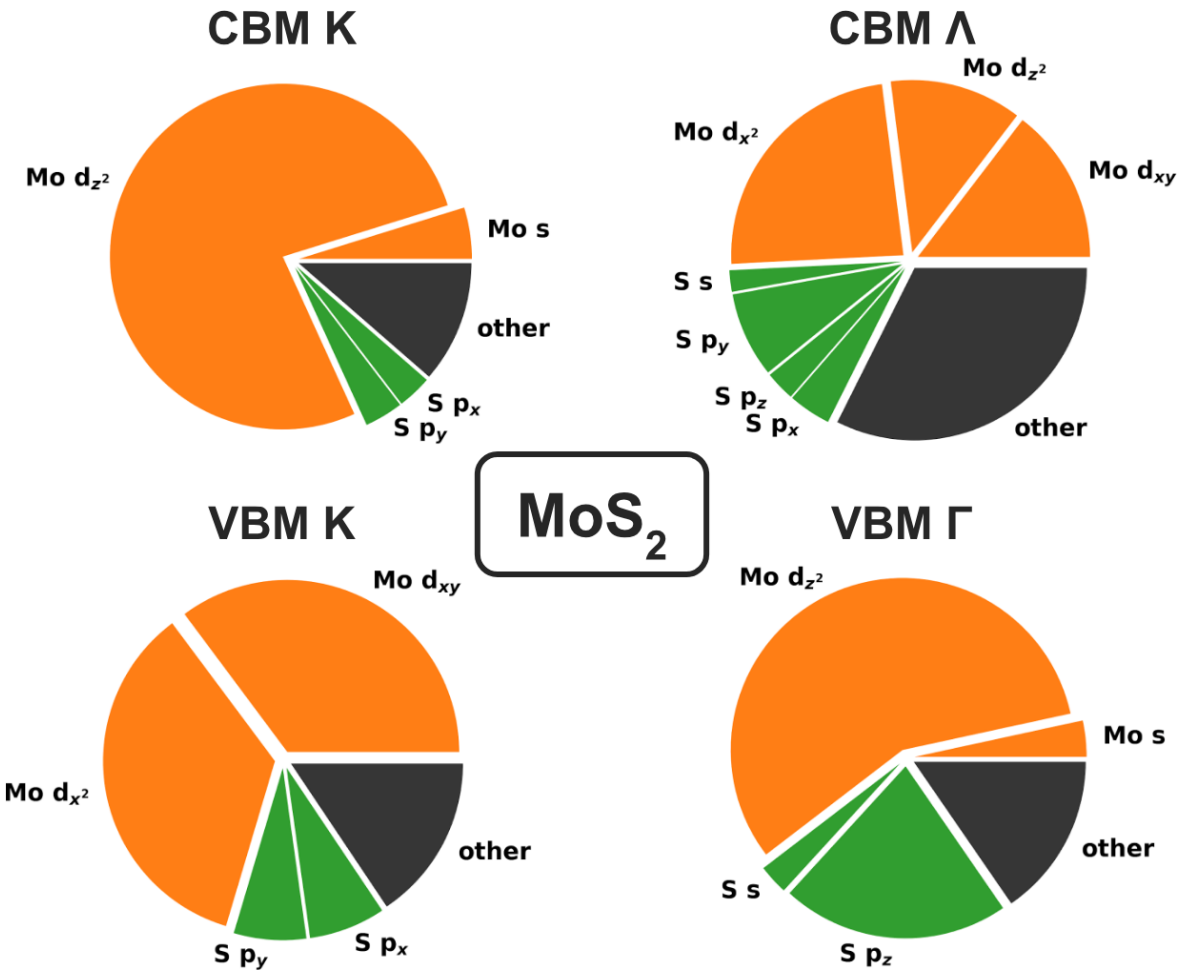

Figure 3.11: Orbital decompositions of the electronic wavefunctions at the valence band maxima at the K and Γ points and the conduction band minima at K and halfway the Λ line in bulk 2H-phase MoS_2 as calculated with DFT. The S p_z contribution of the valence band maximum at Γ causes this state to increase its energy upon stacking of monolayers, resulting in the direct-indirect bandgap transition.

Effective carrier mass As explained in chapter 2, the effective carrier masses can be derived from the band structure through the curvature of the valence band maximum for holes and the conduction band minimum for electrons:

$$m^* = \hbar^2 \left(\frac{\partial^2 E}{\partial k^2} \right)^{-1} \tag{3.1}$$

We do this by locally fitting a parabola to these bands of the form

$$E = a(k - k_0)^2 + c, \tag{3.2}$$

where k is the wavevector magnitude, and k_0 is the wavevector magnitude at the point where we want to find the curvature. The coefficient a is then the second derivative at the extremum which we use to calculate the effective carrier mass through equation (3.1). However, we found the results obtained using this method to be inconsistent with literature data. The fact that the calculated band diagrams are discontinuous at the high-symmetry points as well as the obfuscated representation of reciprocal space units in the VASP software make the parabola method difficult to use in practice. Instead, we used a related finite-difference method to calculate the effective masses. In this method, a new electronic structure calculation is performed for a selection of points in reciprocal space closely spaced around the valence band maximum / conduction band minimum. A finite-difference stencil is used to calculate the local curvature of the bands from the calculated electron energies at these points. For these calculations, the effective mass calculator of Fonari and Sutton was used [70]. Table 3.4 shows the effective carrier masses in the in-plane direction calculated in this way and compares them to values from DFT literature. The calculated values show excellent agreement with the literature values. One exception is the electron mass at the K point, for which we have found inconsistent results caused by the close proximity of the lowest conduction band to the next conduction band, such that errors occurred in the finite-difference calculations. From the wide spread in the literature values of this parameter, it appears that other authors also run into this problem. We note that in principle the issue may be alleviated by using the orbital decomposition of the bands in order to uniquely identify the lowest conduction band and calculate its curvature. However, since the conduction states at the K point are at an energy of 0.2 eV higher than the CBM at the Λ point which is a difference of about 7 $k_B T$ at room temperature and thus irrelevant for regular electron transport, we shall just focus on the electron mass at the absolute CBM at the Λ point instead.

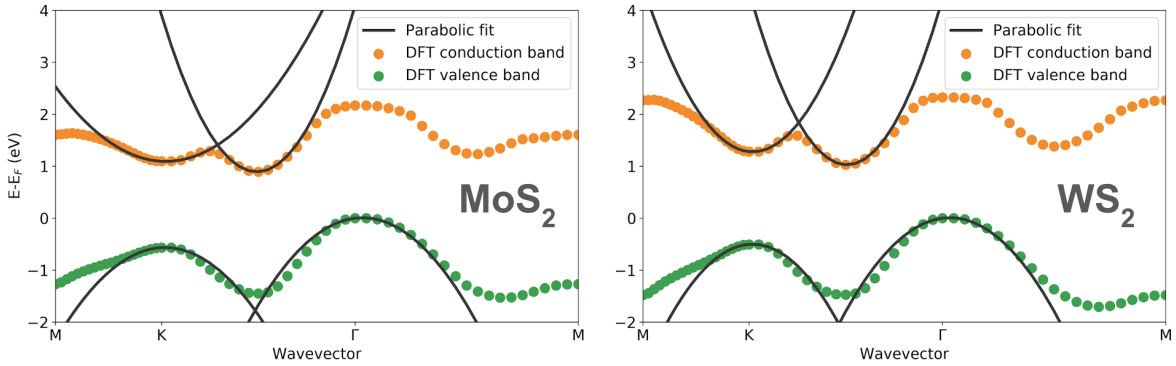

Figure 3.12: The DFT-calculated band structures of bulk MoS_2 and WS_2 shifted such that parabolas can be fitted to the K points as well as the Γ point and the conduction band minimum halfway between them. From the curvature of the fitted parabolas, the effective carrier masses can be extracted.

Table 3.4: Comparison of the calculated effective carrier masses in MoS_2 and WS_2 from DFT to values from literature.

	DFT literature				Calculated			
TMD	m_e^*K	$m_e^*\Lambda$	m_h^*K	$m_h^*\Gamma$	m_e^*K	$m_e^*\Lambda$	m_h^*K	$m_h^*\Gamma$
MoS_2	0.45 [71] 0.82 [72]	0.53 [71] 0.55 [72]	0.43 [71] 0.63 [72]	0.62 [71] 0.71 [72]	...	0.57	0.58	0.69
WS_2	0.38 [73]	0.57 [73]	0.37 [73]	0.83 [73]	0.36	0.61	0.43	0.65

3.5 Imperfections in synthesized TMDs

All crystals contain imperfections to some degree. Generally, the concentration of these imperfections depends on the synthesis method used to obtain the crystals. Slow, delicate synthesis methods such as the solvent flux method [74] can be used to synthesize very pure single crystals on timescales of several weeks. For large-scale industrial use of crystals, however, this is not practical. Hence, vapor-phase methods such as chemical vapor deposition (CVD) or atomic layer deposition are used, which permit much higher growth rates. However, these synthesis methods also produce higher concentrations of defects in the deposited crystals. One example is the emergence of nano-sized crystal grains or domains which have different orientations and are separated by grain boundaries. These domains emerge when multiple nucleation sites are formed at the beginning of the deposition and differently-oriented crystals start growing on these sites. While each domain is itself crystalline, the grain boundaries may have a significant impact on the macroscopic electrical and chemical properties of the polycrystalline material. Other types of imperfections include missing, misplaced or swapped atoms within the crystal lattice. Since these defects are localized to a single point in the crystal, they are known as point defects. Missing atoms or vacancies may arise for

example with the use of plasma during deposition, where atoms may be ejected from the surface, or when the deposited crystal is understochiometric. Substitutional atoms may originate from impurities which are intentionally or unintentionally introduced into the deposition process. For example, in the case of doping, the substitutional defects are deliberately introduced in order to enhance the electronic properties of the crystal. For transition metal dichalcogenides in particular, it is known that defects are important in determining their chemical and electronic properties [22, 23, 24, 25]. While grain boundaries are relevant in determining electronic properties, these types of defects are difficult to simulate with ab-initio methods since they require large simulation domains. Therefore, we focus on studying the effect of point defects on the structural and electronic properties of TMDs by density functional theory calculations in the next section.

3.6 Results: ab-initio calculations on point defects in TMDs

In order to gain insight into the impact of point defects on the structural and electronic properties of TMDs, we study a selection of 6 point defects in MoS_2 crystals in this section: vacancies of S, S_2, MoS_3 and MoS_6 as well as Mo-W and S-O substitutions. The choice of the vacancy defects was based on experimental observations of these defects in plasma-exposed MoS_2 layers [75]. Additionally, quantum chemistry calculations of the formation energies of various point defects indicate that the single sulfur vacancy is the most common type of point defect in MoS_2 [76, 77]. The Mo-W substitutional defect was included as a stepping stone towards the treatment of $Mo_xW_{1-x}S_2$ alloys in the next chapter. The S-O substitutional defect was included since these defects are expected to occur when the MoS_2 films are exposed to air. Interstitial S atoms are also classified as point defects and are known to have relatively low formation energies [76], but these defects were not included in our study.

Point defects are the simplest defects to model since they are intrinsically localized in the crystal structure. Nevertheless, the simulation of realistic concentrations of point defects requires significant changes to the computational methodology compared to pristine crystal calculations, as we will explain next.

3.6.1 Computational approach

In synthesized 2D-TMDs, typical point defect concentrations are on the order of 0.01 to 0.1 per crystallographic unit cell [78]. Evidently, a calculation based on the periodic repetition of the primitive unit cell cannot accurately model these defect concentrations: the closest options are 0 or 1 defects per primitive cell. As such, we need to switch to a supercell-based calculation. In these calculations, we choose a supercell consisting of multiple primitive unit cells as our periodically repeated unit cell. For example, a single point defect introduced into a supercell consisting of 5x5x2 unit cells would

represent a defect concentration of 0.02 defects per primitive cell, which is comparable to experimentally observed defect concentrations.

A complication that arises in the use of supercells in planewave DFT calculations is that the resulting band structure does no longer correspond to the primitive unit cell. As the supercell is larger than the primitive cell, its Brillouin zone becomes smaller. This small Brillouin zone becomes overcrowded with energy bands, resulting in an obfuscated band diagram. In order to still interpret the results and compare them to pristine materials, a so-called "unfolding" of the supercell band structure may be performed to obtain an effective primitive-cell band structure. We use the software vasp_unfold [79] to automate this procedure.

The calculation of effective carrier masses also requires some additional thought when switching to a supercell-based calculation method. For the primitive-cell calculations, we were able to find the valence and conduction bands and fit parabolas to them. For a supercell calculation this is unfeasible as the valence and conduction bands are continuously crossed by other electronic bands in the supercell Brillouin zone, and it is a priori unclear which band corresponds to the actual primitive-cell valence or conduction band. As a workaround, we first calculate the energies of the 40 bands closest to the bandgap in a small region around the valence band maxima and conduction band minima. Next, we identify which of these energy values belong to the effective valence and conduction band by comparing the orbital decomposition of the wavefunctions to those of the valence band maxima and conduction band minima of the primitive cell calculation. Having thus reconstructed the valence and conduction bands around these points, we may calculate the effective carrier mass by the usual parabolic fitting method or finite-difference calculation of the band curvature.

3.6.2 Effects on crystal structure

Relaxation of the point defects was performed with DFT. For these calculations the Brillouin zone sampling in the k_x-k_y plane was reduced to 3 by 3 k-points. This is justified on the grounds that the Brillouin zone of the 5x5 supercell is a factor 5 smaller than for a primitive cell calculation. Figure 3.14 shows heatmaps of the structural relaxation, highlighting the structural changes caused by the point defects in MoS_2. The substitutional Mo-W and S-O defects are seen to cause the least distortion, with especially the tungsten substitution causing virtually no structural deformation of the MoS_2. The single sulfur vacancy produces distortions of a similar magnitude as the S-O substitution, and the larger vacancy structures cause significantly larger distortions to the crystal lattice. From these images, it can be seen that the structural distortions are highly localized around the defect centers. Additionally, a comparison of the scale bar to our previous calculation of typical phonon displacements reveals that only the largest vacancy defect, a missing MoS_6 unit, produces distortions larger than the typical phonon amplitude of 0.07 $\mathring{A}$. For all the other studied point defects, the maximum atomic displacement stays below half of this value. This indicates that the structural rearrangements around point defect sites are negligible compared to phonon-induced

distortions. Of course, the defects themselves may still have significant influence on the electronic structure, which is investigated in the next section.

3.6.3 Effects on electronic structure

Band structure Using the relaxed structures of the 5x5 supercells of MoS_2 with point defects, band structure calculations were performed. Since the Brillouin zone corresponding to the supercell is smaller than the one corresponding to the primitive cell, the energy bands need to be "unfolded" in order to obtain an effective band structure for the Brillouin zone of the primitive cell. This unfolding was automated using the software vasp_unfold [79]. The resulting effective band structures around the bandgap for the point defects are shown in figure 3.15. The substitutional defects have band structures which are very similar to the band structure of the pristine material, with barely any spectral noise visible. For the S and S_2 vacancies, we observe higher levels of spectral noise, accompanied by the emergence of new, dispersionless states within the bandgap. In the case of the MoS_3 vacancy, these gap states are even more abundant and are seen to originate from the unpaired S atoms, since they are not visible in the band structure of the MoS_6 vacancy. Additionally, the band structures of the MoS_3 and MoS_6 vacancies show significant levels of spectral noise, which is indicative of the breaking of the translational symmetry in the crystal on the primitive-cell level.

Effective carrier mass In order to obtain effective carrier masses from these unfolded band structures, identification of the valence and conduction bands is needed. This is non-trivial because these bands are crossed many times by bands (both spectral noise and defect states) which do not belong to the primitive cell band structure. This makes it hard to identify the same band at several points in k-space, which is necessary in order to calculate its curvature for use in the calculation of the effective carrier mass. The identification of the bands corresponding to the primitive-cell valence and conduction band was performed by comparing their orbital decompositions to those found for the primitive cell calculations on MoS_2 (see figure 3.11). The automated finite difference script by Fonari and Sutton [70] was used to calculate the lateral effective carrier masses of the defect structures, which are tabulated in table 3.5. We note that the effective carrier masses calculated from simulations with realistic concentrations of point defects do not differ by more than a factor of 2 from their values in defect-free MoS_2. As such, we do not expect these defects to be limiting the carrier mobility in synthesized 2H-phase TMDs through their impact on the effective mass. Other effects, most notably the presence of grain boundaries and, to a lesser degree, electron-phonon scattering are more likely to be limiting the carrier mobility in these materials. Additionally, changes in carrier concentration effectuated by point defects may play a role in determining the mobility. For example, both sulfur vacancies[77] and lead impurities [**?**] are known to act as p-type doping in MoS_2.

Table 3.5: Electronic and structural properties of MoS_2 with various point defects in a concentration of 0.04 per unit cell.

Structure	m_e^*	m_h^*	a	c/a
Pristine	0.57	0.69	3.162	3.941
S vac.	0.65	0.75	3.155	3.950
S_2 vac.	0.67	0.81	3.149	3.955
MoS_3 vac.	0.78	0.85	3.159	3.933
MoS_6 vac.	0.85	1.38	3.140	3.950
Mo-W sub.	0.59	0.77	3.161	3.944
S-O sub.	0.60	0.77	3.157	3.950

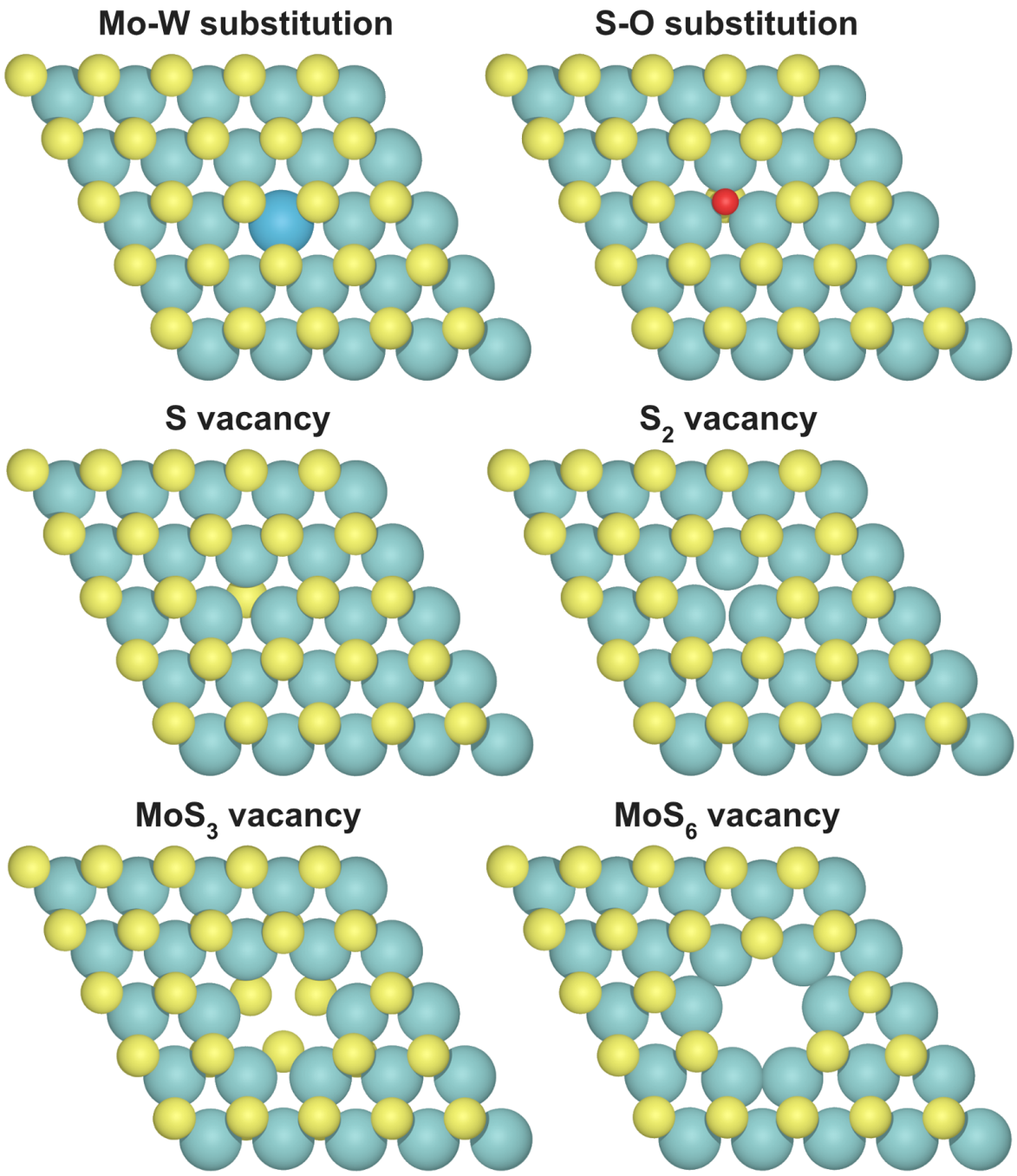

Figure 3.13: Overview of the supercell structures used to study point defects in MoS_2.

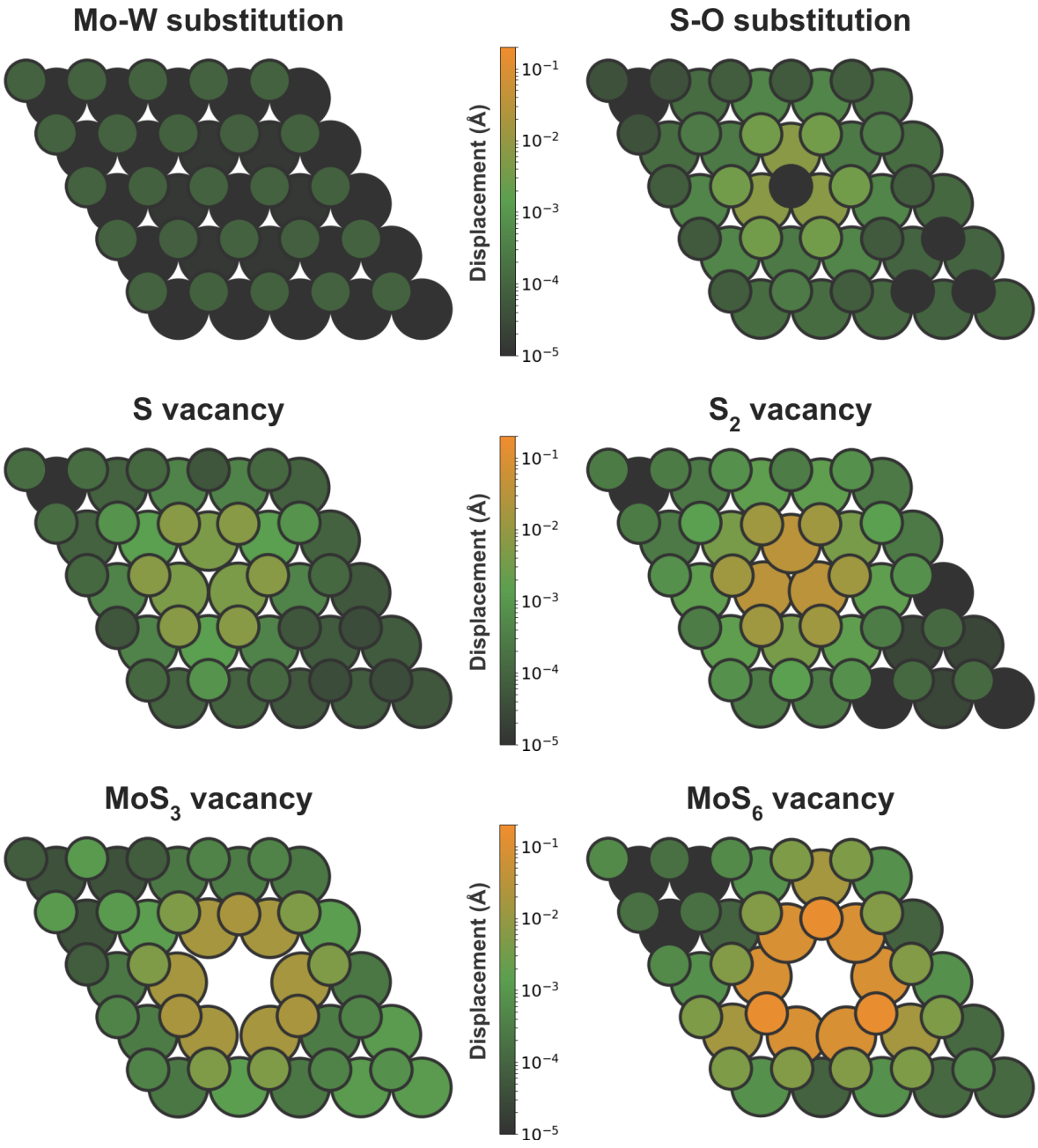

Figure 3.14: Relaxation heatmaps of the studied point defects in MoS_2. The colors indicate atomic displacements with respect to their position in the pristine material.

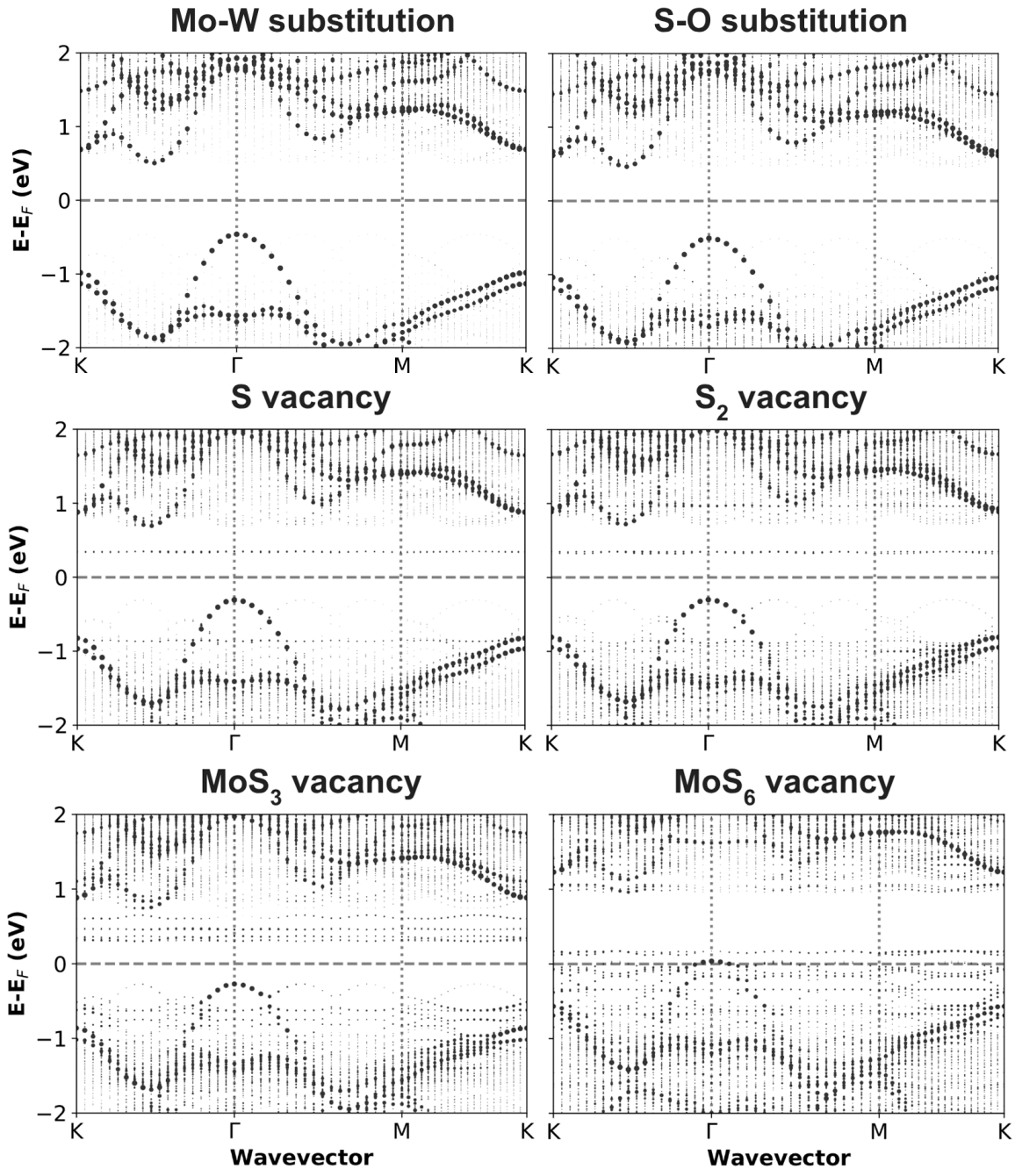

Figure 3.15: Effective band structures around the bandgap for concentrations of 0.04 per unitcell of six common point defects in MoS_2

Chapter 4

Two-dimensional Alloys: Case Study of $Mo_xW_{1-x}S_2$

Abstract

A requirement for the usability of 2D transition metal dichalcogenides (TMDs) for a wide range of applications like nano-scale transistors and sensors is the tunability of their material properties. Numerous pathways to achieving tunability have already been explored, such as inducing doping or crystal defects in the material or combining multiple TMDs into alloys. The method of alloying is especially promising as several pairs of TMDs exist with nearly identical crystal structures, such that their alloys have minimal structural distortion. Accordingly, these alloys may achieve a large degree of tunability by controlling their composition without significantly deteriorating the desirable intrinsic material properties of the TMDs. Previous work on these types of alloys has shown that relevant properties like the band gap can indeed be tuned by controlling the alloy ratio. However, not much is known about the effect that the atomic-scale ordering of the alloy has on its material properties. Many crystal growth techniques are unable to achieve the atomic-level growth control necessary to systematically study the effects of atomic ordering. As such, the focus of most TMD alloy studies has been on the effect that the alloy ratio has on the material's properties, and the effects of atomic ordering are largely unknown.

In this work, we investigate the influence of both the alloy ratio and the atomic-scale ordering of $Mo_xW_{1-x}S_2$ on the material properties of these alloys. We employ the synthesis technique of atomic layer deposition (ALD) to achieve the required atomic-level growth control. We show that alloys of molybdenum disulfide and tungsten disulfide $Mo_xW_{1-x}S_2$ are influenced by the atomic mixing in a distinct way, as we observe a systematic variation in the spectral position of the dominant A_{1g} and E_{2g} vibrations in the Raman response when altering the ALD cycle ordering. This effect is distinct from alloy ratio-dependent effects and is furthermore unexpected from a classical analysis of the vibrational frequencies. An ab-initio analysis of the vibrational frequencies of

the alloys suggests that this effect is related to the atomic-scale ordering and clustering of the molybdenum and tungsten atoms in the alloy. Additionally, experiments where the alloy composition was varied from pure WS_2 through the $Mo_xW_{1-x}S_2$ alloys to pure MoS_2 allowed us to demonstrate the tunability of the electrical resistivity and the control over the band gap offered by ALD. Through ab-initio modeling of the alloys we elucidate the underlying origin of these trends. Comparing the experimental and ab-initio results suggests that grain size is the dominant effect dominating the resistivity for ALD-synthesized alloys, whereas the band gap is mainly determined by the alloy fraction.

4.1 Introduction

Due to their graphene-like layered structure, the family of two-dimensional transition metal dichalcogenides (2D TMDs) exhibit fascinating and useful electro-optical properties, making them promising materials for integration in novel transistors and sensors. For the application of TMDs to these devices, the ability to control their material properties is highly desirable. Various pathways exist to this kind of control in TMDs. Doping, defects, morphological differences and alloying can all serve to this goal. In this work we focus on alloying of MoS_2 and WS_2. Since these materials are structurally closely related, the $Mo_xW_{1-x}S_2$ alloys may achieve properties intermediate between the constituent materials without significantly degrading the quality of the crystal. In section 4.2.1, we introduce a direct atomic layer deposition (ALD) method of synthesizing the $Mo_xW_{1-x}S_2$ alloys. In section 4.2.2 we investigate the growth and composition of the films deposited with our ALD recipe. In section 4.3.2 we study the control over the electronic properties of the deposited films that can be achieved by controlling the alloy ratio, while in section 4.3.3 we study the effects of the atomic-scale mixing of the alloy on its electronic properties.

4.2 Methods

This section contains a description of our methods of synthesizing the $Mo_xW_{1-x}S_2$ alloys and the experimental characterization thereof, as well as a discussion of the computational details of our theoretical investigation of these materials.

4.2.1 Atomic Layer Deposition of $Mo_xW_{1-x}S_2$ alloys

For the synthesis of the $Mo_xW_{1-x}S_2$ alloys we use the plasma-enhanced atomic layer deposition (PE-ALD) technique. The ALD technique is capable of producing highly uniform films with sub-nanometer thickness control by employing self-limiting surface reactions between a substrate and vapor-phase precursors. We performed the depositions in an Oxford Instruments FlexAL2D reactor equipped with an inductively coupled plasma (ICP) source which allows for substrate-independent control over the plasma.

For the deposition of the $Mo_xW_{1-x}S_2$ alloys, a supercycle approach was used where each supercycle consists of five ALD cycles of either MoS_2 or WS_2, as illustrated in figure 4.1. Each of those five ALD cycles consists of two half-cycles with argon purge steps in between. In each first half-cycle, the metal-organic precursor $(({}^t\text{BuN})_2(\text{Me}_2\text{N})_2\text{Mo}$ (98%, Strem Chemicals) for molybdenum or $({}^t\text{BuN})_2(\text{Me}_2\text{N})_2\text{W}$ (99%, Sigma Aldrich) for tungsten) is bubbled into the reactor chamber. These two precursors have the same structure apart from their central metal atom (molybdenum or tungsten), and their structure is illustrated in figure 4.2. After the precusor has adsorbed onto the surface in a self-limiting manner, the reactor chamber is purged with an argon flow. In the second half-cycle, the inductively-coupled plasma source is ignited with a gas mixture of hydrogen disulfide and argon. The plasma species serve to remove remaining organic precursor ligands and deposit sulfur onto the surface, thus preparing the surface for the next ALD cycle. Each supercycle consists of five such ALD cycles, allowing control over the composition of the $Mo_xW_{1-x}S_2$ alloy by varying the relative amount of molybdenum and tungsten cycles in each supercycle. Depositions were performed on silicon (100) wafers with 450 nm thermally grown silicon oxide. The experimental parameters of the deposition process are summarized in table 4.1.

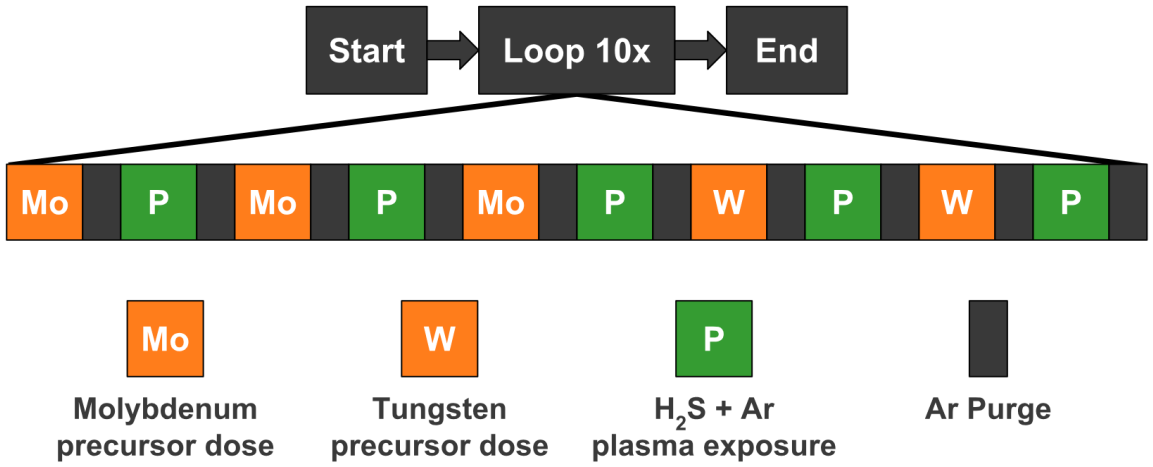

Figure 4.1: The supercycle approach used to deposit the $Mo_xW_{1-x}S_2$ alloys. With a supercycle consisting of five molybdenum and/or tungsten cycles, the alloy fraction can be varied between zero and one in steps of 0.2. After every half-cycle, a purge step (not illustrated) ensures there is no direct contact between the precursor and co-reactant.

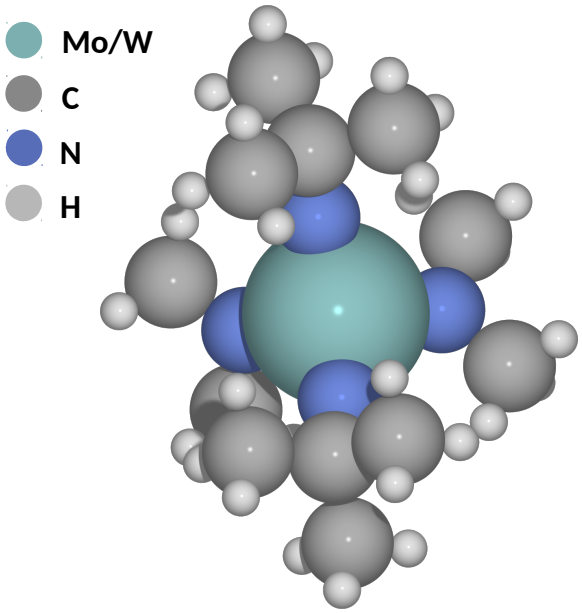

Figure 4.2: Structure of the molybdenum and tungsten precursors $(^tBuN)_2(Me_2N)_2(Mo/W)$ employed for atomic layer deposition of the $Mo_xW_{1-x}S_2$ alloys in this work.

Table 4.1: Summary of the deposition parameters of the $Mo_xW_{1-x}S_2$ alloy supercycle ALD process

Process parameter	**Value**	**Process parameter**	**Value**
Heater temperature	450 °C	Purge duration	10 s
Substrate temperature	350 °C	Purge argon flow	200 sccm
Reactor wall temperature	120 °C	Plasma duration	30 s
Precursor dose duration	10 s	Plasma power	500 W
Bubbler argon flow	50 sccm	Plasma pressure	15 mTorr
Chamber pressure during precursor dose	30 mTorr	Plasma mixture	40 sccm Ar 10 sccm H_2S

4.2.2 Characterization of synthesized alloys

The growth of the alloys was monitored during deposition by in-situ spectroscopic ellipsometry (SE) (J.A. Woollam M2000F, 1.25 eV - 5 eV). The film thickness was extracted by parametrizing the dielectric function with a series of B-splines, in which the Kramers-Kronig relations linking the real and imaginary parts of the dielectric function, were conserved. Resistivity measurements on the deposited films were performed using the four-point probe method (Signatone S-301-6). Raman spectroscopy

and photoluminescence (PL) spectroscopy were performed using a Renishaw Raman microscope equipped with a 514.5 nm laser. X-ray photoelectron spectroscopy measurements were performed using a Thermo Scientific K-Alpha KA 1066 X-ray photon spectroscope employing 1486.6 eV aluminum K-alpha radiation. The measurement depth is determined by the escape depth of the electrons which is limited by inelastic scattering, and is in the order of 10 nanometers for the materials in this study.

4.2.3 Density functional theory calculations

For the ab-initio study of the electronic structure of the $Mo_xW_{1-x}S_2$ alloys, density functional theory was employed in the projector-augmented wave framework [56, 80] as implemented in the VASP software package [81, 82, 83, 84]. The exchange-correlation functionals from Perdew, Burke and Ernzerhof (PBE) [42] were used, and inter-layer dispersion forces were accounted for by the zero-damping DFT-D3 method of Grimme [48]. In order to realistically model different alloy ratios, supercells were used of 5x5x1 primitive cells. Different alloy fractions were simulated by changing the relative amount of molybdenum and tungsten atoms constituting the total of 50 metal atoms in the supercell. Per alloy fraction, five different random configurations were generated (as exemplified in figure 4.3). These structures were relaxed until the total energy differential was smaller than 10^{-4} eV (for band structure calculations) or until all forces were smaller than 10^{-3} eV/Å(for phonon calculations). Structural relaxations were performed with a converged cutoff energy of 400 eV and by sampling the Brillouin zone with a Γ-centered Monkhorst-Pack grid [54] of 3x3x1 points. For electronic band structure calculations, 20 points along each high-symmetry line were sampled. The usage of a supercell impedes the direct interpretation of the obtained band structures as in a primitive cell calculation. This was mitigated by a so-called "unfolding" scheme [79] that recovers an effective band structure from the supercell calculation. The parabolic fitting method was used to obtain effective carrier masses from the obtained band structures.

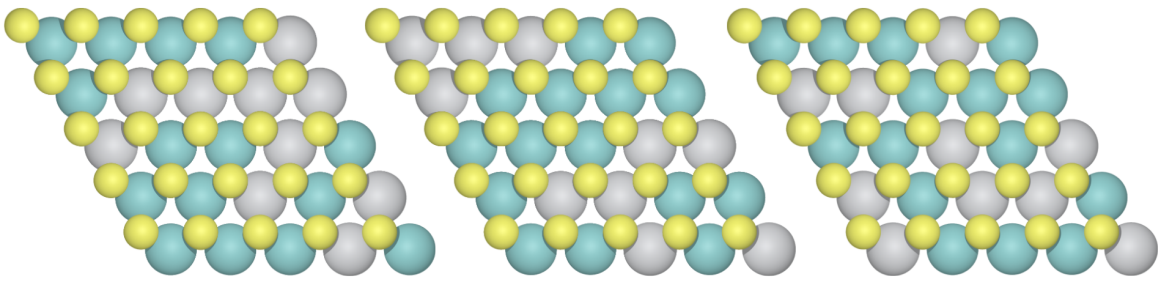

Figure 4.3: Three examples of supercells representing the same alloy ratio of 6:4 with different random configurations. In our calculations of alloy ratio-dependent effective masses, five random configurations were calculated for every alloy fraction such that the calculated effective carrier masses could be averaged over the configurations.

4.3 Results and discussion

In this section, we first study the deposition process and the crystallinity of the resulting show results of in-situ thickness monitoring by spectroscopic ellipsometry, composition measurements by x-ray photoemission spectroscopy and on the ALD-deposited $Mo_xW_{1-x}S_2$ alloys in order to get insight into the deposition process. Next, we study the effects of the alloy composition on their resistivity, effective mass, photoluminescence and Raman scattering. This analysis is split into two complementary parts: effects of the alloy ratio are treated in section 4.3.2 and effects of the alloy mixing are treated in section 4.3.3.

4.3.1 Film growth and composition

A series of samples was deposited using ALD supercycles with Mo:W cycle ratios of 5:0 (pure MoS_2), 4:1, 3:2, 2:3, 1:4 and 0:5 (pure WS_2). For each sample, a total of 50 ALD cycles (= 10 supercycles) were performed.

Thickness The apparent thickness of the films after deposition was determined by in-situ spectroscopic ellipsometry. From this data, the growth per supercycle (GPsC) of the alloys was calculated, as shown in figure 4.4. The GPsC is seen to decrease linearly as the relative number of tungsten cycles in the supercycle increases, with the GPsC of the pure MoS_2 deposition being 60% higher than that of pure WS_2. The growth per cycle (GPC) of the pure MoS_2 and WS_2 depostions are 1.28 Å and 0.83 Å respectively. These values are comparable to the values of 1.4 Å and 0.65 Å which were observed in the MoS_2 [85] and WS_2 (unpublished) processes on which our process is based.

Composition The alloy ratio of the ALD-deposited $Mo_xW_{1-x}S_2$ films was studied by x-ray photoelectron spectroscopy (XPS). XPS is a method of studying the atomic composition of a sample by irradiating it with x-ray radiation and recording the energy spectrum of the valence and core electrons that are expelled from the sample. XPS does not yield absolute atomic concentrations (in absence of a reference sample), but is able to give accurate abundance ratios of different types of atoms within the sample. The molybdenum to tungsten abundance ratio in the ALD-deposited $Mo_xW1\text{-}xS_2$ alloys was extracted from XPS spectra, and are plotted as a function of the Mo:W cycle ratio in figure 4.5. The data coincides with a curve of the form $y = \frac{cR}{cR+(1-R)}$, where R is the Mo:W cycle ratio and c is the ratio in growth rate (atoms per cycle) between molybdenum and tungsten. The best fit to the data was obtained with $c = 1.5$. This is the same factor that was found in the SE thickness monitoring, indicating that the thickness difference between Mo-rich films and W-rich films seen from ellipsometry measurements (figure 4.4) can be fully explained by a difference in the amount of metal atoms deposited during the Mo and W half-cycles. This excludes any differences of morphology or density among the series of alloys deposited with different Mo:W cycle

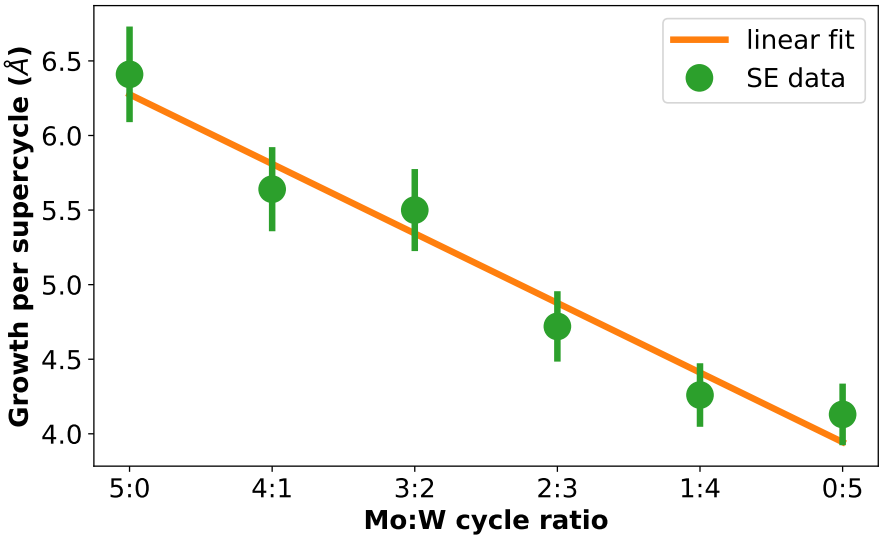

Figure 4.4: Growth per supercycle (GPsC) of ALD-deposited $Mo_xW_{1-x}S_2$ alloys as a function of the Mo:W cycle ratio in the five-step supercycle. Data was obtained from in-situ spectroscopic ellipsometry measurements.

ratios. The reason for the difference in amount of metal atoms deposited in the Mo and W cycles may be attributable to the difference in size of the molybdenum and tungsten precursors. The tungsten precursor may block more reactive sites on the surface than the molybdenum precursor due to its larger size, leading to a smaller number of deposited atoms when saturation is reached.

Lattice vibrations The vibrational modes of the deposited films were studied by Raman spectroscopy, which is a quick, non-intrusive and substrate-independent characterization method. In this method, the samples are irradiated with laser light, some of which is absorbed by lattice vibrations (phonons) in the sample, producing peaks in the back-scattered light spectrum which are shifted away from the laser frequency. These peaks carry information about the normal vibrations of the sample, and thus about the crystal structure. The Raman spectra of the ALD-deposited samples with Mo:W cycle ratios of 5:0, 4:1, 3:2, 2:3, 1:4 and 0:5 are shown in figure 4.6. In the spectrum of the pure MoS_2 sample, the E_{2g} and A_{1g} peaks can be seen at frequencies 384 cm^{-1} and 410 cm^{-1} respectively. In the spectrum of the pure WS_2, the same peaks are seen at 356 cm^{-1} and 420 cm^{-1}. Here it should be pointed out that the E_{2g} peak of WS_2 coincides with the second harmonic of the defect-enabled $LA(M)$ mode, which is difficult to deconvolute from the E_{2g} peak. The differences in E_{2g} and A_{1g} frequency between MoS_2 and WS_2 can be understood by considering the motion of these vibrations. In the E_{2g} vibration, the metal and sulfur atoms both oscillate in the in-plane direction. The heavier tungsten atoms have more inertia than the molybdenum

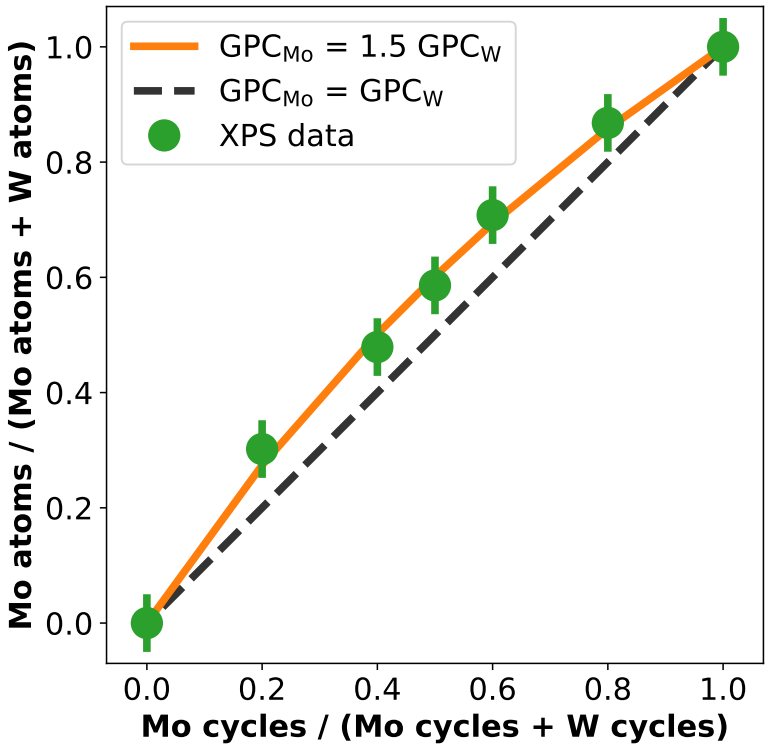

Figure 4.5: Relative abundance of molybdenum and tungsten atoms in the ALD-deposited alloys. The diagonal line shows the expected behavior when growth rates (atoms per cycle) of the molybdenum and tungsten would be equal. The curve through the data is of the form $f = \frac{cR}{cR+(1-R)}$ where R is the Mo:W cycle ratio and c is the ratio in growth rate (atoms per cycle) between molybdenum and tungsten. The best fit to the data was obtained with $c = 1.5$.

atoms, resulting in an E_{2g} frequency which is 28 cm^{-1} lower in WS_2 than in MoS_2. On the other hand, the A_{1g} vibration consists of out-of-plane movement of the sulfur atoms while the metal atoms remain stationary. While in this case the oscillating mass is equal for both MoS_2 and WS_2, there is a difference in metal-sulfur bond strength between these materials, causing a frequency difference of the A_{1g} vibration of 10 cm^{-1} between them. The spectra of the intermediate $Mo_xW_{1-x}S_2$ alloys display a superposition of both the MoS_2-related E_{2g} and A_{1g} peaks as well as the WS_2-related E_{2g}+$2LA(M)$ and A_{1g} peaks. The relative intensity of the MoS_2-related and WS_2-related peaks in these spectra is seen to correspond to the Mo:W ALD cycle ratio used in the deposition of the samples. The overall intensity of the spectra is highest for the pure MoS_2 and WS_2 samples. For WS_2, this is partially due to the choice of laser frequency, as the 514 nm light is resonant with the B-exciton of this material. The reduced Raman intensity from the intermediate alloys may indicate a reduced crystallinity of these films compared to

the pure MoS_2 and WS_2 films.

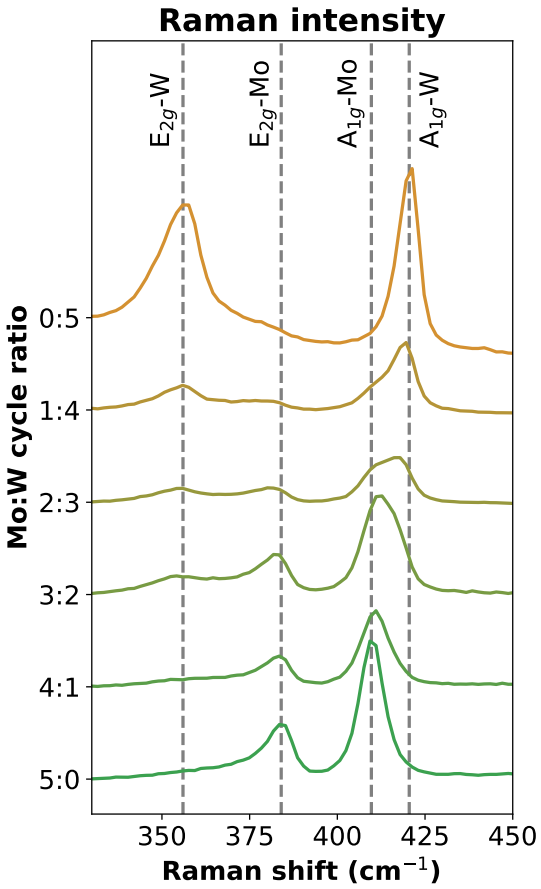

Figure 4.6: Normalized Raman spectra of the $Mo_xW_{1-x}S_2$ alloys grown by ALD with Mo:W cycle ratios of 5:0, 4:1, 3:2, 2:3, 1:4 and 0:5. The peaks corresponding to the E_{2g} and A_{1g} vibrations of MoS_2 and WS_2 can be identified in the pure MoS_2 and WS_2 spectra as well as in the spectra of the alloys.

Morphology Transmission electron microscopy images were made of the pure MoS_2 and WS_2 samples as well as the alloy with Mo:W cycle ratio of 2:3 (atomic ratio 50/50) in order to study their morphology. Figure 4.7 shows images of these samples at made at magnifications of 50.000x and 250.000x. On all three samples, fringes can be seen whose frequency corresponds to the interlayer spacing of crystallites which are oriented in the out-of-plane direction. The emergence of these fin-like structures is known to be a common occurence in the PE-ALD synthesis of MoS_2 and WS_2 and is due to the fact that the precursor adsorbs preferentially on the edges of the crystal grains and not on the basal planes. No significant difference in the concentration of out-of-plane structures was observed between the pure MoS_2/WS_2 samples and the alloy. In order

to investigate the crystallinity of the deposited TMD alloy, a Fourier transform of the TEM images was made such that the crystal lattice spacings could be measured conveniently. Figure 4.8 shows a typical Fourier transform of a TEM image from the $Mo_xW_{1-x}S_2$sample with $x = 0.5$. Three features can be identified: two concentric rings and a series of dots spaced around the center. The two concentric rings represent two spatial frequencies which can be deduced to originate from the in-plane spacing of the hexagonal crystal, see figure 4.8. The outer ring corresponds to the second harmonic of the in-plane nearest-neighbour spacing, allowing us to measure the value of this lattice constant as $a = 0.30 \pm 0.01$ nm. The inner ring corresponds to the second harmonic of the second-nearest neighbour spacing $\sqrt{3}a$. The central bright dot does not carry any crystal information, instead it represents the infinite-wavelength component of the original TEM image, i.e. its intensity offset. The bright dots around the center are all at a radius of 0.62 nm which corresponds to the inter-layer spacing of the TMD crystal. The continuity of the rings indicates that there is no dominant crystal orientation and that the material is instead polycrystalline, consisting of randomly oriented crystallites or grains, separated by grain boundaries.

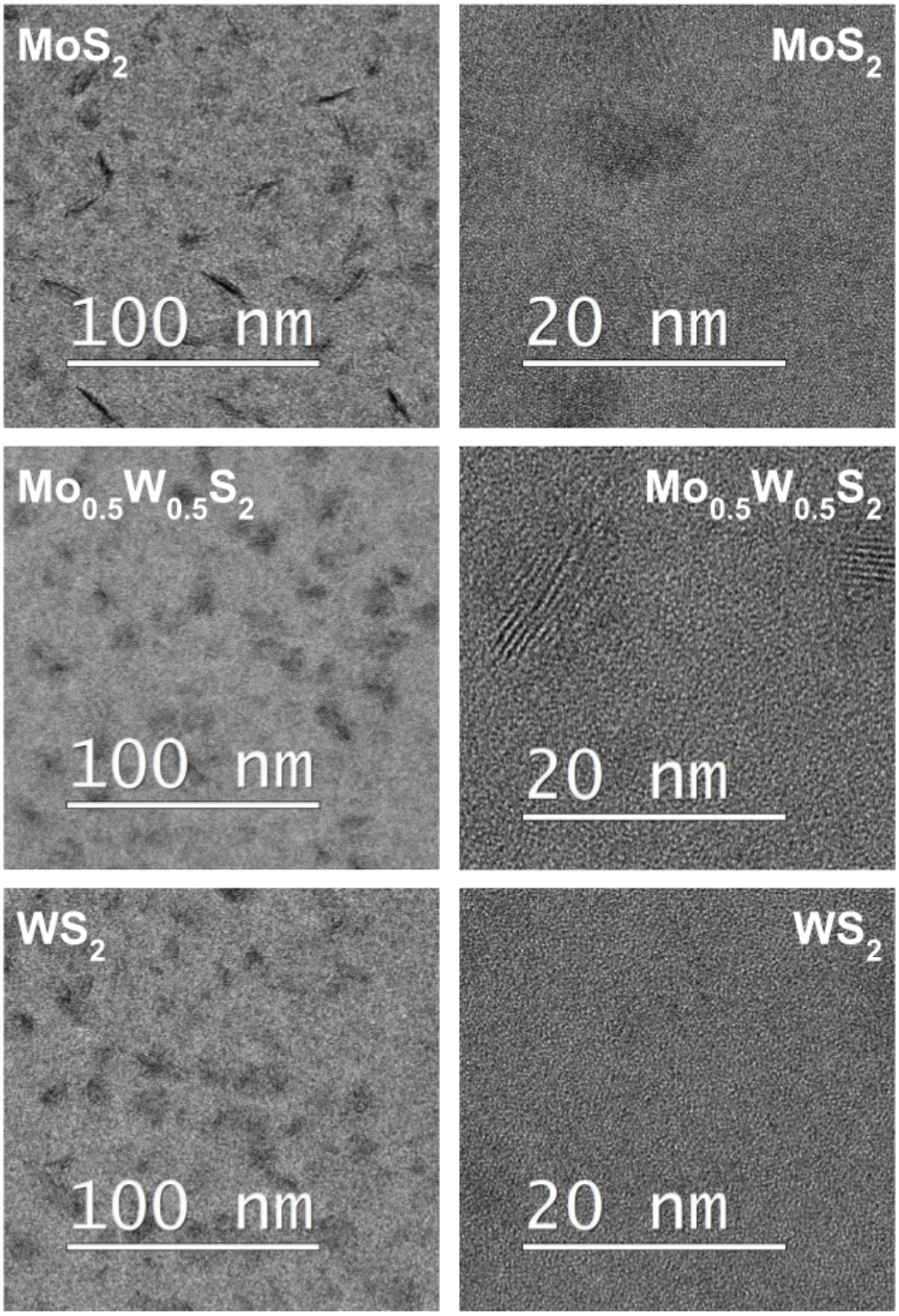

Figure 4.7: Transmission electron microscopy images of the ALD-deposited MoS_2, WS_2 and $Mo_xW_{1-x}S_2$alloy with Mo W cycle ratio of 2:3. The visible fringes are out-of-plane oriented crystals whose interlayer spacing of 0.62 nm can be identified from the Fourier transform in figure 4.8.

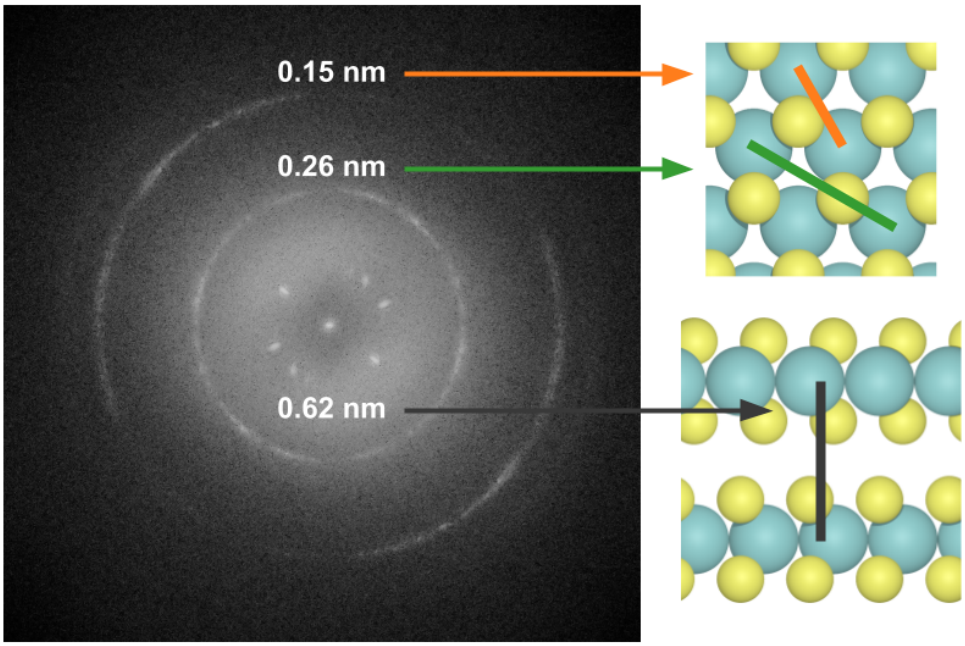

Figure 4.8: Fourier transform of a TEM image of the $Mo_{0.5}W_{0.5}S_2$ alloy. The two concentric circles correspond to the second harmonics of in-plane lattice spacings, as indicated. From the radii of these circles, the crystal structure of the deposited films can be verified. The bright dots around the center correspond to the inter-layer spacing and originate from out-of-plane oriented crystallites.

4.3.2 Alloy ratio effects

In the last section we have studied the growth and crystallinity of the ALD-deposited $Mo_xW_{1-x}S_2$ films and have demonstrated the composition control achieved by this synthesis method. We now turn our attention to the effects on the electronic properties of the 2D alloys that are enabled by this control.

Bandgap and photoluminescence Bulk MoS_2 and WS_2 have indirect electronic bandgaps, which transition to direct bandgaps at monolayer thickness. Direct bandgaps have the nice property that they can be measured directly by means of photoluminescence measurements. In these measurements, excitons are created by excitation with a laser. In their subsequent recombination, these excitons emit light whose frequency is a measure of the bandgap magnitude. In order to measure photoluminescence from the $Mo_xW_{1-x}S_2$ films, a new series of samples was deposited with the same Mo:W cycle ratios of 5:0, 4:1, 3:2, 2:3, 1:4 and 0:5 but with a reduced number of ALD cycles in order to achieve monolayer thickness. A number of 15 cycles was found to be optimal as samples deposited with 10 or 20 cycles showed no significant photoluminescence. Figure 4.9 shows the photoluminescence spectra recorded from the $Mo_xW_{1-x}S_2$ films deposited using 15 cycles. The pure MoS_2 and WS_2 films show dominant peaks at 1.88 eV and 2.02 eV respectively, which correspond to the direct bandgaps of these materials [86]. All of the intermediate alloys, including the most tungsten-rich, produce a photoluminescence spectrum dominated by a MoS_2-like peak centered at 1.86-1.88 eV. To gain more insight into this effect, the direct bandgaps of the monolayer alloys were calculated with DFT as a function of the atomic Mo:W ratio. Since the planewave DFT method relies on periodic boundary conditions, the monolayers were separated by 1.5 nanometers of vacuum in order to mitigate interactions between the periodic images. The calculated bandgaps are shown in figure 4.10. As also noted in the last chapter, the bandgaps calculated with the PBE exchange-correlation functional consistently underestimate the experimental values. On the other hand, the difference between the MoS_2 and WS_2 bandgaps is predicted to be 0.137 eV, which is in line with the difference of 1.4 eV measured by photoluminescence. However, a quantitative interpretation of these data should take into account the significant exciton binding energy in these materials which shifts the optical bandgap measured by photoluminescence away from the true electronic bandgap. In monolayers of MoS_2 and WS_2, these binding energies are 1.02 eV and 1.05 eV respectively, yielding an electronic bandgap difference between MoS_2 and WS_2 of 1.7 eV.

The trend in bandgap magnitude as a function of the alloy ratio is seen to be parabolic from the DFT data. This is in contrast with the photoluminescence data, where a constant MoS_2-like bandgap is observed for all intermediate alloys. This may be explained by preferential migration of excitons to local clusters of MoS_2 within the alloy, which would be energetically favorable due to the lower bandgap in these regions. The subsequent recombination of the excitons at these positions would result in the MoS_2-like photoluminescence spectrum that is observed.

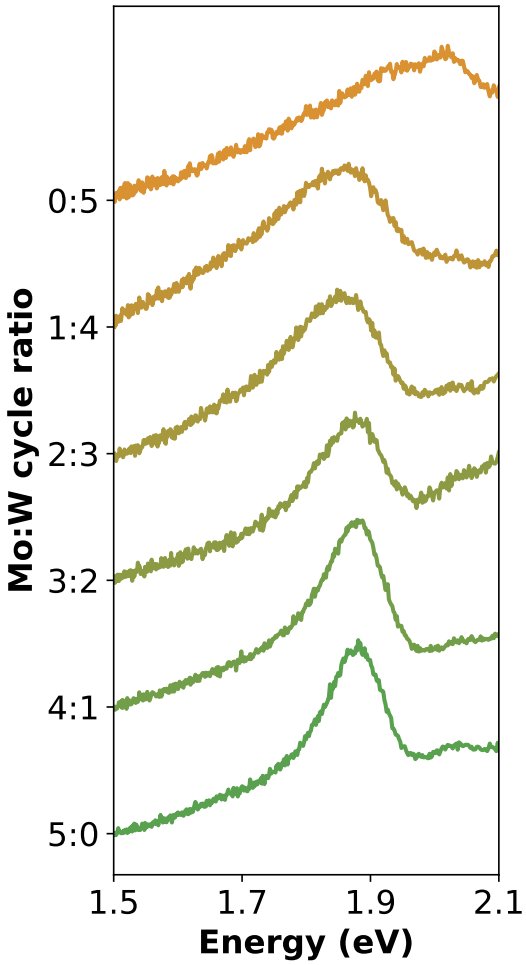

Figure 4.9: Photoluminescence spectra of $Mo_xW_{1-x}S_2$ films grown by 15 cycles of ALD. The A-excitons of MoS_2 and WS_2 can be observed in the 5:0 and 0:5 spectra, with energies of 1.88 eV and 2.02 eV respectively. All intermediate alloys are dominated by an MoS_2-like photoluminescence peak which we attribute to the energetically favorable exciton migration to MoS_2 clusters within the alloys.

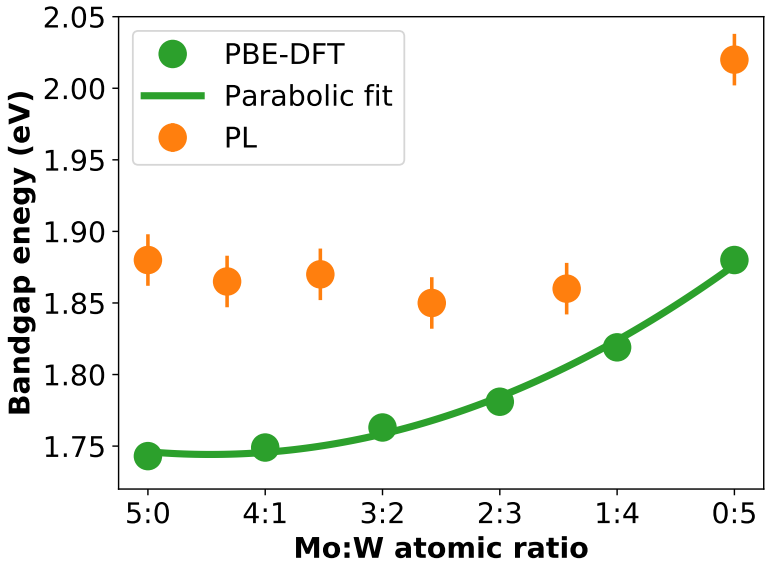

Figure 4.10: Electronic bandgap magnitudes for monolayers of MoS_2, WS_2 and intermediate alloys calculated with DFT at the PBE level compared to values obtained from photoluminescence measurements. DFT error bars of one standard deviation are 0.005 eV in magnitude, which coincides with the size of the markers. The atomic Mo:W ratios of the PL samples were calculated from their Mo:W ALD cycle ratio using the calibration in figure 4.5.

Electronic transport The electrical resistivity of the ALD-deposited MoS_2, WS_2 and $Mo_xW_{1-x}S_2$ alloys was measured using the four-point-probe technique: results are shown in figure 4.11a. The measured resistivities are on the order of 10^3 Ωcm. This is high compared to WS_2 films grown by others in our group, which may be attributed to the strong dependence of the resistivity of these materials on the thickness of the films in the few-nanometer regime. The intermediate alloys were found to be less resistive than the pure MoS_2 and WS_2 by a factor of 2. In order to gain an understanding of this effect, we employed density functional theory to perform effective mass calculations on these alloys. Resistivity is proportional to the effective mass through its dependence on the carrier mobility:

$$\frac{1}{\rho} = ne\mu, \tag{4.1}$$

with the mobility μ a function of the effective carrier mass m^* and the mean scattering time of the carriers $\bar{\tau}$:

$$\mu = e\frac{\bar{\tau}}{m^*}. \tag{4.2}$$

The calculated effective carrier masses are shown in figure 4.11b. The electron effective masses depend quadratically on the atomic Mo:W ratio of the alloy, reaching a maximum value 20% higher than pure MoS_2 and WS_2 at a 50/50 alloy ratio. On the other hand, the effective hole mass decreases linearly from pure MoS_2 through the alloys to WS_2. Synthesized MoS_2 and WS_2 are known to usually be n-type semiconductors, so the electron effective mass is the most relevant quantity. Based on the higher effective electron mass of the alloys, their resistivity would be expected to be higher than the pure TMDs. However, this is contradicted by the four-point-probe measurements. Additionally, the 20% difference in effective mass cannot account for the factor 2 change which is observed in the resistivity. Evidently, either the carrier concentration (equation (4.1)) or the scattering time (equation (4.2)) are more important than the effective mass in determining the resistivity of the $Mo_xW_{1-x}S_2$ alloys. A likely explanation of the observed low resistivity is a decrease in scattering time due to reduced crystallinity of the alloys compared to the pure MoS_2 and WS_2. This effect was also suggested by the lower Raman intensity from the alloy samples as shown in figure 4.6.

4.3.3 Alloy mixing effects

Due to its atomic-scale growth control, the synthesis technique of atomic layer deposition offers unparalleled control over the degree of mixing of the deposited 2D alloys. To investigate the effect of atomic-scale mixing, three samples were made with Mo:W cycle alternations of 1:1, 3:3 and 5:5 as illustrated in figure 4.12. Another three samples were deposited with the same alternation but with the order reversed, starting with tungsten cycles instead of molybdenum cycles. All six of these samples were made using the

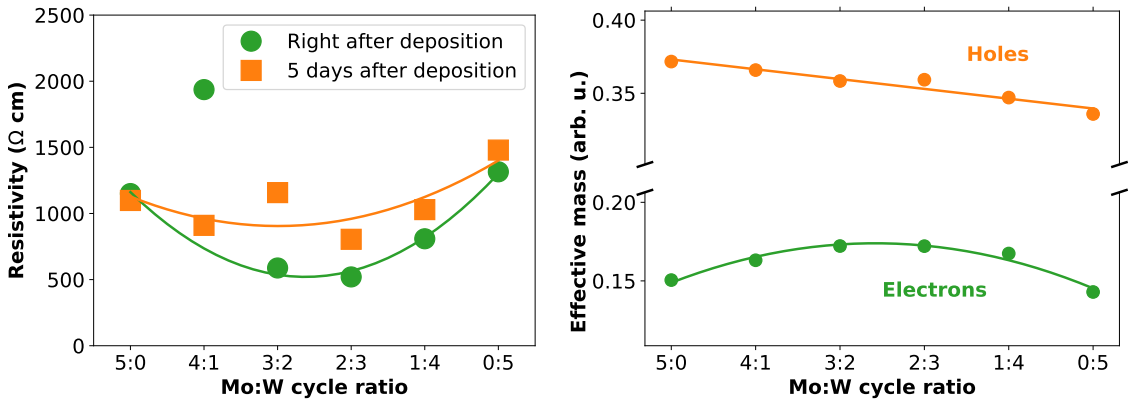

(a) Four-point probe

(b) DFT effective mass

Figure 4.11: Four-point probe resistivity and density functional theory calculated effective carrier masses.

same total number of ALD cycles such that all samples have the same alloy fraction and only differ in the degree of mixing of molybdenum and tungsten within the alloy.

Lattice vibrations Raman spectroscopy was performed on the six samples with different molybdenum-tungsten mixing and the spectra are shown in figure 4.13. Qualitatively, the spectra are similar to those from the alloys with intermediate alloy ratio in figure 4.6, which is as expected based on their alloy ratio. Between the Raman spectra of differently-mixed alloys, there is a distinct change in the separation of the two A_{1g} peaks. While peaks are visibly separated for the sample with 5:5 cycle alternation, they are closer together in the 3:3 sample, merging into one for the 1:1 sample. The fact that the total width of the combined A_{1g} peaks decreases as the same time shows that this merging is not merely a broadening effect and a frequency shift must be involved. In order to quantify these frequency shifts, the Raman spectra were deconvoluted to obtain the peak positions of both the E_{2g} and A_{1g} peaks. As an example, the deconvolution of the Raman spectra of the sample with 3:3 cycle mixing, W-first is shown in figure 4.14. Deconvolution is more straightforward for the A_{1g} peaks than for the E_{2g} peaks since the E_{2g} peak of WS_2 overlaps with contributions from other phonons. These additional peaks which were not fully modeled in the deconvolution procedure since our focus is on the A_{1g} phonons. The deconvoluted peak positions in figure 4.15 confirm the convergence of the two A_{1g} peaks as the alloys are better mixed, showing shifts in the range of 1 to 2 wavenumbers. Evidently, the molybdenum-tungsten mixing in the ALD-deposited $Mo_xW_{1-x}S_2$ alloys has some impact on their structure, causing the frequencies of their characteristic out-of-plane A_{1g} vibration to shift. In the next section, we attempt to gain insight into this mechanism by theoretical modeling of the A_{1g} vibration in these alloys.

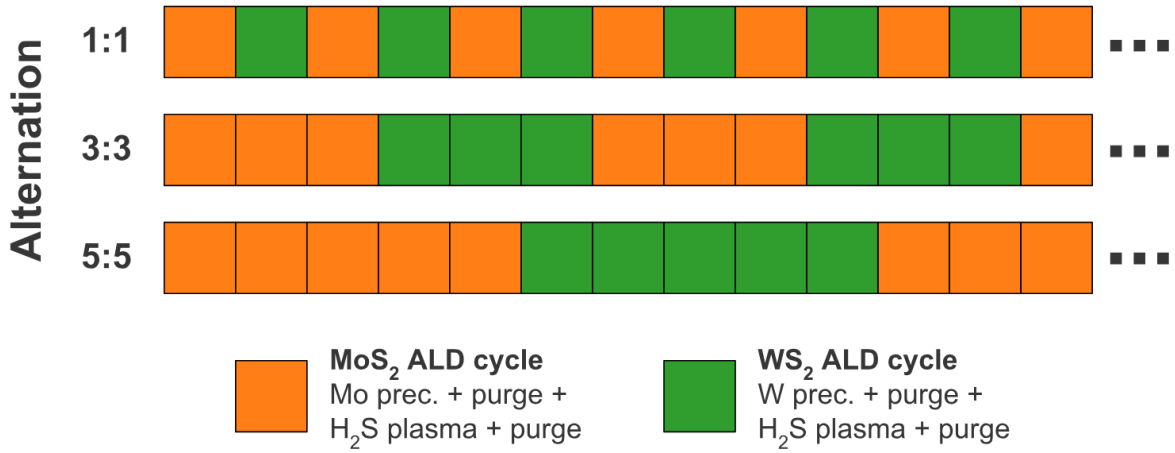

Figure 4.12: Method of controlling the mixing of the ALD-deposited $Mo_xW_{1-x}S_2$ by changing the alternation of the Mo and W cycles. The total number of cycles was chosen such that the alloy ratio could be kept constant in order to isolate the effects of atomic-scale ordering.

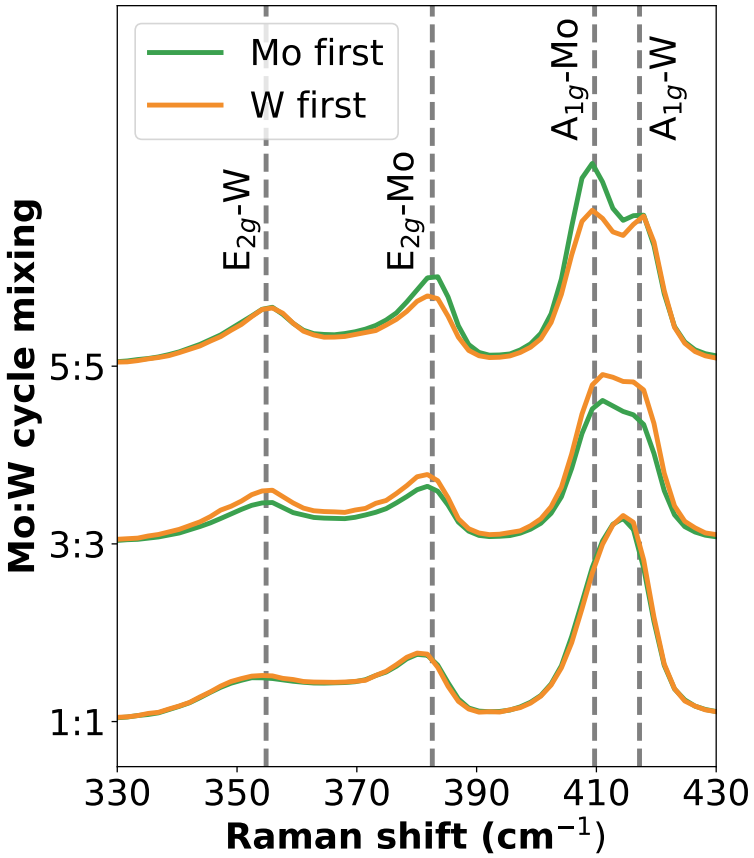

Figure 4.13: Raman spectra of ALD-deposited alloys with constant alloy fraction $Mo_{0.6}W_{0.4}S_2$ and different degrees of mixing, effectuated by alternating the molybdenum and tungsten ALD cycles as illustrated in figure 4.12. The characteristic A_{1g} and E_{2g} modes of MoS_2 and WS_2 are labeled. The colors indicate whether Mo or W was dosed first in the deposition process.

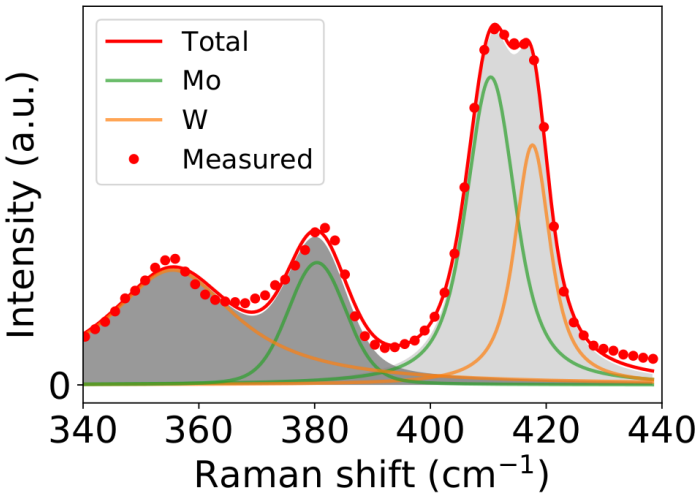

Figure 4.14: Deconvolution of the Raman spectrum of the $Mo_xW_{1-x}S_2$ sample deposited with Mo:W cycle alternation of 3:3. Deconvolution of the E_{2g} peaks (left) is made difficult by the overlapping E_{2g} and defect-enabled $LA(M)$ peaks of WS_2, which we have not treated separately. The positions of the A_{1g} peaks (right) can be resolved much more accurately.

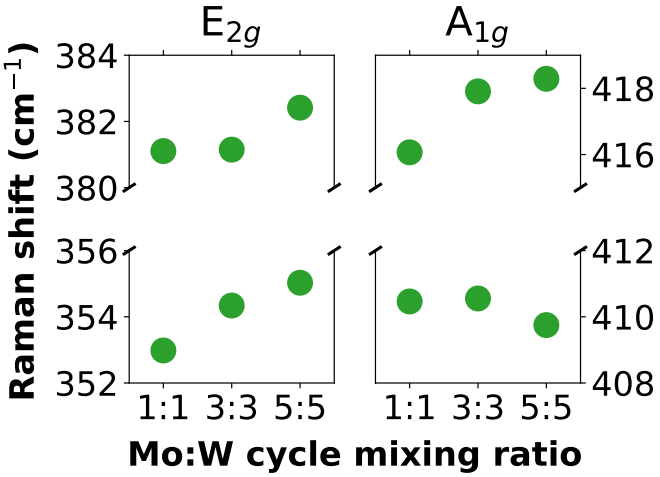

Figure 4.15: Frequencies of the characteristic Raman peaks of the $Mo_{0.6}W_{0.4}S_2$ alloys as a function of the cycle mixing ratio. Data is shown for the three samples of which the supercycle started with molybdenum ALD cycles; results were similar for the samples whose supercycles started with tungsten cycles. A clear divergence between the two A_{1g} peaks is seen as the mixing of molybdenum and tungsten becomes coarser.

Theoretical modeling of the A_{1g} vibration in $Mo_xW_{1-x}S_2$ alloys

As a first approximation we can model effect of atomic mixing on the A_{1g} vibrational frequency by treating the primitive cells of MoS_2 and WS_2 as harmonic oscillators. When independent, each oscillator will have an oscillation frequency porportional to the square root of the ratio of its elastic constant and its mass. Since in the A_{1g} vibration the metal atom is stationary while sulfur atoms oscillate in the out-of-plane direction, the masses of the two oscillators are equal. The Raman spectra show that the frequency of the A_{1g} vibration is higher in WS_2 than in MoS_2, indicating that the WS_2 oscillator has a larger elastic constant. When these two oscillators are coupled together, as they would be in a well-mixed alloy, their common oscillation frequencies are given by

$$(\frac{-k_{MoS_2}-\kappa}{m_S}+\omega^2)(\frac{-k_{WS_2}-\kappa}{m_S}+\omega^2)=\frac{\kappa^2}{m_S^2}, \tag{4.3}$$

where κ is the coupling strength between the oscillators, k_{MoS_2} and k_{WS_2} are the elastic constants and m_S is the atomic sulfur mass. Based on this equation, the expected behaviour is that both oscillation frequencies shift towards higher frequencies, which is contradictory to the bidirectional shifts of the A_{1g} frequencies we observe in the Raman spectra. Evidently, such a simplified picture of the situation is not sufficient to explain the observed phenomenon.

In order to gain more insight into the mechanism causing the mixing-dependent shift of the A_{1g} vibrational frequency, we employ density functional theory calculations to calculate the A_{1g} frequency in $Mo_xW_{1-x}S_2$ alloys. As a first approximation, we study clusters of WS_2 embedded in a MoS_2 supercell in order to investigate the effect of domain size on the A_{1g} frequency. These clusters are taken to be symmetric around a central sulfur atom such that vibrational mode mixing is mitigated and the out-of-plane perturbation of the sulfur atoms results in a pure vibration in the A_{1g} mode, with no other modes activated. In total, 7 different shapes and sizes of WS_2 clusters were investigated. In their definitions we refer to the nearest, second-nearest and third-nearest unit cells of the central sulfur atom as defined in figure 4.16. The 7 clusters are labeled as follows:

- 100: **only the nearest neighbouring** unit cells of the central sulfur atom are WS_2 cells, the rest of the 5x5 supercell consists of MoS_2 cells
- 010: **only the second-nearest neighbouring** unit cells of the central sulfur atom are WS_2 cells, the rest of the 5x5 supercell consists of MoS_2 cells
- 001: **only the third-nearest neighbouring** unit cells of the central sulfur atom are WS_2 cells, the rest of the 5x5 supercell consists of MoS_2 cells
- 101, 110, 011, 111: all possible combinations of the configurations above. For example, 101: the nearest neighbouring and third-nearest neighbouring unit cells of the central sulfur atom are WS_2 cells, the rest of the 5x5 supercell (including the second-nearest neighbours of the central sulfur atom) are MoS_2 cells.

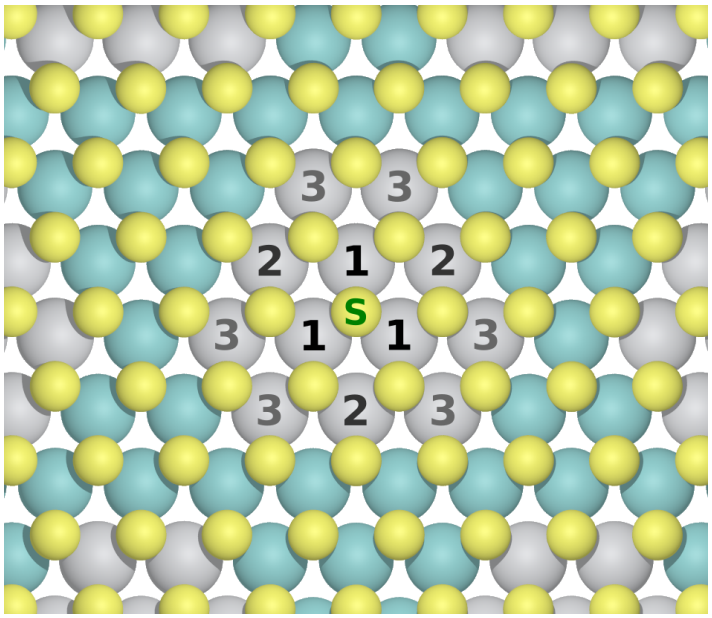

Figure 4.16: Definition of nearest (1), second-nearest (2) and third-nearest (3) neighbouring metal atoms of the central sulfur atom (S). The shown structure corresponds to the 111 cluster where the nearest, second-nearest and third-nearest neighbouring cells of the central sulfur atom are WS_2 cells, and the rest of the 5x5 supercell consists of MoS_2 cells.

Structural relaxations were performed on the 7 cluster-containing supercells, after which all sulfur atoms were displaced in the out-of-plane direction by 0.01 angstrom. From the calculation of the resulting restoring force, the local frequency of the A_{1g} vibration at the center of each cluster was derived. The results in figure 4.17 indicate that the nearest-neighbouring metal atoms have the biggest influence on the local A_{1g} frequency. The frequency of the A_{1g} frequency in the 1xx clusters is on average 15 wavenumbers higher than in the 0xx clusters. It is notable, however, that even the second-nearest and third-nearest neighbours have a significant impact on the local A_{1g} frequency, shifting its value by about 5 wavenumbers. These findings suggest that the extended atomic environment beyond the nearest neighbours are significant in determining the Raman response of $Mo_xW_{1-x}S_2$ alloys.

The simulations described above are insightful, but they do not permit a direct comparison to the Raman spectra of figure 4.13 as the alloy ratio is not kept constant in these simulations. As such, it could be argued that the effects seen in these simulations are merely an effect of the alloy ratio, and not of the degree of mixing. Hence, we performed additional DFT calculations on 5x5 supercells of $Mo_{0.6}W_{0.4}S_2$ alloys with constant alloy ratio and different degrees of mixing, effectuated by controlling the configuration of Mo and W atoms in the supercell. The number M of heterometallic Mo-W nearest neighbours will be used as measure of the mixing of the supercell. Lower M corresponds to more clustering and worse mixing, while higher M corresponds to

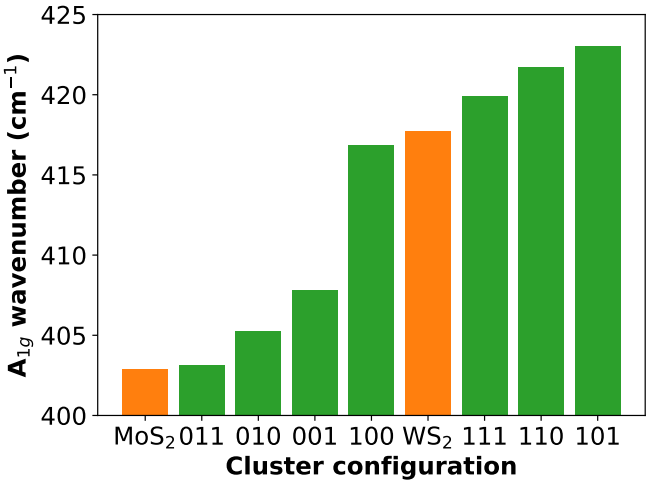

Figure 4.17: The local shift in the A_{1g} vibrational frequency in symmetric clusters of WS_2 embedded in MoS_2. Labeling: the first digit indicates whether the nearest neighbouring metal atoms are tungsten (1) or molybdenum (0). The second and third digit determine the second-nearest and third-nearest neighbours in the same way. The definition of nearest, second-nearest and third-nearest neighbours is given in figure 4.16. Frequencies of the A_{1g} vibrations in pure MoS_2 and WS_2 calculated with the same parameters are included as reference.

more uniform distribution and better mixing of the Mo and W atoms in the alloy. We may calculate the expectation value of M for an optimally mixed alloy, which depends only on its alloy ratio in the limit of an infinitely large supercell. Considering a supercell with atomic Mo:W ratio of 6:4, the six neighbouring metal atoms of any metal atom will on average be $0.6 \cdot 6 = 3.6$ Mo atoms and $0.4 \cdot 6 = 2.4$ W atoms. In a 5x5 supercell, this results in an expectation value of $M = \frac{1}{2} \cdot 25 \cdot (0.6 \cdot 3.6 + 0.4 \cdot 2.4) = 39$, where division by 2 avoids double-counting the pairs. More generally, for a supercell consisting of N cells, the expectation value of M can be expressed as

$$\frac{M}{N} = \frac{1}{2} \cdot 6 \cdot (x^2 + (1-x)^2), \tag{4.4}$$

where x is the alloy fraction. Thus, an optimally-mixed $Mo_{0.6}W_{0.4}S_2$ alloy will have $\frac{M}{N} = 1.56$. The range of $\frac{M}{N}$ that can be simulated depends on the size of the supercell. To illustrate this, figure 4.18 shows the minimum (0.8) and maximum (2.0) values that can be achieved with a 5x5 supercell. The practically useful range is smaller still, since these extreme values can only be achieved by highly ordered, low-entropy configurations as shown in figure 4.18. Since the value for an optimally mixed alloy is 1.56, the maximum value is not a practical restriction. However, the minimum value inhibits investigation of alloys with low degrees of mixing. In other words, effects of clustering on scales larger than the supercell cannot be examined. Extending the least-mixed

configuration of figure 4.18 to larger supercells of size $N = n \times n$, the lowest achievable value of $\frac{M}{N}$ can be expressed as

$$\left(\frac{M}{N}\right)_{min} = \frac{4n}{n^2} \propto \frac{1}{n} = \frac{1}{\sqrt{N}}. \tag{4.5}$$

For our present calculations, however, we stick to a supercell size of 5×5. We study three structures with mixing degrees $\frac{M}{N}$ of 1.20, 1.52 and 1.76, as shown in figure 4.19. Structural relaxation on these supercells was performed and the sulfur atoms were subsequently displaced in the out-of-plane direction by 0.01 angstrom. Unlike in our calculations on symmetric clusters before, in these calculations we record the oscillation frequencies of all sulfur atoms in the 5x5 supercell. In order to plot how the A_{1g} frequencies depend on the atomic environment, we introduce a metric such that the environment can be classified by a single number. This number is obtained in the following way: for each sulfur atom, a circular region of radius R is defined concentrically around the atom. For each tungsten atom within this circle, add $1/d$ to the number, where d is the distance from the tungsten atom to the sulfur atom. For each molybdenum atom, subtract $1/d$. The resulting number will thus be more positive for a tungsten-rich environment and more negative for a molybdenum-rich environment, and metal atoms further away contribute less than those closer to the sulfur atom. In figure 4.20 we plot the calculated A_{1g} frequencies of all sulfur atoms in the supercells shown in figure 4.19 as a function of their local atomic environment as defined above. Two main clusters can be observed in the data: one of lower frequency in molybdenum-rich environments, and one of higher frequency in tungsten-rich environments. These resemble the two A_{1g} peaks which are seen in the Raman spectra of the ALD-synthesized alloys in figure 4.13. This is illustrated in figure 4.21, where we have reconstructed a Raman spectrum from the DFT data for the configurations with mixing degrees $\frac{M}{N}$ of 1.2 and 1.52. This was done by summing over the frequency data points of figure 4.20 and applying a Gaussian broadening of $\sigma = 3$ cm^{-1}. Additionally, the frequency axis was shifted by 20 cm^{-1} in order to match the experimental data taken from figure 4.13, which is shown by the dotted and dashed lines. We see that the shape of the Raman reponse of the sample with low mixing (5:5 cycle alternation) is closely approximated by the DFT-generated Raman spectrum with mixing degree $\frac{M}{N} = 1.2$, demonstrating that the used approach works. On the other hand, the peak shifts observed in Raman spectrum of the the well-mixed (1:1 cycle alternation) sample are not seen in the DFT-generated Raman spectrum of mixing degree $\frac{M}{N} = 1.52$. Instead, in both DFT-generated Raman spectra, the peak positions remain nearly constant. Simulations of higher degrees of mixing are not expected to be relevant, as the currently-used value of $\frac{M}{N} = 1.52$ is already close to the value of 1.56 of an optimally-mixed alloys. The observed discrepancy between the experimentally measured Raman spectra and the DFT-reconstructed Raman spectra suggests that the experimentally observed shifts in the A_{1g} frequencies as a function of alloy mixing may instead be the result of larger-scale collective effects than were probed by our calculations using a 5x5 supercell.

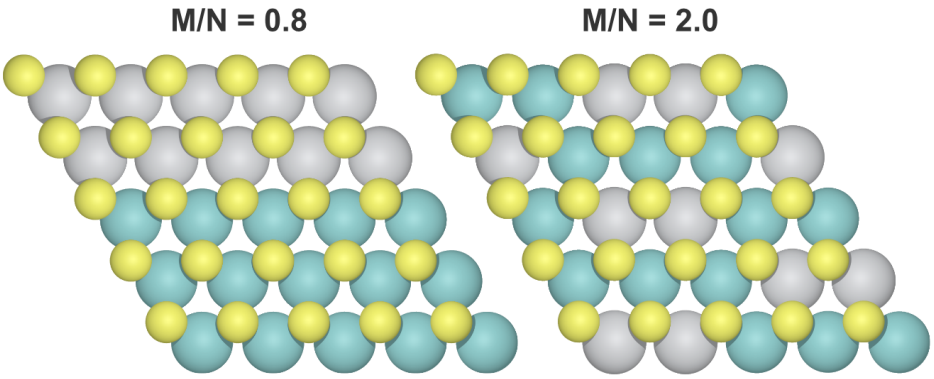

Figure 4.18: The lowest and highest degrees of mixing that can be simulated in a 5x5 supercell correspond to $\frac{M}{N}$ values of 0.8 and 2.0 respectively. However, these degrees of mixing can only be achieved with a single highly ordered configuration, making these cases physically irrelevant due to their low entropy.

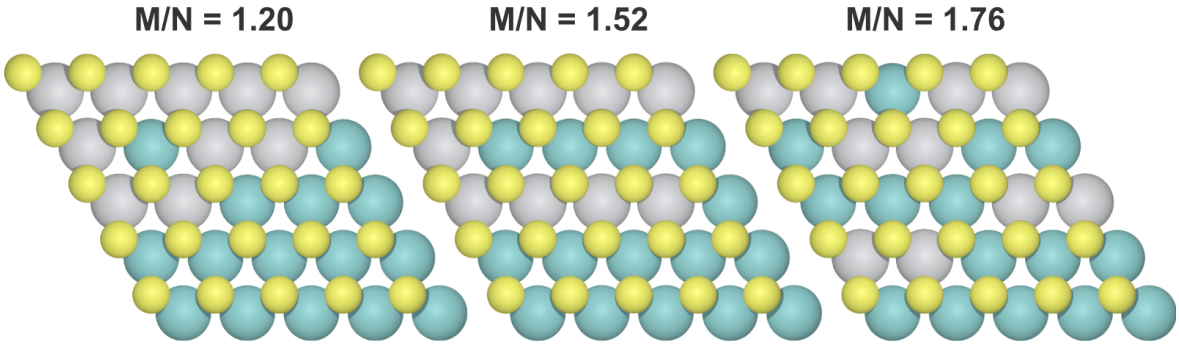

Figure 4.19: Three supercells with realistic degrees of mixing, intermediate to the minimum and maximum attainable values in a 5x5 supercell. These structures were used to study the mixing-dependent A_{1g} frequency in $Mo_xW_{1-x}S_2$ alloys.

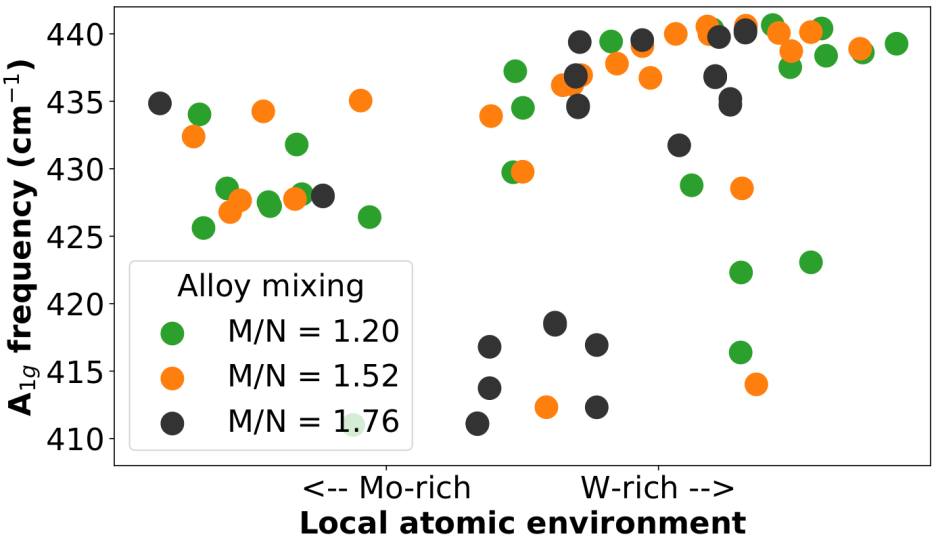

Figure 4.20: DFT-calculated A_{1g} vibrational frequencies as a function of the local atomic environment in $Mo_xW_{1-x}S_2$ alloys with different degrees of mixing. The numerical definitions of the local environment and the degree of mixing are given in the text.

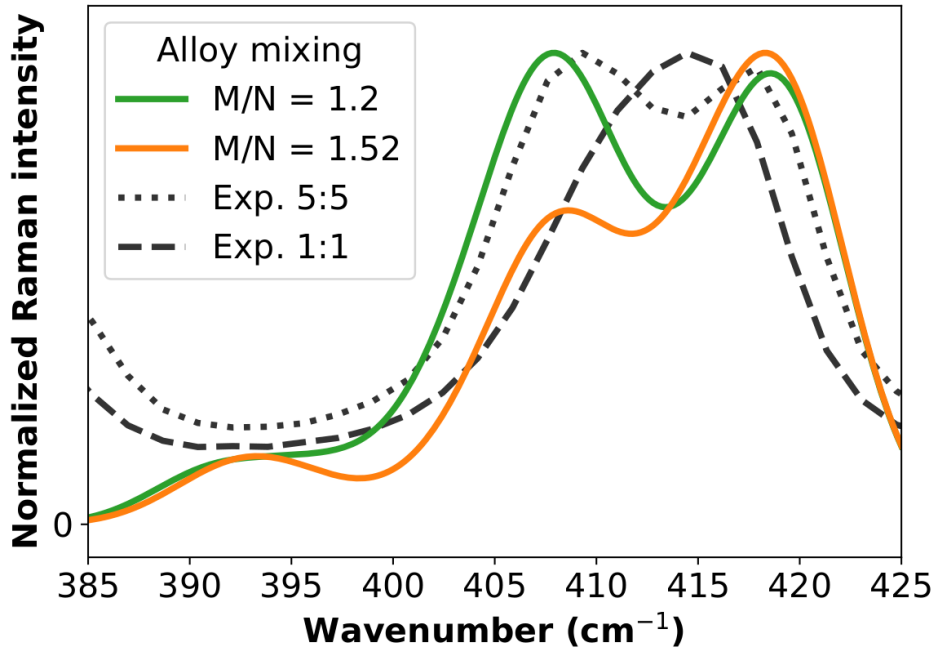

Figure 4.21: Reconstructed Raman spectra from the DFT datasets from figure 4.20 for mixing degrees of $\frac{M}{N} = 1.2$ and 1.52. Gaussian broadening of 3 cm^{-1} was used, and the frequency axis is shifted by 20 cm^{-1} in order to match the experimental data shown by the dashed and dotted lines.

4.4 Conclusions

We have elucidated the trends in bandgap, effective mass, resistivity and A_{1g} phonon frequency in ALD-synthesized $Mo_xW_{1-x}S_2$ alloys by performing DFT calculations on these materials. The synthesis of the alloys was done using a novel direct atomic layer deposition process based on supercycles of MoS_2 and WS_2. Accurate control over the alloy fraction was achieved, as evidenced by x-ray photoelectron spectroscopy. Electrical resistivities of the alloys were lower than of pure MoS_2 and WS_2 deposited using the same process. From a comparison to calculations of the effective carrier masses, the reason for the lower resistivity appears to be a reduced crystallinity of the alloys, of which their reduced Raman intensity is an indication. The photoluminescence spectra of monolayers of $Mo_xW_{1-x}S_2$ alloys are MoS_2-like, independent of their alloy ratio. Since the calculated bandgaps of these materials instead show a parabolic dependence on the alloy ratio, we explain the measured PL spectra by migration of excitons to local clusters of MoS_2 within the alloy, driven by a smaller bandgap in these regions. Additionally, the effect of the degree of mixing of the alloys was investigated. The sub-monolayer growth control inherent to ALD was exploited to deposit films with a constant alloy ratio but a different degree of mixing. A non-trivial consequence of the mixing was observed in the vibrational spectra of the alloys as measured with Raman spectroscopy. The separation between the out-of-plane A_{1g} vibrational peaks of MoS_2 and WS_2 decreases as the alloy mixing becomes more homogeneous, with both peaks shifting towards each other. Advanced DFT calculations were employed to explain the observed A_{1g} frequency shifts in these alloys. By simulating clusters of WS_2 embedded in a supercell of MoS_2, the extended atomic environment beyond the nearest neighbours was found to be significant in determining the local frequency of the A_{1g} vibration. Additional simulations on supercells with constant alloy ratio and different degrees of mixing were successfully used to reconstruct experimentally measured Raman spectra. The experimentally observed shifts in A_{1g} frequency were not observed in these simulations, indicating that these shifts may be caused by collective interactions on length scales larger than can be investigated by use of a 5x5 supercell.

Chapter 5

Conclusions

The goal of this work was to achieve insight into how the electronic properties of transition metal dichalcogenides can be controlled. To this end, Density Functional Theory was used to perform ab-initio electronic structure calculations of pristine TMDs and subsequently extend these to a supercell approach to model realistic concentrations of typical point defects in TMDs. Finally, we employed the supercell calculation approach to the binary TMD alloys $Mo_xW_{1-x}S_2$. The calculated bandgaps, effective carrier masses and phonon frequencies were compared to measurements on thin films of these alloys, synthesized using a newly developed atomic layer deposition process based on supercycles of MoS_2 and WS_2. In the introduction to this thesis we posed three research questions, which we are now in a position to address:

1. *Can density functional theory (DFT) be used to calculate structural and electronic properties like lattice parameters, bandgap, carrier mobility and phonon frequencies of transition metal dichalcogenides with enough accuracy to compare them to experimental results?*

   In order to obtain the highest possible accuracy in our calculations, we have systematically optimized our DFT calculation parameters, most importantly the planewave cutoff energy and the Brillouin zone sampling density. With these converged calculation parameters, the lattice constants of MoS_2 and WS_2 are predicted very accurately, differing less than half a percent from their experimental values. The electronic bandgaps of both bulk crystals and monolayers of MoS and WS_2 were shown to be more challenging to calculate accurately with DFT: their magnitudes are consistently underestimated by about 0.2-0.3 eV. This is a known shortcoming of the PBE exchange-correlation functional we used, and more advanced DFT approaches such as the use of hybrid functionals or Green's function based methods can be used to calculate these bandgaps more accurately, at a higher computational cost. However, the inaccuracy in the bandgap magnitude does not carry over to the effective carrier masses, which is calculated from the curvature of the valence and conduction bands. In fact, the values of the effective carrier masses are in good agreement with literature values, indicating that the

inaccuracy of the bandgap as calculated using the PBE functional corresponds to a rigid shift of the energy bands which does not significantly affect their curvature. The vibrational structure of MoS_2 and WS_2 was probed with DFT by calculating the restoring force acting on the sulfur atoms as a function of their displacement in the A_{1g} vibration of these materials. In the harmonic approximation, the frequency of this oscillation could be calculated with an accuracy of 4%. For large displacements, anharmonicity is observed in the force-displacement curve, which is also in line with expectations.

In conclusion, it can be said that the crystal structure of TMDs can be calculated up to experimental accuracy using DFT. While the PBE exchange-correlation functional underestimates the bandgaps of these materials, the effective carrier masses derived from the curvature of the valence and conduction bands are in line with calculations using more sophisticated exchange-correlation functionals. Additionally, phonon frequencies can be calculated with sufficient accuracy to identify them with peaks observed in Raman spectra.

2. *What role do crystal defects play in determining the electronic properties of transition metal dichalcogenides?*

   We employed a supercell method to DFT in order to model realistic concentrations of typical point defects found in synthesized TMDs. From relaxation heatmaps of the defect sites, the structural impact of the defects on the crystal lattice was shown to be highly localized around the defect sites. In order to obtain the electronic properties of MoS_2 with point defects, unfolding of the energy bands was performed, yielding an effective band structure from which the effective carrier masses were extracted. The resulting effective masses differ from their values in the pristine material by no more than a factor of two, indicating that changes in the effective mass are not limiting the mobility in TMDs with point defects. It should be noted, however, that these types of defects may still have a significant impact on the carrier mobility by acting as dopants, that is, by changing the carrier concentration in the material. Additionally, other factors such as the presence of grain boundaries or electron-phonon scattering are expected to have a larger impact than point defects on the electronic properties.

3. *How can the atomic ordering of binary TMD alloys be exploited to achieve control over their electronic properties?*

   We conducted a combined theoretical and experimental investigation into the binary TMD alloys of $Mo_xW_{1-x}S_2$. We identified two parameters that could be manipulated to control the properties of the alloys: their alloy ratio and their degree of atomic mixing. Changing the alloy ratio allowed control over the resistivity, which were shown by DFT calculations to not be caused by changes in the effective mass. Instead, this change in resistivity may be caused by a reduced crystallinity, which was also suggested by the measured Raman spectra. This

indicates that the effective mass is not limiting the resistivity in these materials. On the other hand, the atomic-scale mixing of the alloys was investigated by exploiting the atomic-scale growth control of the atomic layer deposition technique. The mixing was shown to have a distinct effect on the Raman spectra of the alloys, shifting and merging the two A_{1g} vibrational peaks together when the degree of mixing was increased. These shifts were investigated by calculating the A_{1g} vibrational frequencies with DFT for clusters of WS_2 embedded in MoS_2. The results indicate that while the nearest-neighbouring unit cells are most important in determining the local A_{1g} frequency, the extended environment of second-nearest and third-nearest neighbours also have non-negligible influence, shifting the local A_{1g} frequency by up to 5 wavenumbers. Additional calculations were devised where the effect of differently-mixed supercells on the local A_{1g} frequency was investigated. While these calculations enabled a qualitative reconstruction of the observed Raman spectra, the mixing-dependent shifts in the A_{1g} frequency were not observed. As such, these shifts are suggested to be caused by collective effects on length scales longer than was investigated using a 5x5 supercell.

Recommendations

In order to further elucidate the observed mixing-dependent shifts in the Raman frequencies of the A_{1g} vibrations of the $Mo_xW_{1-x}S_2$ alloys, it would be insightful to attempt DFT phonon calculations using larger supercells than 5x5. While the physically relevant optimum mixing can already be probed with the 5x5 cell, the larger number of oscillators that are present in larger supercells would allow for more in-depth statistics on the calculated oscillation frequencies. Additionally, there may be large-scale correlations that only emerge for larger supercells and that cause the experimentally observed frequency shifts. Deeper investigations of the low-mixing regime would also be enabled by the adoption of larger supercells, which may provide additional ways of controlling the material properties of the TMDs, analogously to 2D heterostructures but in the in-plane dimension. Experimentally, it would be interesting to combine different alloy ratios with different degrees of mixing. Enormous freedom is provided by these two parameters, which could even be changed during the deposition, for example by changing the degree of mixing halfway through the deposition. Finally, it would be helpful to have a way of estimating the value of the mixing parameter $\frac{M}{N}$ for ALD-deposited alloy samples in order to facilitate a more accurate comparison between the experimental and theoretical data.

Bibliography

[1] K. S. Novoselov, A. K. Geim, S. V. Morozov, D. Jiang, Y. Zhang, S. V. Dubonos, I. V. Grigorieva, and A. A. Firsov. Electric field effect in atomically thin carbon films. *Science*, 306(5696):666–669, 2004.

[2] Kostya S Novoselov, Andre K Geim, SVb Morozov, Da Jiang, MIc Katsnelson, IVa Grigorieva, SVb Dubonos, and AA Firsov. Two-dimensional gas of massless dirac fermions in graphene. *nature*, 438(7065):197, 2005.

[3] Yuanbo Zhang, Yan-Wen Tan, Horst L Stormer, and Philip Kim. Experimental observation of the quantum hall effect and berry's phase in graphene. *nature*, 438(7065):201, 2005.

[4] Jl A Wilson and AD Yoffe. The transition metal dichalcogenides discussion and interpretation of the observed optical, electrical and structural properties. *Advances in Physics*, 18(73):193–335, 1969.

[5] K. S. Novoselov, D. Jiang, F. Schedin, T. J. Booth, V. V. Khotkevich, S. V. Morozov, and A. K. Geim. Two-dimensional atomic crystals. *Proceedings of the National Academy of Sciences*, 102(30):10451–10453, 2005.

[6] Wonbong Choi, Nitin Choudhary, Gang Hee Han, Juhong Park, Deji Akinwande, and Young Hee Lee. Recent development of two-dimensional transition metal dichalcogenides and their applications. *Materials Today*, 20(3):116 – 130, 2017.

[7] Kenji Watanabe, Takashi Taniguchi, and Hisao Kanda. Direct-bandgap properties and evidence for ultraviolet lasing of hexagonal boron nitride single crystal. *Nature materials*, 3(6):404, 2004.

[8] Li Song, Lijie Ci, Hao Lu, Pavel B. Sorokin, Chuanhong Jin, Jie Ni, Alexander G. Kvashnin, Dmitry G. Kvashnin, Jun Lou, Boris I. Yakobson, and Pulickel M. Ajayan. Large scale growth and characterization of atomic hexagonal boron nitride layers. *Nano Letters*, 10(8):3209–3215, 2010. PMID: 20698639.

[9] Fengnian Xia, Han Wang, and Yichen Jia. Rediscovering black phosphorus as an anisotropic layered material for optoelectronics and electronics. *Nature communications*, 5:4458, 2014.

[10] Likai Li, Yijun Yu, Guo Jun Ye, Qingqin Ge, Xuedong Ou, Hua Wu, Donglai Feng, Xian Hui Chen, and Yuanbo Zhang. Black phosphorus field-effect transistors. *Nature nanotechnology*, 9(5):372, 2014.

[11] Patrick Vogt, Paola De Padova, Claudio Quaresima, Jose Avila, Emmanouil Frantzeskakis, Maria Carmen Asensio, Andrea Resta, Bénédicte Ealet, and Guy Le Lay. Silicene: compelling experimental evidence for graphenelike two-dimensional silicon. *Physical review letters*, 108(15):155501, 2012.

[12] Cheng-Cheng Liu, Wanxiang Feng, and Yugui Yao. Quantum spin hall effect in silicene and two-dimensional germanium. *Physical review letters*, 107(7):076802, 2011.

[13] ME Dávila, Lede Xian, Seymur Cahangirov, Angel Rubio, and Guy Le Lay. Germanene: a novel two-dimensional germanium allotrope akin to graphene and silicene. *New Journal of Physics*, 16(9):095002, 2014.

[14] Seunghyun Lee and Zhaohui Zhong. Nanoelectronic circuits based on two-dimensional atomic layer crystals. *Nanoscale*, 6(22):13283–13300, 2014.

[15] Manish Chhowalla, Hyeon Suk Shin, Goki Eda, Lain-Jong Li, Kian Ping Loh, and Hua Zhang. The chemistry of two-dimensional layered transition metal dichalcogenide nanosheets. *Nature chemistry*, 5(4):263, 2013.

[16] Francesco Bonaccorso, Luigi Colombo, Guihua Yu, Meryl Stoller, Valentina Tozzini, Andrea C Ferrari, Rodney S Ruoff, and Vittorio Pellegrini. Graphene, related two-dimensional crystals, and hybrid systems for energy conversion and storage. *Science*, 347(6217):1246501, 2015.

[17] Seba Sara Varghese, Saino Hanna Varghese, Sundaram Swaminathan, Krishna Kumar Singh, and Vikas Mittal. Two-dimensional materials for sensing: graphene and beyond. *Electronics*, 4(3):651–687, 2015.

[18] Gwan-Hyoung Lee, Young-Jun Yu, Xu Cui, Nicholas Petrone, Chul-Ho Lee, Min Sup Choi, Dae-Yeong Lee, Changgu Lee, Won Jong Yoo, Kenji Watanabe, et al. Flexible and transparent mos2 field-effect transistors on hexagonal boron nitride-graphene heterostructures. *ACS nano*, 7(9):7931–7936, 2013.

[19] Riccardo Pisoni, Zijin Lei, Patrick Back, Marius Eich, Hiske Overweg, Yongjin Lee, Kenji Watanabe, Takashi Taniguchi, Thomas Ihn, and Klaus Ensslin. Gate-tunable quantum dot in a high quality single layer mos2 van der waals heterostructure. *Applied Physics Letters*, 112(12):123101, 2018.

[20] Somaia Sarwat Sylvia, Khairul Alam, and Roger K Lake. Uniform benchmarking of low-voltage van der waals fets. *IEEE Journal on Exploratory Solid-State Computational Devices and Circuits*, 2:28–35, 2016.

[21] Andrea Splendiani, Liang Sun, Yuanbo Zhang, Tianshu Li, Jonghwan Kim, Chi-Yung Chim, Giulia Galli, and Feng Wang. Emerging photoluminescence in monolayer mos2. *Nano letters*, 10(4):1271–1275, 2010.

[22] KC Santosh, Roberto C Longo, Rafik Addou, Robert M Wallace, and Kyeongjae Cho. Impact of intrinsic atomic defects on the electronic structure of mos2 monolayers. *Nanotechnology*, 25(37):375703, 2014.

[23] Gonglan Ye, Yongji Gong, Junhao Lin, Bo Li, Yongmin He, Sokrates T Pantelides, Wu Zhou, Robert Vajtai, and Pulickel M Ajayan. Defects engineered monolayer mos2 for improved hydrogen evolution reaction. *Nano letters*, 16(2):1097–1103, 2016.

[24] Shinichiro Mouri, Yuhei Miyauchi, and Kazunari Matsuda. Tunable photoluminescence of monolayer mos2 via chemical doping. *Nano letters*, 13(12):5944–5948, 2013.

[25] Joonki Suh, Tae-Eon Park, Der-Yuh Lin, Deyi Fu, Joonsuk Park, Hee Joon Jung, Yabin Chen, Changhyun Ko, Chaun Jang, Yinghui Sun, et al. Doping against the native propensity of mos2: degenerate hole doping by cation substitution. *Nano letters*, 14(12):6976–6982, 2014.

[26] Honglai Li, Xidong Duan, Xueping Wu, Xiujuan Zhuang, Hong Zhou, Qinglin Zhang, Xiaoli Zhu, Wei Hu, Pinyun Ren, Pengfei Guo, et al. Growth of alloy mos2 x se2 (1–x) nanosheets with fully tunable chemical compositions and optical properties. *Journal of the American Chemical Society*, 136(10):3756–3759, 2014.

[27] Yanfeng Chen, Jinyang Xi, Dumitru O Dumcenco, Zheng Liu, Kazu Suenaga, Dong Wang, Zhigang Shuai, Ying-Sheng Huang, and Liming Xie. Tunable band gap photoluminescence from atomically thin transition-metal dichalcogenide alloys. *Acs Nano*, 7(5):4610–4616, 2013.

[28] Joseph John Thomson. Cathode rays. *The London, Edinburgh, and Dublin Philosophical Magazine and Journal of Science*, 44(269):293–316, 1897.

[29] Ernest Rutherford. The scattering of α and β particles by matter and the structure of the atom. *The London, Edinburgh, and Dublin Philosophical Magazine and Journal of Science*, 21(125):669–688, 1911.

[30] N.W. Ashcroft and N.D. Mermin. *Solid State Physics*. Cengage Learning, 2011.

[31] Wahyu Setyawan and Stefano Curtarolo. High-throughput electronic band structure calculations: Challenges and tools. *Computational materials science*, 49(2):299–312, 2010.

[32] Dominik Bogdan Jochym and Stewart Clark. *Development of Non-Local Density Functional Methods*. 2012.

[33] Valerio Magnasco. Chapter 16 - post-hartree–fock methods. In Valerio Magnasco, editor, *Elementary Molecular Quantum Mechanics (Second Edition)*, pages 681 – 722. Elsevier, Oxford, second edition edition, 2013.

[34] Chr. Møller and M. S. Plesset. Note on an approximation treatment for many-electron systems. *Phys. Rev.*, 46:618–622, Oct 1934.

[35] L. H. Thomas. The calculation of atomic fields. *Mathematical Proceedings of the Cambridge Philosophical Society*, 23(5):542–548, 1927.

[36] Stig Lundqvist and Norman H March. *Theory of the inhomogeneous electron gas*. Springer Science & Business Media, 2013.

[37] P. A. M. Dirac. Note on exchange phenomena in the thomas atom. *Mathematical Proceedings of the Cambridge Philosophical Society*, 26(3):376–385, 1930.

[38] Pierre Hohenberg and Walter Kohn. Inhomogeneous electron gas. *Physical review*, 136(3B):B864, 1964.

[39] Walter Kohn and Lu Jeu Sham. Self-consistent equations including exchange and correlation effects. *Physical review*, 140(4A):A1133, 1965.

[40] Robert O Jones and Olle Gunnarsson. The density functional formalism, its applications and prospects. *Reviews of Modern Physics*, 61(3):689, 1989.

[41] Randolph Q Hood, MY Chou, AJ Williamson, G Rajagopal, and RJ Needs. Exchange and correlation in silicon. *Physical Review B*, 57(15):8972, 1998.

[42] John P Perdew, Kieron Burke, and Matthias Ernzerhof. Generalized gradient approximation made simple. *Physical review letters*, 77(18):3865, 1996.

[43] Jianmin Tao, John P. Perdew, Viktor N. Staroverov, and Gustavo E. Scuseria. Climbing the density functional ladder: Nonempirical meta–generalized gradient approximation designed for molecules and solids. *Phys. Rev. Lett.*, 91:146401, Sep 2003.

[44] John P Perdew, Matthias Ernzerhof, and Kieron Burke. Rationale for mixing exact exchange with density functional approximations. *The Journal of chemical physics*, 105(22):9982–9985, 1996.

[45] O Gunnarsson. O. gunnarsson, m. jonson, and bi lundqvist, phys. lett. 59a, 177 (1976). *Phys. Lett.*, 59:177, 1976.

[46] Stefan Grimme, Jens Antony, Tobias Schwabe, and Christian Mück-Lichtenfeld. Density functional theory with dispersion corrections for supramolecular structures, aggregates, and complexes of (bio)organic molecules. *Org. Biomol. Chem.*, 5:741–758, 2007.

[47] Stefan Grimme. Semiempirical gga-type density functional constructed with a long-range dispersion correction. *Journal of computational chemistry*, 27(15):1787–1799, 2006.

[48] Stefan Grimme, Jens Antony, Stephan Ehrlich, and Helge Krieg. A consistent and accurate ab initio parametrization of density functional dispersion correction (dft-d) for the 94 elements h-pu. *The Journal of chemical physics*, 132(15):154104, 2010.

[49] Robert A Evarestov. *Quantum chemistry of solids: the LCAO first principles treatment of crystals*, volume 153. Springer Science & Business Media, 2007.

[50] Alfonso Baldereschi. Mean-value point in the brillouin zone. *Physical Review B*, 7(12):5212, 1973.

[51] A Baldereschi and E Tosatti. Mean-value point and dielectric properties of semiconductors and insulators. *Physical Review B*, 17(12):4710, 1978.

[52] D Jetal Chadi and Marvin L Cohen. Special points in the brillouin zone. *Physical Review B*, 8(12):5747, 1973.

[53] DJ Chadi and Marvin L Cohen. Electronic structure of hg 1- x cd x te alloys and charge-density calculations using representative k points. *Physical Review B*, 7(2):692, 1973.

[54] Hendrik J. Monkhorst and James D. Pack. Special points for brillouin-zone integrations. *Phys. Rev. B*, 13:5188–5192, Jun 1976.

[55] John C Slater. An augmented plane wave method for the periodic potential problem. *Physical Review*, 92(3):603, 1953.

[56] Peter E Blöchl. Projector augmented-wave method. *Physical review B*, 50(24):17953, 1994.

[57] Ayse Berkdemir, Humberto R Gutiérrez, Andrés R Botello-Méndez, Néstor Perea-López, Ana Laura Elías, Chen-Ing Chia, Bei Wang, Vincent H Crespi, Florentino López-Urías, Jean-Christophe Charlier, et al. Identification of individual and few layers of ws 2 using raman spectroscopy. *Scientific reports*, 3:1755, 2013.

[58] Alejandro Molina-Sanchez and Ludger Wirtz. Phonons in single-layer and few-layer mos 2 and ws 2. *Physical Review B*, 84(15):155413, 2011.

[59] Benjamin Groven, Markus Heyne, Ankit Nalin Mehta, Hugo Bender, Thomas Nuytten, Johan Meersschaut, Thierry Conard, Patrick Verdonck, Sven Van Elshocht, Wilfried Vandervorst, et al. Plasma-enhanced atomic layer deposition of two-dimensional ws2 from wf6, h2 plasma, and h2s. *Chemistry of Materials*, 29(7):2927–2938, 2017.

[60] Keliang He, Charles Poole, Kin Fai Mak, and Jie Shan. Experimental demonstration of continuous electronic structure tuning via strain in atomically thin mos2. *Nano letters*, 13(6):2931–2936, 2013.

[61] Yongqing Cai, Jinghua Lan, Gang Zhang, and Yong-Wei Zhang. Lattice vibrational modes and phonon thermal conductivity of monolayer mos 2. *Physical Review B*, 89(3):035438, 2014.

[62] Georg Kresse. Vasp: Accuracy and validation of results.

[63] J.D.H. Donnay and Helen M. Ondik. *Crystal data: determinative tables. Volume II, Inorganic compounds*. 1973.

[64] Atsushi Togo and Isao Tanaka. First principles phonon calculations in materials science. *Scripta Materialia*, 108:1–5, 2015.

[65] John P Perdew. Density functional theory and the band gap problem. *International Journal of Quantum Chemistry*, 28(S19):497–523, 1985.

[66] Wilfried G Aulbur, Lars Jönsson, and John W Wilkins. Quasiparticle calculations in solids. *Solid State Physics*, 54:1–218, 2000.

[67] KK Kam and BA Parkinson. Detailed photocurrent spectroscopy of the semiconducting group vib transition metal dichalcogenides. *The Journal of Physical Chemistry*, 86(4):463–467, 1982.

[68] Goki Eda, Hisato Yamaguchi, Damien Voiry, Takeshi Fujita, Mingwei Chen, and Manish Chhowalla. Photoluminescence from chemically exfoliated mos2. *Nano letters*, 11(12):5111–5116, 2011.

[69] Victor Vega-Mayoral, Claudia Backes, Damien Hanlon, Umar Khan, Zahra Gholamvand, Maria O'Brien, Georg S Duesberg, Christoph Gadermaier, and Jonathan N Coleman. Photoluminescence from liquid-exfoliated ws2 monomers in poly (vinyl alcohol) polymer composites. *Advanced Functional Materials*, 26(7):1028–1039, 2016.

[70] A. Fonari and C. Sutton. Effective mass calculator. 2012.

[71] Hartwin Peelaers and Chris G Van de Walle. Effects of strain on band structure and effective masses in mos 2. *Physical Review B*, 86(24):241401, 2012.

[72] Won Seok Yun, SW Han, Soon Cheol Hong, In Gee Kim, and JD Lee. Thickness and strain effects on electronic structures of transition metal dichalcogenides: 2h-m x 2 semiconductors (m= mo, w; x= s, se, te). *Physical Review B*, 85(3):033305, 2012.

[73] Darshana Wickramaratne, Ferdows Zahid, and Roger K Lake. Electronic and thermoelectric properties of few-layer transition metal dichalcogenides. *The Journal of chemical physics*, 140(12):124710, 2014.

[74] Paul C Canfield and Z Fisk. Growth of single crystals from metallic fluxes. *Philosophical magazine B*, 65(6):1117–1123, 1992.

[75] Wu Zhou, Xiaolong Zou, Sina Najmaei, Zheng Liu, Yumeng Shi, Jing Kong, Jun Lou, Pulickel M Ajayan, Boris I Yakobson, and Juan-Carlos Idrobo. Intrinsic structural defects in monolayer molybdenum disulfide. *Nano letters*, 13(6):2615–2622, 2013.

[76] Ji-Young Noh, Hanchul Kim, and Yong-Sung Kim. Stability and electronic structures of native defects in single-layer mos 2. *Physical Review B*, 89(20):205417, 2014.

[77] Hannu-Pekka Komsa and Arkady V Krasheninnikov. Native defects in bulk and monolayer mos 2 from first principles. *Physical Review B*, 91(12):125304, 2015.

[78] Sandro Mignuzzi, Andrew J Pollard, Nicola Bonini, Barry Brennan, Ian S Gilmore, Marcos A Pimenta, David Richards, and Debdulal Roy. Effect of disorder on raman scattering of single-layer mo s 2. *Physical Review B*, 91(19):195411, 2015.

[79] Milan Tomić, Harald O. Jeschke, and Roser Valentí. Unfolding of electronic structure through induced representations of space groups: Application to fe-based superconductors. *Phys. Rev. B*, 90:195121, Nov 2014.

[80] Georg Kresse and D Joubert. From ultrasoft pseudopotentials to the projector augmented-wave method. *Physical Review B*, 59(3):1758, 1999.

[81] Georg Kresse and Jürgen Hafner. Ab initio molecular dynamics for liquid metals. *Physical Review B*, 47(1):558, 1993.

[82] Georg Kresse and Jürgen Hafner. Ab initio molecular-dynamics simulation of the liquid-metal–amorphous-semiconductor transition in germanium. *Physical Review B*, 49(20):14251, 1994.

[83] Georg Kresse and Jürgen Furthmüller. Efficiency of ab-initio total energy calculations for metals and semiconductors using a plane-wave basis set. *Computational materials science*, 6(1):15–50, 1996.

[84] Georg Kresse and Jürgen Furthmüller. Efficient iterative schemes for ab initio total-energy calculations using a plane-wave basis set. *Physical review B*, 54(16):11169, 1996.

[85] Akhil Sharma, Marcel A. Verheijen, Longfei Wu, Saurabh Karwal, Vincent Vandalon, Harm C. M. Knoops, Ravi S. Sundaram, Jan P. Hofmann, W. M. M. (Erwin) Kessels, and Ageeth A. Bol. Low-temperature plasma-enhanced atomic layer deposition of 2-d mos2: large area, thickness control and tuneable morphology. *Nanoscale*, 10:8615–8627, 2018.

[86] Hongliang Shi, Hui Pan, Yong-Wei Zhang, and Boris I Yakobson. Quasiparticle band structures and optical properties of strained monolayer mos 2 and ws 2. *Physical Review B*, 87(15):155304, 2013.